Diploma Thesis

In-situ SAXS study on the ion dynamics in microporous carbon based supercapacitors

Christian Prehal

Leoben, im März 2014

Montanuniversität Leoben

Institute of Physics

Eidesstattliche Erklärung

Ich erkläre an Eides statt, dass ich diese Arbeit selbstständig verfasst, andere als die angegebenen Quellen und Hilfsmittel nicht benützt und mich auch sonst keiner unerlaubten Hilfsmittel bedient habe.

Affidavit

I declare in lieu of oath, that I wrote this thesis and performed the associated research myself, using only literature cited in this volume.

19.03.2014

Datum

Unterschrift

Acknowledgements

I would like to thank all my co-workers and colleagues on the Institute of Physics for the friendly uptake, the many off-topic discussions and the support in any respect.

In particular I thank my supervisor Prof. Oskar Paris for his support and the motivating words he always finds. His enthusiasm and curiosity in scientific problems gave me the permanent opportunity to fill his time schedule with extensive discussions. Advices in both technical and personal concerns supported me in my constantly changing ideas and plans at work. I am looking forward to the next three years working together.

Furthermore I thank Dr. Rainer Lechner for the introduction to scattering techniques and the support at my first beamtime in Trieste. Also I would like to thank Ass. Prof. Volker Presser for introducing me to the exciting field of supercapacitors. I thank both Dr. Emilie Perre and Dr. Daniel Weingarth from the INM Saarbrücken, who gave me an insight into the rather unknown concepts of electrochemistry.

Moreover I would like to thank Frau Heide Kirchberger and Frau Magdalena Ottrin from the secretary's office for managing so much of my organizational work.

A very important factor in my life is my family. Thank you for guiding me into the right direction and supporting me in my whole life's decisions. In particular I thank Lena who helped me constantly forgetting my thesis for a while. And thank you Nadine for bearing with the materials scientiest's every-day problems and more important, being the most important person in my life.

Abstract

Supercapacitors or Electrical Double-layer Capacitors (EDLCs) are energy storage devices consisting of two electrodes immersed in a liquid electrolyte and contacted by metal current collectors. The energy is stored electrostatically by an electrical double-layer that forms upon applying a potential between the two electrodes. In contrast to conventional battery technologies no charge transfer across the electrode-electrolyte interface takes place. Hence the charge on the electrode side (electrons or holes) is situated across from the countercharge on the electrolyte side formed by the ions (corresponding to a plate capacitor). Due to the high surface area of the electrode materials (up to 2000m^2/g in activated carbons) and the small distance between the opposed charges on the interface, extremely high capacitance values are achieved. In such electrode materials the average pore width is typically below one nanometer inhibiting the formation of the conventional electrical double layer. Furthermore it was found that in the smallest accessible pores ions lose partially their solvation shell, leading to an anomalous increase of the normalized capacitance (F/m^2). There is still a lack of understanding on the appearance of the equilibrium ion structure and in particular the ion rearrangement and kinetics within such micropores.

In order to study the kinetics of ions with a time-resolution of seconds, in-situ Small Angle X-ray Scattering (SAXS) experiments were performed at the Austrian SAXS beamline at the Synchrotron radiation source ELETTRA in Trieste, Italy. While the working supercapacitor-device was irradiated with the Synchrotron X-ray beam, various potential signals via a potentiostat were applied to the cell. The scattering intensity (SAXS and Wide Angle X-ray Scattering (WAXS) with position sensitive detectors) as well as the sample transmission (with a photodiode) were recorded simultaneously. Beside the construction of the in-situ sample holder, in particular the data-analysis and interpretation bear a big challenge since a variety of processes take place simultaneously.

The in-situ SAXS measurements revealed a detailed analysis of the ion transport within different hierarchical levels (such as micro-, meso-, macropores, corresponding to pore sizes <2nm, 2-50nm, and >50nm, respectively) depending on the cell geometry and the investigated spot on the electrode. The actual electrosorption corresponds to a local ion transport from the macropores (serving as ion reservoirs) into the meso- and micropore volume, exhibiting a lower time constant than a macroscopic ion transport from one electrode to the other taking place within the macropores. Furthermore the expansion of micro- and mesopores in dependence of applied electrical potential could be tracked by analyzing the so-called SAXS correlation length. Combining

the measured transmission and electrical current signals, the absolute ion concentration changes within the irradiated pores could be evaluated. The total ion concentration was found to be constant for all potentials. According to our data a mechanical pressure due to the increased amount of ions within the pores plays only a minor role in terms of pore swelling. This effect requires further systematic investigations beyond this work.

In contrast to conventional electrochemical and other in-situ techniques (e.g. in-situ dilatometry), in-situ scattering not only provides integral information of the entire cell. It enables on the one hand a distinction between processes in different pore size regimes, on the other hand the study of the local properties on the investigated electrode, with a time resolution in the sub-second regime. The present work exhibits for the first time a detailed in-situ SAXS/WAXS study on the ion transport in microporous carbon based supercapacitors offering a distinction between the kinetics within different pore size levels.

Kurzfassung

Superkondensatoren oder elektrochemische Doppelschichtkondensatoren (EDLC) dienen zur effektiven Energiespeicherung. Sie bestehen ähnlich wie konventionelle Batterien aus zwei Elektroden, eingetaucht in flüssigem Elektrolyten, sowie metallischen Kontakten. Die Energie wird in Form einer elektrischen Doppelschicht nach dem Anlegen einer elektrischen Spannung elektrostatisch gespeichert. Im Unterschied zu Batterien tritt jedoch kein Ladungstransfer an der Elektrolyt-Elektroden-Grenzfläche auf. Die Spannungsabhängigkeit der sich gegenüberliegenden Ladungsmenge (Elektronen oder Löcher auf Elektrodenseite bzw. Kationen oder Anionen im Elektrolyten) führt zu der entsprechenden Kapazität. Auf Grund der extrem hohen spezifischen Oberflächen der verwendeten Elektrodenmaterialen wie z.B. Aktivkohle (bis zu 2000m^2/g) und dem geringen Abstand der sich gegenüberliegenden Ladungschichten können sehr hohe Kapazitäten und Speicherdichten erreicht werden. Die durchschnittliche Porengröße in solchen Materialien liegt unter 1nm, wodurch die übliche Struktur der elektrischen Doppelschicht nicht vollständig ausgebildet werden kann. Selbst kleinste Mikroporen sind auf Grund des partiellen Verlustes der Solvationsschale der Ionen zugänglich. Dies führt unter anderem zu einem anormalen Anstieg der spezifischen Kapazität (F/m^2). Die detaillierte Anordnung der Ionen und vor allem der Ionentransport und dessen Kinetik in den kleinsten Poren sind noch weitgehend unverstanden.

Um den Ionentransport innerhalb der porösen Kohlenstoffstruktur näher zu untersuchen, wurden in-situ Röntgen Kleinwinkelstreuversuche an der österreichischen SAXS Beamline am Synchrotron ELETTRA in Triest durchgeführt. Während des Anlegens verschiedener Spannungssignale mit Hilfe eines Potentiostaten wurden die Streuung sowie die Transmission der Röntgenstrahlung beim Durchtritt durch eine Elektrode des Superkondensators aufgezeichnet. Neben der Entwicklung einer geeigneten in-situ Messzelle gestaltete sich besonders die Datenanalyse und Interpretation auf Grund des gleichzeitigen Auftretens verschiedener physikalischer Prozesse äußerst schwierig.

Die in-situ Experimente ermöglichten eine detaillierte Analyse des Ionentransportes in Poren unterschiedlicher Größe, abhängig von der Zellgeometrie und dem Ort der bestrahlten Elektrodenfläche. Die eigentliche Elektrosorption entspricht einem lokalen Ionentransport ausgehend von den Makroporen (>50 nm, welche als Ionenreservoir dienen) in die Meso- (2-50nm) und Mikroporen (<2nm). Diesem Prozess nacheilend (größere Zeitkonstante), findet der makroskopische Ionentransport von einer Elektrode zur anderen innerhalb der Makroporen statt. Zudem konnte eine Expansion der Mikro- und Mesoporen bei Anlegen einer elektrischen

Spannung gemessen werden. Mit Hilfe des Transmissions- sowie des elektrischen Stromsignals konnte die absolute Ionenkonzentrationsänderung innerhalb der Porenstruktur berechnet werden. Die Gesamtionenkonzentration bleibt für alle Spannungen konstant. Die Expansion der Poren ist daher nicht auf eine erhöhte Ionenkonzentration zurückzuführen; das Verständnis dieses Effektes erfordert noch weitergehende über diese Arbeit hinausgehende Untersuchungen.

Im Unterschied zu konventionellen elektrochemischen sowie anderen in-situ Methoden (z.B. in-situ Dilatometrie) ermöglichen in-situ Streumethoden nicht nur die Messung integraler Information. Es kann einerseits zwischen Prozessen in unterschiedlichen Porengrößen, andererseits zwischen lokalen Abhängigkeiten auf der untersuchten Elektrode, unterschieden werden. Die vorliegende Arbeit zeigt erstmals eine detaillierte in-situ Streuuntersuchung des Ionentransportes in mikroporösen Kohlenstoff-basierten Superkondensatoren, welche eine Unterscheidung der Kinetik innerhalb unterschiedlicher Porengrößenordnungen ermöglicht.

Contents

Abbreviations

SAXS	Small Angle X-ray scattering
WAXS	Wide Angle X-ray scattering
EDLC	Electrical Double-layer Capacitor
WE	working electrode
CE	counter electrode
CC	current collector
YP-50	electrode material (activated carbon)
YP-80	2nd electrode material (activated carbon)
CV	cyclic voltammetry
CA	chronoamperometry
PZC	point of zero charge
D8	cell design according to chapter 3.3.1
D9	cell design according to chapter 3.3.1
$\tilde{I}$	integrated intensity
Lc	correlation length
$\tilde{I}(t)$	integrated intensity as a function of time
$Lc(t)$	correlation length as a function of time

1 Introduction

The demands for green energy technologies have increased dramatically within the last years. The capability of storing large amounts of energy in devices like batteries or supercapacitors plays a critical role for the development of e.g. electric mobility technologies [1]. Modern battery technologies reveal energy densities about two orders of magnitude higher than supercapacitors or Electrical Double layer Capacitors (EDLC) as indicated in Fig. 1 [2].

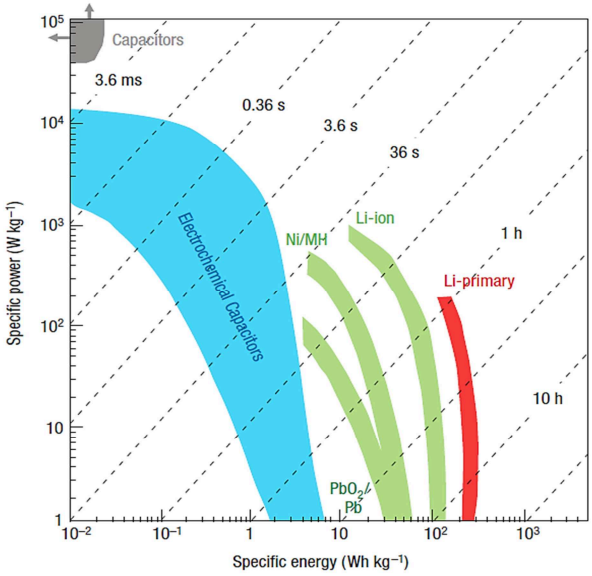

Fig. 1: Specific Power vs. specific energy for selected battery systems in comparison to electrochemical capacitors. Reproduced with permission from [2]. © Nature Publishing Group.

However, for applications where the provision or storage of energy has to happen within very short times highest power densities provided by supercapacitors are required. They consist of two electrodes immersed in a liquid electrolyte similar to typical electrochemical cells. In contrast to batteries no chemical, but electrostatic energy is stored at the electrode-electrolyte interface, exhibiting no kinetic limitations due to faradaic reactions. Ions of the liquid electrolyte with electrons/holes in the electrode build up an electric double layer at the interface as a result of a voltage applied between the two electrodes. To enhance the amount of stored energy the electrodes have to reveal high specific surface areas up to 2000m^2/g (e.g. activated carbons). Supercapacitors gain their high capacity mainly from the electrosorption process within the micropores (<2nm). Upon applying different potential signals to the electrodes, the balance of cations and anions within the micropores gets disturbed, leading to a net charge counterbalanced by electrons or holes within the carbon electrode. Since highest power densities (and therefore

highest ion mobilities) have to be maintained upon decreasing the average pore size, a detailed understanding of the ion kinetics of the electrolyte within the confined system of a microporous electrode is highly required[1, 3].

As compared to international standards the basic research activities in the field of energy storage devices are rather low in Austria. The growing international research community working on supercapacitors is strongly interdisciplinary consisting of electrochemists, material scientists and physicists. However, the charge-storage mechanism in the confinement of micropores in the size range of the actual ion diameter is an in-depth physical problem.

In 2006 an anomalous increase of the normalized capacitance (F/m^2) in electrode materials with preferably monodisperse pores in the size range of the desolvated ion diameter was found [4]. In order to enter the smallest accessible pores at least a partial desolvation of ions must occur [5]. Not only the technological opportunities, but in particular the lack of understanding of the physical origin of this anomalous capacitance increase gave rise to increased research activities on supercapacitors within the last years. Recently published in-situ experiments [6-10] as well as enhanced simulation studies [11-15] led to improvements in the understanding of the ion rearrangement within the confined system of highly porous electrode materials. A molecular dynamics study of Merlet et al. could explain the capacitance increase for an ionic liquid electrolyte (no solvent) in a model carbon derived carbon (CDC) electrode. The closer approach of counter ions to the electrode surface compared to systems with larger pores is responsible for the increase in the normalized capacitance [11]. Fig. 2 should emphasize the complexity of the investigated systems and the difficulty not only for experiments, but also for modelling approaches to study the supercapacitor behavior on the molecular level.

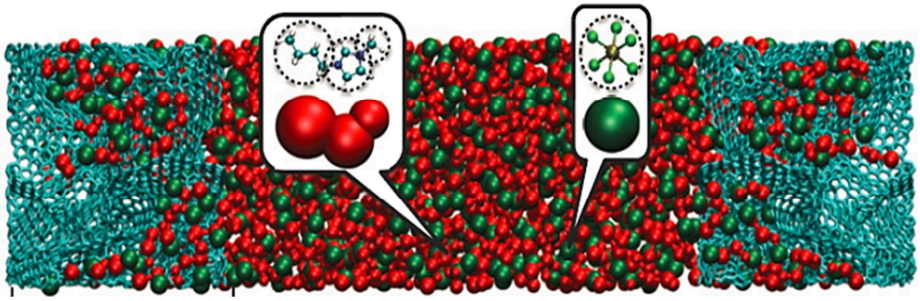

Fig. 2: The model system of the molecular dynamics simulation of Merlet et al is indicated. The cyan structure on the left and the right represents a carbide-derived carbon (CDC) model electrode, the red and green species the cations and anions of the ionic liquid, respectively. The ionic liquid has entered the micropores of the CDC structure [11]. In particular the disordered nature of the micropores makes experimental investigations difficult. Reproduced with permission from [11]. © Nature Publishing Group.

The ion arrangement within the confinement of a conducting electrode is determined by a variety of interactions. Beside electrostatic ion-ion and ion-pore wall interactions also the solvent

molecules of the aqueous or organic electrolyte play a significant role on the ion behavior in confinement [13]. The loss of the tight solvation shell may influences the kinetic behavior of the ions as well. Upon charging the electrode e. g. negatively the countercharge on the electrolyte side can be established by either inserting additional cations or withdrawing anions from the micropores [7]. Hence in-situ techniques enabling the distinction between the single ion species are required.

Another barely understood phenomenon is the expansion or contraction of the carbon electrodes upon charging. The macroscopic strain may be an important factor for the supercapacitor lifetime [9] or might be used for electrochemical actuators [16, 17]. In literature the swelling is sometimes reduced to the increased total ion concentration within the pores leading to an increased pressure acting on the pore walls and depending on the ion sizes [9, 18]. Other studies gave rise to the idea of the carbon electrode changing its interface properties upon inserting or withdrawing electrons [19-21]. Several contributions may change the electrolyte-electrode interface properties leading to a change in the surface stress. Only the knowledge of the interactions between the involved species (carbon, cations, anions, solvent molecules) enables a fundamental understanding of the physical origin of the pore strain.

In 2010 Ruch et al. first used in-situ Small-angle X-ray Scattering (SAXS) to study ion insertion processes during the electrochemical activation of activated carbon electrodes [22]. Another Small-angle Neutron Scattering (SANS) study in 2013 could provide information on the strong influence of the electrolyte solvent on the wetting properties and consequently the ability of ions to contribute to charge storage [23]. Both experiments showed the high potential of scattering techniques to study changes of the ion rearrangements within the microporous carbon structure. Although experimentally difficult to achieve, the simultaneous investigation of processes within different pore size regimes is basically possible. Due to the high photon flux of modern Synchrotron radiation X-ray sources, scattering curves with a time resolution in the millisecond regime are recordable. Since the beam has a size of several hundred nanometers up to some millimeters, the measurement of different spots on the electrode enables the investigation of local dependencies and the dependency on the cell design. In comparison to other in-situ or conventional electrochemical techniques in-situ scattering methods not only provide integral information of the entire electrode. Changes of all included materials (electrode, solvent, ions) can be studied on different hierarchical levels, such as different pore size regimes or different spots on the investigated electrode [24].

The aim of the present work is to perform a detailed kinetic study of the ion rearrangement within the micropores of carbon electrodes in an aqueous CsCl electrolyte. The measurement on different spots on the working electrode and the ability of studying processes within different pore size regimes simultaneously should provide a comprehensive picture of the ion transport.

The strain of micropores upon charging is a rather complex phenomenon and poorely understood. Hence, in-situ scattering represents an alternative method to study the expansion/contraction of micropores. As a complementary technique the macroscopic swelling of the carbon electrode is tracked by dilatometry measurements. The calculation of the absolute ion concentrations using the transmission signal and the theoretical attenuation coefficients should provide information on the impact of the total ion concentration on the pore strain. Beside the development of a specially designed supercapacitor cell, in particular the data analysis and interpretation bear a big challenge, since a variety of processes are recorded simultaneously. Separating all these contributions from the scattering signal should provide detailed insights into ion kinetics depending on the pore size level and the electrical potential signal applied.

In general, the present thesis should not only contribute to the fundamental understanding on the enhancement of the supercapacitor power or energy capability. It can be seen in a more general context, important also e.g. in biological systems or desalination. Ions surrounded by solvent molecules confined in a porous structure of charged materials, lead to several phenomena dependent on the detailed arrangement of ions. The multiple interactions of ions arising with the pore walls, other ions and the solvent molecules are responsible for the strong dependency of physical properties (like the normalized capacity (F/m^2) or pore strain) on the size of confinement and the extend of charging. Hence, tracking ion transport and rearrangement with in-situ scattering techniques might be a novel opportunity to improve the understanding of these complex systems.

2 Fundamentals

2.1 Interaction of matter with light

Photons of an X-ray beam interact with atoms of any kind of material in different ways, as indicated in Fig. 3. Depending on the type of material and its thickness some photons are absorbed, at small X-ray energies with highest probability due to the photoelectric effect. Caused by the absorption of energy other particles such as electrons (photoelectric effect) or photons with different wavelengths (fluorescence) can be emitted additionally by the material. Furthermore the electromagnetic wave gets scattered elastically (no energy loss) or inelastically (energy loss, phonons or other excitations are included in the scattering process). Elastically scattered waves only change the direction of their wave vector, but not its magnitude. All of the emitted particles (or waves) can be detected and used to gain information on the inner structure or the chemistry of the material [25, 26]. In the following the theory about elastically scattered X-rays is briefly described (Thomson Scattering).

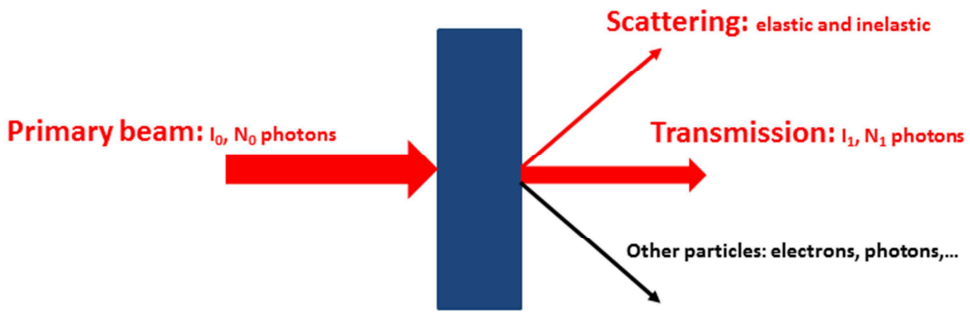

Fig. 3: Interaction of matter with light. The emitted particles/waves (on the right) can be detected and used to study the irradiated material.

2.2 Scattering theory

2.2.1 Basics

If an incoming X-ray beam hits a sample the beam gets scattered. The detector records the intensity of the scattered beam as a function of the scattering angle 2θ. More generally the wave vector is given by $\vec{Q} = \vec{k}_2 - \vec{k}_1$, where $\vec{k}_1$ and $\vec{k}_2$ corresponds to the wave vectors of the incoming and scattered wave, respectively (Fig. 4a). In a closer look (Fig. 4b) an incoming, monochromatic

and coherent electromagnetic plane wave hits an ensemble of scattering centers (electrons in the case of X-rays). Spherical waves with their origin at the electron position are emitted. At large distances those waves can be replaced by plane waves to a good approximation. The phase difference between two plane waves at a defined angle 2θ is defined by the position of their origin in the ensemble of electrons. For the incoming wave k_1 the path difference between the points 0 and r_n equals $r_n * \sin\theta$, which corresponds to a phase difference of $(2\pi r_n \sin\theta)/\lambda = \vec{k}_1 * \vec{r}_n$. The scattered wave exhibits a phase difference of $-\vec{k}_2 * \vec{r}_n$, thus the total phase difference corresponds to $(\vec{k}_1 - \vec{k}_2) * \vec{r}_n$. The wave scattered at position r_n shows in comparison to the scattered wave at position 0 a phase factor of $exp[i(\vec{k}_1 - \vec{k}_2) * \vec{r}_n] = exp[-i\vec{Q}\vec{r}_n]$ [27].

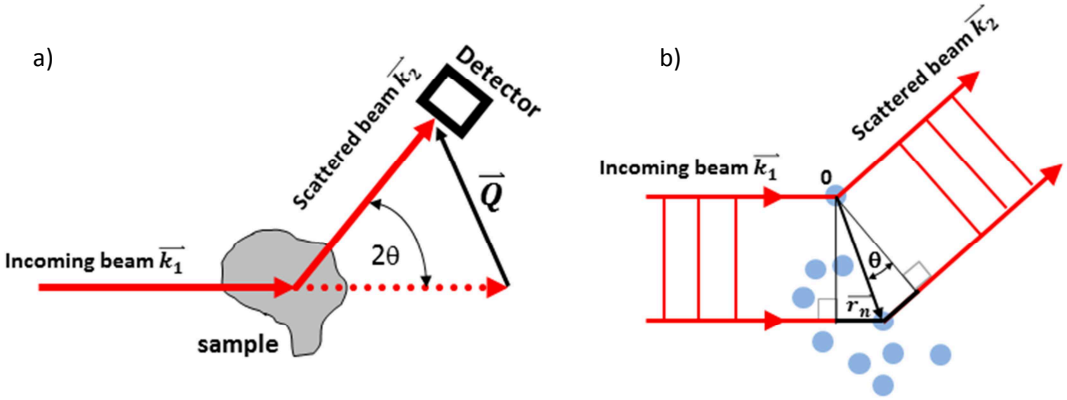

Fig. 4: a) If an incoming beam with the wavelength λ hits a sample it gets scattered in different directions. Studying the intensity of the scattered waves for different scattering angles 2θ enables the investigation of the inner structure of the sample. The absolute value of $\vec{Q}$ can be written as $4\pi \sin\theta/\lambda$. Adapted from [28]. In b) an ensemble of scattering centers (electrons in the case of X-rays) is indicated [28]. As indicated in b) the phase difference for a monochromatic wave scattered by an electron at the origin and at position r_n is responsible for either constructive or destructive interference at the scattering angle 2θ [27].

The probability that an incoming photon hits an electron and is subsequently scattered is expressed by the scattering length b_n. The amplitude of the scattered wave is therefore lowered compared to the incoming wave. The total amplitude of a scattered wave at any scattering angle $(Q \text{ or } 2\theta)$ is now represented by the sum of all scattered waves in the irradiated area. In a real measurement only intensities are recordable. The intensity is the square of the absolute value of the amplitude of the scattered wave and is written as

$$I(Q) = K\frac{d\Sigma}{d\Omega} = \frac{K}{V}\left|\sum_n b_n e^{-i\vec{Q}\vec{r}_n}\right|^2. \qquad (1)$$

V represents the irradiated volume, K is an instrumental constant and related to the experimental conditions like detector efficiency, detector-specimen distance, cross section of the beam, etc. The differential scattering cross-section per unit volume $\frac{d\Sigma}{d\Omega}$ corresponds to the probability of a photon being scattered in a sample unit volume into the solid angle element $\Delta\Omega$. The electron

positions can be expressed by a continuous function of the electron density $\rho(\vec{r})$, which is (similar to the scattering length) proportional to the probability that a photon gets scattered. Thus *I(Q)* can be rewritten to [28, 29]

$$I(Q) = \frac{K}{V}\left|\int_V \rho(\vec{r})\, e^{-i\vec{Q}\vec{r}}\, d^3r\right|^2 \tag{2}$$

2.2.2 Diffraction

The periodicity of the electron densities in a crystal, can be written as a Fourier series in the form

$$\rho(\vec{r}) = \sum_G \rho_G e^{i\vec{G}\vec{r}}, \tag{3}$$

where $\vec{G}$ is defined as a reciprocal lattice vector [27]. In order to preserve the translational invariance of the crystal lattice in real space, a reciprocal lattice with primitive reciprocal lattice vectors is defined. The periodic function of the crystal lattice *n(r)* is now inserted in eqn. (2).

$$I(Q) = \frac{K}{V}\left|\sum_G \int \rho_G e^{i(\vec{G}-\vec{Q})\vec{r}} d^3r\right|^2 \tag{4}$$

The intensity is negligible if $\vec{Q}$ is essentially different than $\vec{G}$, a recordable scattering intensity is only observed at scattering angles where the reciprocal lattice vector $\vec{G}$ is equal to the wave vector $\vec{Q}$. The diffraction condition, for observing a position where the scattered waves interfere constructively, is given by $\vec{Q} = \vec{G}$ and can be transformed to the famous Bragg-equation, using the following expression.

$$\left|\vec{Q}\right| = \frac{4\pi \sin\theta}{\lambda} = \left|\vec{G}\right| = \frac{2\pi}{d_{hkl}} \qquad \rightarrow \qquad 2d_{hkl}\sin\theta = \lambda \tag{5}$$

The distance between two parallel lattice planes normal to the direction of $\vec{G}$ is represented by d_{hkl}. In the case the diffraction condition is valid the intensity is expressed by

$$I(Q) = \frac{K}{V} N \left|\int_{cell} \rho(\vec{r}) e^{-i\vec{G}\vec{r}} d^3r\right|^2 = \frac{K}{V} N |S_F|^2\,, \tag{6}$$

with S_f representing the so-called structure factor for a perfectly ordered crystal and N as the number of unit cells within the irradiated volume. The expression for the structure factor of the base can be rewritten as a sum of all atoms in the primitive unit cell to

$$S_F(Q) = \sum_j f_j\, e^{-i\vec{G}\vec{r}_j}\,, \tag{7}$$

where f_j is the atomic formfactor, considering the spatial extension of the electron density around the atom [27].

In a liquid or amorphous solid the long-range translational order is not preserved, only the distance between nearest neighbors remains nearly constant. Thus the structure factor of a liquid

does not consist of delta-functions at the positions where the diffraction condition is fulfilled, as in the crystalline case. Due to the short range order only some broadened peaks are visible (Fig. 5). At higher Q-values the peaks become more and more smeared out [27, 30]. Eqn. (1) was derived for the scattering of an ensemble of scattering centers, which are electrons in the case of X-rays. Replacing the scattering length b_n by the atomic formfactor $f(Q)$ and neglecting the instrumental constant and the volume normalization, leads to a similar expression describing an ensemble of atoms (of the same type) acting as scattering centers.

$$I(Q) = f(Q)^2 \sum_n e^{i\vec{Q}\vec{r}_n} \sum_m e^{-i\vec{Q}\vec{r}_m} = f(Q)^2 \sum_n \sum_m e^{i\vec{Q}(\vec{r}_n - \vec{r}_m)} \quad (8)$$

From the double-summation the terms with *n*=*m* are separated.

$$I(Q) = Nf(Q)^2 + f(Q)^2 \sum_n \sum_{m \neq n} e^{i\vec{Q}(\vec{r}_n - \vec{r}_m)} \quad (9)$$

The second summation term is now replaced by an integral. With the implementation of n_0, representing the average density of atoms, and $n_n(\vec{r}_{nm})$ being the density of atoms located at position $\vec{r}_m - \vec{r}_n$ with respect to the position of the reference atom $\vec{r}_n$, eqn. (9) can be rewritten to

$$I(Q) = Nf(Q)^2 + f(Q)^2 \sum_n \int_V [n_n(\vec{r}_{nm}) - n_0] e^{i\vec{Q}(\vec{r}_n - \vec{r}_m)} dV_m$$
$$+ f(Q)^2 n_0 \sum_n \int_V e^{i\vec{Q}(\vec{r}_n - \vec{r}_m)} dV_m \,. \quad (10)$$

The last term corresponds to the scattering of a homogenous density of atoms n_0 and is negligible despite of small Q-values (small angles). If the volume $V \to \infty$ the integral is a delta function at the origin. In the following this small angle scattering term is neglected. The remaining summation over all reference positions *n* in eqn. (10) is replaced using $n(\vec{r})$, which corresponds to an average over all *n*.

$$I(Q) = Nf(Q)^2 + f(Q)^2 \int_V [n(\vec{r}) - n_0] e^{i\vec{Q}\vec{r}} dV \quad (11)$$

Due to the isotropy in a liquid the phase factor can be averaged over a sphere using $\langle \exp[i\vec{Q}\vec{r}] \rangle = sin\, Qr\, /Qr$. This leads to

$$I(Q) = Nf(Q)^2 + f(Q)^2 \int_0^\infty [n(r) - n_0] 4\pi r^2 \frac{sin\, Qr}{Qr} dr. \quad (12)$$

The radial distribution function is defined as $g(r) = n(r)/n_0$. The liquid structure factor is thus expressed in the following way.

$$S(Q) = \frac{I(Q)}{Nf(Q)^2} = 1 + \frac{4\pi}{Q} \int_0^\infty r[g(r) - 1]\, sin\, Qr\, dr \quad (13)$$

With the Fourier-integral theorem in 3D *g(r)* can be calculated from the measured structure factor (Fig. 5).

$$g(r) = 1 + \frac{1}{2\pi^2 r n_0} \int_0^\infty Q[S(Q) - 1] \sin Qr \, dQ \tag{14}$$

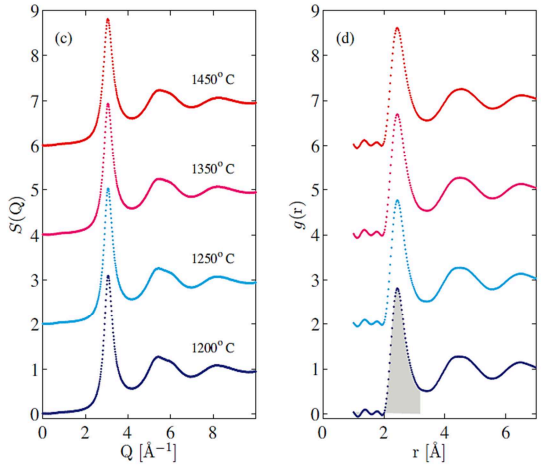

Fig. 5: Exemplarily the structure factor S(Q) of a liquid metal at different temperatures is indicated. The corresponding radial distribution function g(r) is given on the right. Reproduced with permission from [31]. © Wiley.

The reciprocal of the position of the first structure factor peak is proportional to the mean distance of liquid molecules (*=2π/Q_{peak}*) [27, 31].

2.2.3 Small-Angle X-Ray Scattering

With Small-Angle X-ray Scattering, objects or distances with sizes of several nanometers are observable, depending on the recorded Q-region. In Fig. 6 a structure with two phases α and β, having different scattering length densities (X-rays: corresponding to different electron densities) both in the size range of nanometers, are indicated. In the limit of small scattering angles the recordable spatial correlations are much larger than atomic distances. If the two phases have a homogeneous electron density eqn. (2) can be rearranged to

$$I(\vec{Q}) = \frac{K}{V}(\rho_\alpha - \rho_\beta)^2 \left| \int_V \Theta(\vec{r})\, e^{-i\vec{Q}\vec{r}}\, d^3r \right|^2, \tag{15}$$

where ρ_α and ρ_β represent the electron densities of a phase α and β, respectively. $\Theta(\vec{r})$ is the structure function which contains all the geometrical information of the structure and is equal to 1 in the α-phase and 0 in the β-phase, or vice versa.

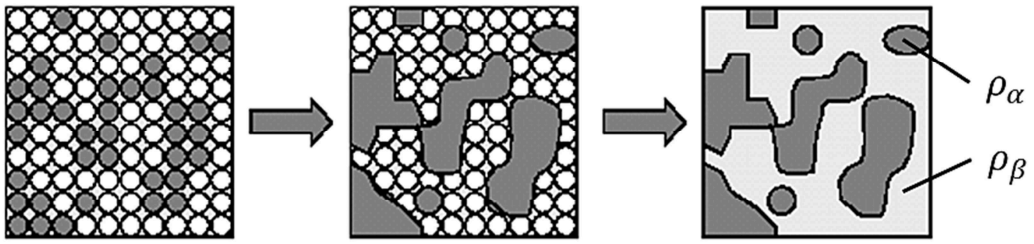

Fig. 6: 2D sketch of a structure with two different phases α (grey) and β (white) with a size of several nanometers. The atomic structure (indicated as small circles in the figure on the left) is not resolvable at Q-values where the two-phase model is applied. The electron density is assumed to be constant within each phase and the interfaces sharp and distinct (indicated in the right sketch). With SAXS the structure and shape of the two phases α and β can be studied. With permission from [29].

The so-called two-phase model assumes a sample of two phases with a homogeneous, average scattering length density and well defined, sharp interfaces. The size range of structures where the model is applicable depends on the Q-region recorded. At some point at larger Q-values details of the electron density function according to the atomic arrangement are resolvable – the two-phase model fails. In many systems the two-phase model is not applicable at all (e.g. colloidal systems). A good indication whether the two-phase model is applicable is that the size of the domain >> width of the interface [26, 28, 29].

2.2.4 Laue Scattering

Eqn. (2) can be rewritten in the following way.

$$\frac{d\Sigma}{d\Omega} = \frac{1}{V}\left|\int_V \rho(\vec{r})\, e^{-\vec{Q}\vec{r}}\, d^3r\right|^2 = AA^*$$

$$= \frac{1}{V}\int_V \rho(\vec{r}_1) e^{-i\vec{Q}\vec{r}_1} d\vec{r}_1 \int_V \rho(\vec{r}_2) e^{i\vec{Q}\vec{r}_2} d\vec{r}_2 \qquad (16)$$

$$\frac{d\Sigma}{d\Omega} = \frac{1}{V}\int_V \int_V \rho(\vec{r}_1)\rho(\vec{r}_2) e^{-i\vec{Q}(\vec{r}_1-\vec{r}_2)} d\vec{r}_1 d\vec{r}_2$$

$$= \frac{1}{V}\int_V e^{-i\vec{Q}\vec{r}} d\vec{r} \int_V \rho(\vec{r})\rho(\vec{r}+\vec{r}')d\vec{r}' \quad with \quad \vec{r} = \vec{r}_1 - \vec{r}_2;\ \vec{r}' = \vec{r}_2 \qquad (17)$$

The so-called correlation function $\gamma(\vec{r})$ can be visualized as the probability that a stick with the length *r* has its end in phase α, considering that the other end is already in the phase α.

$$\frac{d\Sigma}{d\Omega} = \frac{1}{V}\int_V \gamma(\vec{r}) e^{-i\vec{Q}\vec{r}} d\vec{r} \qquad (18)$$

$$where\ \gamma(\vec{r}) = \int_V \rho(\vec{r})\rho(\vec{r}+\vec{r}')d\vec{r}' \qquad (19)$$

If now a structure without any spatial correlation is assumed, already the nearest neighborhood of a particle of phase α the probability of finding another particle α corresponds to the total

probability of finding α in the entire sample volume. Thus the correlation function for $\vec{r} = 0$ and $\vec{r} > 0$ gives the following. In the case of rather dense-packed hard spheres the absence of any spatial correlation is not possible, since the probability of finding a neighboring particle is higher at the nearest neighbor distance.

$$\gamma(0) = \frac{1}{V}\int_V \rho^2(\vec{r}')d\vec{r}' = \langle\rho^2\rangle \quad for\ \vec{r} = 0 \tag{20}$$

$$\gamma(\vec{r}) = \frac{1}{V}\int_V \rho(\vec{r}')\langle\rho\rangle d\vec{r}' = \langle\rho\rangle^2 \quad for\ \vec{r} > 0 \tag{21}$$

The correlation function for all *r* can be written as, where $\delta(\vec{r})$ is the delta function (*1* for *r=0* and *0* for *r≠0*)

$$\gamma(\vec{r}) = \langle\rho\rangle^2 + (\langle\rho^2\rangle - \langle\rho\rangle^2)\delta(\vec{r}) \tag{22}$$

Inserting the expression above into eqn. (18) gives a constant intensity for all Q>0.

$$\frac{d\Sigma}{d\Omega} = \langle\rho^2\rangle - \langle\rho\rangle^2 + (2\pi)^3\langle\rho\rangle^2\delta(\vec{Q}) \tag{23}$$

The last term including the delta-function corresponds to the direct beam. Assuming a two-phase system with the densities ρ_α and ρ_β, leads to $\langle\rho\rangle^2 = (V_\alpha/V)^2(\Delta\rho)^2$, where V_α is the total volume of phase α and $\Delta\rho = \rho_\alpha - \rho_\alpha$. V_α/V corresponds to the volumetric concentration ϕ of particles α within the sample volume V. Furthermore $\langle\rho^2\rangle$ in such system is defined as $\langle\rho^2\rangle = (V_\alpha/V)(\Delta\rho)^2$. Hence the intensity for a dilute system of completely randomly distributed particles (ions) yields

$$\frac{d\Sigma}{d\Omega} = (\Delta\rho)^2\phi(1-\phi) \tag{24}$$

The scattering intensity is constant for all Q-values and depends on the concentration of the corresponding particles. In the field of metal physics this is often called Laue-Scattering [29]. In the case of low concentrations the Laue scattering intensity is approximately proportional to the concentration ϕ of one of the solid solution species. A different approach derived for disordered solid solutions yields an equivalent relation for Laue Scattering [32].

2.3 Transmission

Any electromagnetic radiation is losing energy when passing through a material. The intensity weakening of the X-ray beam in forward direction can be either caused by “real” absorption of the photon energy (photoelectric effect) or by a loss through scattered photons. The photoelectric effect represents the largest contribution to absorption, compared to elastic or inelastic scattering processes. An electron is hit by a photon and kicked out of the atom’s shell, which leads to an excitation of the atom. The additional energy of the excited state is subsequently emitted as fluorescence light which is either transferred into heat or emitted by the

material. According to Lambert-Beers law the X-ray beam intensity decays exponentially in the penetrated material. The transmission τ represents the fraction of the primary beam intensity I_0 which has passed through the penetrated material with the thickness d and is defined as follows [25, 26, 31].

$$\tau = \frac{I(d)}{I_0} = e^{-\mu d} \tag{25}$$

The linear attenuation coefficient μ is proportional to the attenuation cross section σ_{tot} ($\mu = \rho_{at} * \sigma_{tot}$, where ρ_{at} is the atomic number density) [31]. The total cross section is the sum of the contributions of the photoelectric effect σ_{pe}, coherent scattering σ_{coh} (Rayleigh), incoherent scattering σ_{incoh} (Compton) and other negligible contributions [33]. For low X-ray energies (e.g. 8keV) the absorption due to the photoelectric effect predominates. Thus the attenuation coefficient depends on the atomic number ($\sim Z^4$) and the photon energy ($\sim E^{-3}$), when neglecting edge effects [31, 33]. Also the thickness d of the material has a strong influence on how much energy is absorbed and transmitted. In the present work we will not strictly refer to "attenuation", but often use the term absorption and absorption coefficients since all other contributions are negligible.

The transmission of a material having more than one component, e.g. α, β, γ can be written as

$$\tau = e^{-\mu_{total} d_{total}} = e^{-\mu_\alpha d_\alpha} * e^{-\mu_\beta d_\beta} * e^{-\mu_\gamma d_\gamma} \tag{26}$$

If the absorption coefficients and the amount of two components are known, the amount or concentration of the third can be calculated. Often the combination with measurements, where one or two phases are missed out, enables an exact evaluation of the amount/concentration of the component of interest.

2.4 Supercapacitors

2.4.1 Basics

Supercapacitors or Electrochemical Double-layer Capacitors (EDLCs) represent alternative energy storage devices with several advantages and disadvantages compared to common battery systems [1, 3, 34]. Unlike battery technologies (e.g. Lithium ion batteries) not a chemical but an electrostatic energy is stored in an electrical double layer on the electrode-electrolyte interface. In an EDLC two electrodes are immersed in a liquid electrolyte (such as any salt in an aqueous or organic solvent). If a voltage is applied an electrical double-layer forms on the electrode-electrolyte interface. On the surface of the metal or semiconducting electrode the electrons (negative applied potential) or holes (positive applied potential) attract cations or anions from the

solution. After the formation of the double-layer the potential drop on both electrodes corresponds to the applied potential (Fig. 7b).

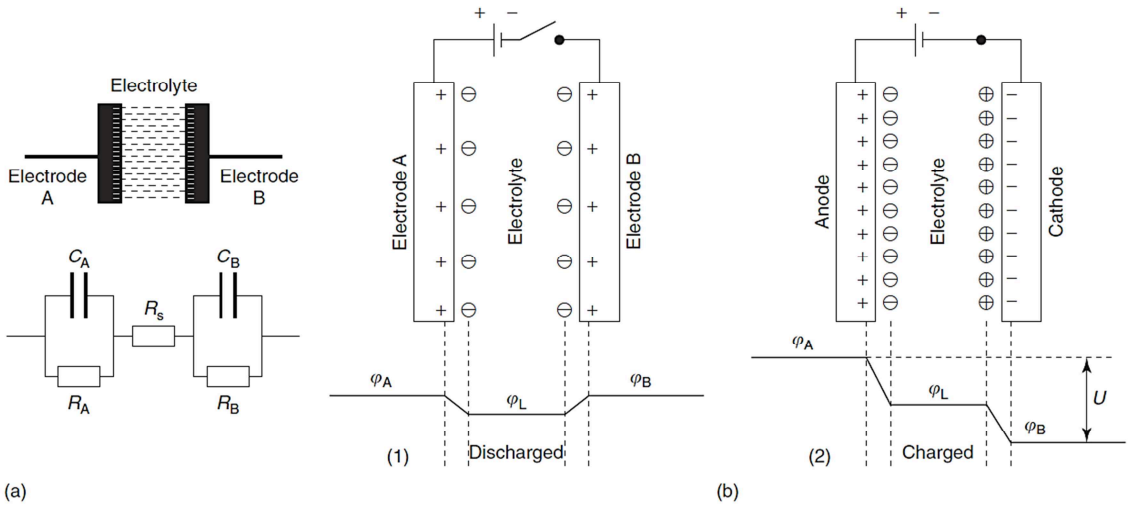

Fig. 7: Schematic working principle of an electrical double-layer capacitor. In a) the equivalent circuit of a realistic EDLC is indicated. b) At 0V some species contained in the electrolyte may preferentially adsorb on the surface (e.g. specific adsorption of anions), thus a small potential drop on the electrode/electrolyte interface is possible. Upon applying a potential to the electrodes the charges in the electrolyte are separated, on the electrode/electrolyte interfaces two layers of opposed charges are arranged, which is equivalent to two plate capacitors in series. With permission from [35]. © Elsevier.

The two electrodes (e.g. activated carbon) are contacted with metal current collectors (CC). An ion separator in between the two electrodes is in a symmetrical EDLC (Fig. 7) necessary to prevent electrical contact between the electrodes and acts as an ion (or electrolyte) storage. Since the electrodes, as well as the electrolytes and the contacts (CC) exhibit a finite ohmic resistance an equivalent circuit of a EDLC device looks like indicated in Fig. 7a. Furthermore the contribution of leakage currents due to electrochemical reactions (faradaic processes) is taken into account.

If an electrode is immersed in an electrolyte in many cases electrons are transferred from the electrolyte to the electrode and vice versa. Depending on the chemical potential in the solid (Fermi-energy) and the electron energy levels of the possible reactants in the solvent, a charge transfer (reaction) takes place. After thermodynamic equilibrium is reached, the rate of electron transfer is equal in forward and backward direction. Thermodynamic equilibrium means that the electrochemical potentials on the electrode and electrolyte side are equal. The difference in chemical potential is thus compensated by an electric potential formed by an electrochemical double-layer at the interface electrode-electrolyte. Preferably one sort of ions, dependent on the difference in chemical potential, is arranged around the electrode surface. If two different electrodes of this kind are immersed into an electrolyte, an open circuit potential (EMF:

represents essentially the difference of the Fermi-energies of the two electrode materials) can be tapped. If this potential is connected to an external load electrical current will result, which corresponds to a battery-like configuration [36]. In fact, there are also situations where the electrolyte/electrode combination does not allow any electron transfer across the interface. If no convenient redox couple is available on the electrolyte side an alignment of the electrochemical potentials is not possible. Due to energetic reasons electrochemical equilibrium between electrons on the electrode and the electrolyte side is not achieved. In Fig. 8 the typical energy level situation for an inert electrode (Pt, Carbon) in an electrolyte with the species A is shown. At 0 applied potential no reaction from the electrolyte side and thus no charge transfer is possible. Only at high enough positive potentials (polarization) an oxidation and at high enough negative potentials a reduction of the electrode is possible due to the Fermi level shift compared to the electrolyte energy levels (or the vacuum level) Charge transfer corresponds to a tunneling process of electrons, hence it is only allowed if the energy levels on electrode and electrolyte side are equal. [3, 36-38].

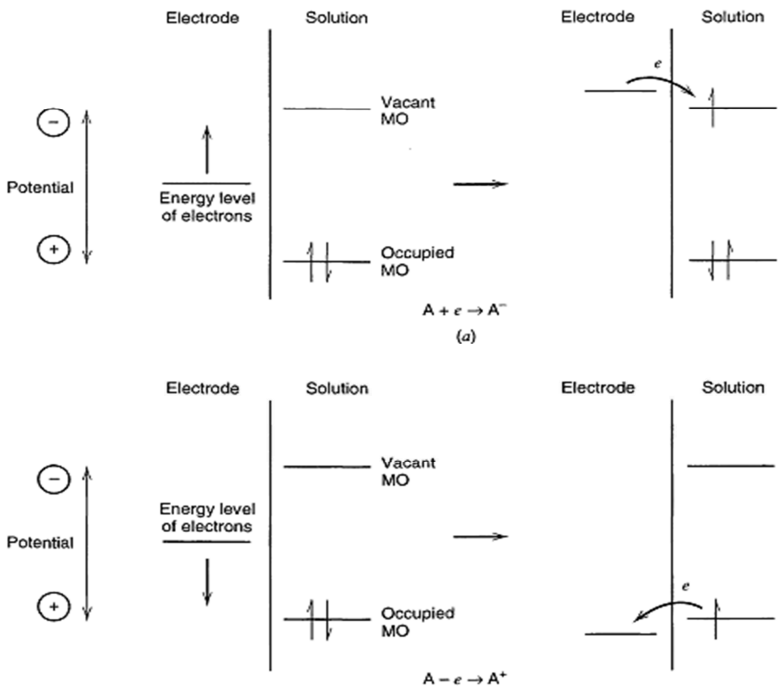

Fig. 8: Sketch of the energy levels at the electrode/electrolyte interface of an ideally polarizable electrode. By changing the applied potential a double layer is formed at the interface, which shifts the electron energy levels of the electrode compared to those in the electrolyte. On the top the situation for an oxidation, on the bottom for a reduction of the metal is indicated. A non-ideally polarizable electrode, where reduction takes place instantly after emerging the electrode into the electrolyte, has a lower Fermi-energy than the occupied molecular orbital of the reactand in the electrolyte. A double-layer forms without applying an external potential until electrochemical equilibrium is achieved. With permission from [36]. © Wiley.

By applying a potential electrons or holes are inserted into the electrode, ions of opposite sign in the electrolyte will be attracted; the situation corresponds to that of a plate capacitor. Such an electrode/electrolyte system is called ideally polarizable and in reality only found for a defined potential range [38]. The region where no faradaic processes take place is called the potential window, which is important for the EDLC performance. In aqueous solutions the typical potential window, avoiding water degradation, lies around 1V. Recently ionic liquids (salts with melting point below room temperature) became more and more an interesting alternative to common organic or aqueous electrolytes because of their high voltage stability. Since the stored energy in a capacitor scales with the square of the potential a large "potential window" of the electrolyte is advantageous. With organic electrolytes the potential window can be increased up to 2.7V, while ionic liquids withstand potential ranges up to 3V. Ionic liquid electrolyte EDLC devices with 1000F running at 3V are already commercially available [2].

Similar to a plate capacitor the capacitance can be increased either by increasing the surface, decreasing the distance between the charges or increasing the dielectric constant in between the charged layers.

$$C = \frac{\varepsilon_r \varepsilon_0 A}{d} \tag{27}$$

With the capacitance built up by a double layer the distance d of the opposed charges is in the order of atomic distances and thus decreased to a minimum. The surface area of the electrode material (e.g. carbide-derived carbons, activated carbons) can be increased up to ≈2000m^2/g or even higher. Too high surface areas (3000m^2/g) are unfavorable, since the remaining carbon matrix is not able to counterbalance all the ions with electrons/holes [39]. Compared to dielectric capacitors the EDLC technology seems to be most efficient for storing electrostatic energy. As electrode materials micro- and mesoporous carbons, such as activated carbons, carbide-derived carbons, carbon nanotubes and carbon aerogels are utilized [40, 41]. In order to gain maximum power density by decreasing the charging time constants and increasing the stored energy an optimized hierarchical structure of micro-, meso- and macroporosity is required [1].

Furthermore, additional energy storage mechanisms in the form of faradaic processes (pseudocapacity) are utilized in hybrid capacitors. Pseudocapacity arises from chemical reactions at the electrode/electrolyte interface where the produced current shows a significant dependency on the potential. Thus a differential capacity can be calculated, although the origin is not a capacitive mechanism in the common sense. Batteries usually show constant currents over a wide potential range. Small pseudocapacitive contributions may arise in every usual EDLC due to surface functional groups or any reactive species contained in the electrolyte [1, 36].

2.4.2 Structure of the Electrode-Electrolyte Interface

In Fig. 9 the state-of-the-art model of the electrical double-layer together with its potential decay on the solution side is indicated. Depending on the electrode conductivity the layer of electrons/holes can reveal a thickness of less than one atom (metal electrode) or be enlarged to a space charge region of several hundreds of atomic distances (semiconductor electrode). To a certain extend independent on the applied potential, some species in the electrolyte might adsorb on the electrode surface. Especially anions have the tendency to specifically adsorb on the surface [3, 36]. Specifically adsorbed species with non-zero charge shift the point of zero charge (pzc: corresponds to the potential where no net charge remains on the surface). The distance of specifically adsorbed species represents the Inner Helmholtz plane (IHP), where also oriented solvent molecules such as water are found. The outer Helmholtz Plane (OHP) is the smallest distance to the electrode surface of non- specifically adsorbed ions, which are hydrated and at a fixed distance to the electrode surface. Due to entropic reasons a diffuse layer with an exponential decay of the concentration of attracted ions surrounds the Helmholtz plane [36].

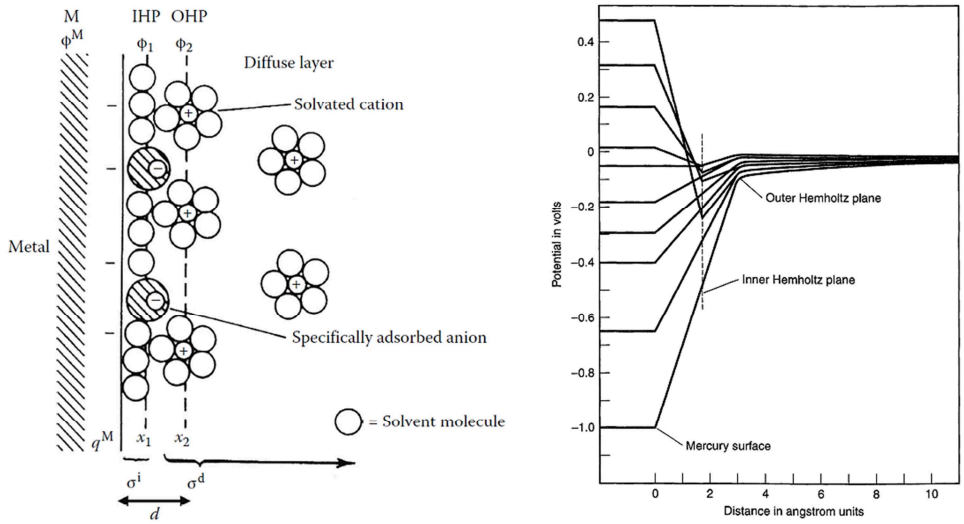

Fig. 9: a) State-of-the-art model of a double layer on a metal electrode. On the electrolyte side the inner Helmholtz plane (IHP) consists of oriented solvent dipoles and specifically adsorbed species (e.g. anions). In the outer Helmholtz plane (OHP) the actual counter charge of the electrode is situated, consisting of solvated cations. Due to entropic reasons at non-zero temperature a diffuse layer with an exponential decay of the concentration of counter ions borders on the OHP. With permission from [34]. © Taylor and Francis Group. In b) potential curves for different applied potentials are shown. At positive potentials a large influence of specifically adsorbed anions is given. The ion charge density is related to the potential decay on the electrolyte side according to the Poisson equation. With permission from [36]. © Wiley.

The theoretical calculation of the Double-layer capacitance is due to the double-layer structure rather complex. Since a direct observation of the double layer is difficult with any experimental technique, models have to be proposed and crosschecked with macroscopic, measurable

properties. One of these measurable properties is the voltage dependency of the differential capacity (Fig. 10). Helmholtz first suggested a monolayer of adsorbed counter-ions on the electrode surface which corresponds to the situation of a plate capacitor. This model predicts a constant differential capacitance.

$$\frac{\partial \sigma}{\partial V} = C_d = \frac{\varepsilon_r \varepsilon_0}{d} \tag{28}$$

C_d is the differential capacitance, σ the surface charge density, V the applied potential, ε_r is the relative permittivity of the medium (or dielectric constant), ε_0 the permittivity of free space and d the distance of opposed charges. However, experimental observations were different (Fig. 10b). Thus, Gouy and Chapman postulated independently the existence of a diffuse layer of counter ions on the electrolyte side [42-44]. Thermal excitation tries to randomize ions which are on the other hand attracted or repelled by the electric field of the electrode charge. Thus, at low applied potentials the counter-ion concentration decays exponentially from the electrode surface. At higher applied potential and at high ion concentrations in the electrolyte the diffuse layer is narrower and thus the capacitance higher, since the average distance d of opposed charges is smaller. Stern modified the Gouy-Chapman theory [45] by introducing a minimum distance ions can approach the electrode surface, because of the ion's finite size. The theoretically calculated differential capacity of the GCS-theory is shown in Fig. 10a. At potentials much higher or lower than the PZC a maximum capacity of C_H is achieved, which corresponds to counter charges all arranged within the Helmholtz planes. Around the PZC a lower capacitance due the extended formation of the diffuse layer occurs. At small concentrations the influence of the diffuse layer is more distinct.

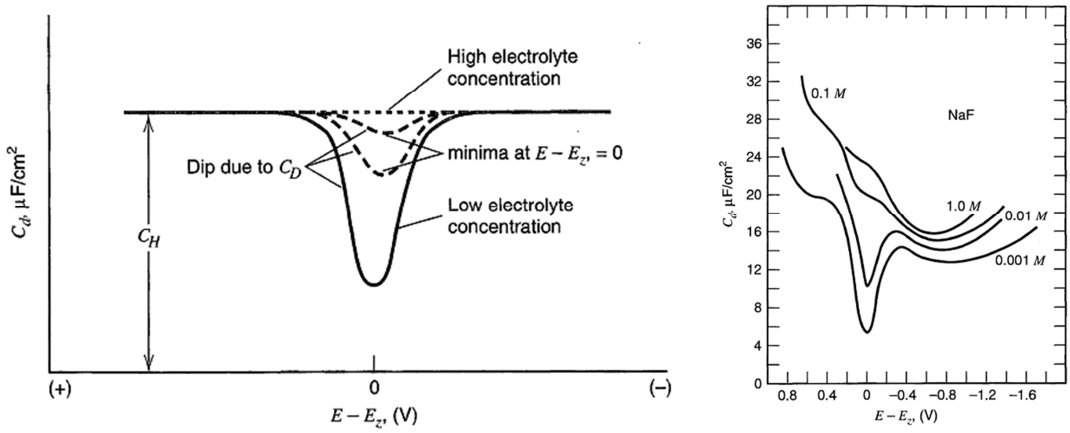

Fig. 10: a) Theoretically predicted differential capacity by the Gouy-Chapman-Stern (GCS) theory. Around the PZC a minimum of the capacity occurs, depending on the ion concentration in the electrolyte. b) Voltage dependency of the differential capacitance of a mercury electrode in NaF solutions having different concentrations at 25 °C. With permission from [36]. © Wiley.

Specifically adsorbed ion concentrations can be calculated from thermodynamic considerations. For common solid electrodes also crystallographic orientations, surface reconstructions and other surface related effects play an important role on double-layer formation [36].

For semiconductor electrodes not only the capacitance of the Helmholtz C_H and the diffuse layer C_{diff} on the electrolyte side but also the space charge region on the electrode side C_{SC} has to be considered [1].

$$\frac{1}{C_l} = \frac{1}{C_{SC}} + \frac{1}{C_H} + \frac{1}{C_{diff}} \tag{29}$$

In highly conducting materials the space charge region is restricted to one atomic layer, causing a high C_{SC} with a negligible contribution to the double-layer capacitance. However, in the case of highly oriented pyrolitic graphite (HOPG) [46] or some activated carbons [47] the contribution is not negligible. In this case the specific capacitance for both negative and positive potentials is increased with respect to the PZC. This effect is often referred to as quantum capacitance and is proportional to the electron density of states around the Fermi-level of the carbon material.

2.4.3 Kinetics of the charging/discharging process

The current I(t) of a plate capacitor with a serial resistance shows the following time dependency, as result to any applied potential step.

$$I(t) = \frac{U_0}{R} * e^{-t/\tau} \tag{30}$$

τ is the time constant and corresponds to $R*C$, U_0 the height of the potential step, R the serial resistance and t the time. The following arguments are based on the fundamentals of classical electrostatics and electrodynamics [48]. Imagine a supercapacitor cell (Fig. 7) where a constant potential is applied by closing a switch (which is situated in between the potential source and the metal contact of one electrode). In the moment the switch is closed an electromagnetic pulse spreads out in the conductor and the electrode. The mobile charge carriers (electrons) immediately react on the electromagnetic pulse, a current starts to flow. Since the capacities of the two electrodes are assumed to be in series the slowest step is critical for the time constant of charging and the resulting current curve $I(t)$. Assuming a well conducting electrode the ion transport in the electrolyte is the limiting step. An electron (or hole) on the electrode side approaches the interface not until the electric field of a cation (or anion) is felt and vice versa for the ion. The smaller the distance d between the ions and the opposed charge on the electrode side, the more charge can be stored. At the end of the charging process the potential within the bulk of the conducting electrode is constant (same is valid for the conducting electrolyte). The electric field of the ions on the electrolyte side acts against the equilibration of the potential in the inside of the electrode because of the partial screening of the electronic field by the ionic

field. Thus much more surface charges are needed on the electrode side to preserve the applied potential in the bulk electrode material, in comparison to the absence of the ionic layer on the electrolyte side.

The electrode pore structure, the electrolyte system, the electrolyte- and electrode-condcutivity and the cell design can have big influences on the capacity and resistance values. Usually, the limiting step in the charging process is the ion transport in the electrolyte. The ion flux arising from a concentration gradient is described by Fick's law

$$j_i = D_i \nabla c_i \,, \tag{31}$$

where D_i represents the Diffusion coefficient, ∇c_i the gradient of the ion concentration and j_i the ionic flux. In general the driving force for the ion transport is the minimization of the Gibbs free energy, thus not only the gradient of the chemical potential, but also the gradient of the electric potential acts as a driving force for ion movement.

$$v_i = -u_i(\nabla \mu_i + z_i F \, \nabla \psi) \,, \tag{32}$$

where v_i represents the ion velocity, u_i the ion mobility, z_i the charge number of the ion, F the Faraday constant and μ_i the chemical and ψ_i the electric potential. The electric potential gradient corresponds to an electric field which can be caused by an external applied field or a field caused by the excess of any ion species within the solution. The Nernst-Planck equation describes the ionic flux depending on concentration and electric potential gradients.

$$j_i = D_i \left(\nabla c_i + c_i z_i \frac{F \, \nabla \psi}{RT} \right) \tag{33}$$

The ionic conductivity is determined by the concentration of ions and the ion mobility, which correspond to the diffusivity (diffusion coefficient). Dissolved ions tend to form pairs of cations and anions, where in some cases the solvation shell is removed. The more ion pairs are present within the electrolyte the less single ions are available for charge transport. Also the degree of dissociation determines the ion concentration within the solvent [49].

The ion mobility is affected by the solvent viscosity, the ion interactions and the solvated ion size. According to the Debye-Hückel theory an excess number of counter ions are arranged around the actual ion. This shell of counter ions together with the hydration shell has to be dragged against the electric field, which produces additional frictional forces. Such forces are called electrophoretic retardation forces and lower the ion mobility [1, 3].

Furthermore in highly porous electrodes the confinement impedes the ion mobility. From impedance spectroscopy different diffusion constants, depending on the porous structure have been estimated. Equivalent circuits like the Transmission Line model from de Levie have been introduced in order to gain information the electrode pore structure. The longer the distance for

ions migrating into the inside of the pore, the higher the serial resistance in the transmission line model. In micropores (<2nm) the largest time constants for diffusion are expected. Thus, the charging process of the supercapacitor appears to be mainly limited by the diffusion process into the micropores [1].

2.4.4 Capacitance in microporous electrodes

In 2006 Chmiola et. al. reported a strong increase in the normalized capacitance per surface area for very small pore sizes in the sub nanometer regime [4]. In order to access the smallest pores down to sizes of the desolvated ion size, ions have to lose their solvation shell. The high energy cost of ion desolvation not only influences the energy storage but also the ion transport mechanism within the micropores [5]. In Fig. 11 the normalized capacitance behavior for carbon electrodes as a function of the average pore size is shown. In the past only pores larger than the solvated ion diameter were believed to be accessible. In region III curvature effects have to be considered, although cylindrical shaped pores does not conform to realistic shapes of mesoporous carbons. Curvature effects get more and more negligible in region IV; the situation corresponds to a planar electrode surface. In section I the capacitance increases indirect proportional to the pore radius. The ions are assumed to be completely or partially desolvated and arranged in the center of a cylindrical pore, as indicated in the sketch on the right in Fig. 11.

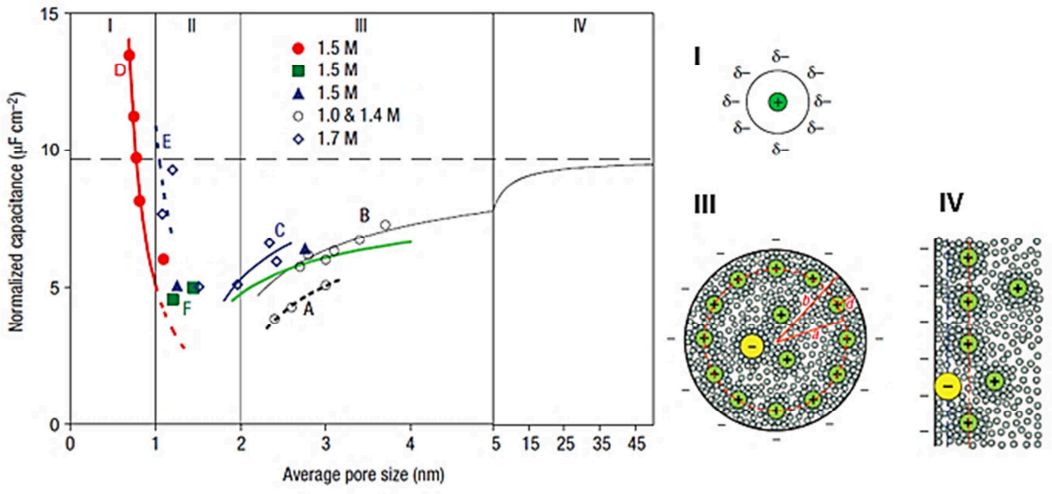

Fig. 11: The specific capacitance in µF/cm^2 vs. the average pore size of a porous carbon electrode is shown on the left. In order to obtain this behavior on real electrodes the pore size distribution has to be narrow. In section I, also indicated in the small sketch on the right, the solvation shell is released, and thus the normalized capacity increases dramatically when approaching an average pore size in the range of the ion size. In section III a double layer can form on the pore walls, although the curvature of a cylindrical pore affects the capacity. In section IV the usual double layer can be observed. With permission from [2]. © Nature Publishing Group.

The mathematical models to describe the simplified pictures indicated in the sketches I, III and IV were first proposed by Huang et al. in 2008 [50, 51]. However, there is still a lack of understanding in terms of a detailed physical explanation of the charge storage mechanism and the ion transport in micropores.

Kondrat and Kornyshev offered an explanation for the anomalous capacitance increase using a mean field and Monte Carlo approach using an ionic liquid confined between to metallic plates [14, 15]. The high conductivity of the metal plates screens the electric potential of the ions within the pore and enables a higher concentration of ions with the same sign within the pore. Furthermore the ionic "self-energy" changes, which corresponds to the energy that is needed to charge the ion in a specific surrounding. The energy cost of the desolvation of an ion is compensated by the difference in self-energy originating from image forces of the metal plates.

As Merlet et al. could show in a molecular dynamics simulation of an ionic liquid within a Carbon derived carbon (CDC) structure, the anomalous capacitance increase is caused by a closer approach of the ions to the pore walls compared to ions of a planar electrode [11]. The reason for that lies in the absence of the counter charged second ion layer, which is typical for ionic liquid electrolytes at planar electrode surfaces [12]. In addition the simulation showed that the carbon electrode is already filled with electrolyte before applying any potential. Insertion of electrolyte into an initially empty pore was indeed found, but only in very rare cases.

Feng et al. performed a molecular dynamics simulation on slit-like pores using an aqueous electrolyte [13]. The interaction of water molecules with ions (hydration) and with other water molecules plays a major role for the ion arrangement depending on the pore size (Fig. 12). Experimentally the measurement of such ion and solvent density profiles is very difficult.

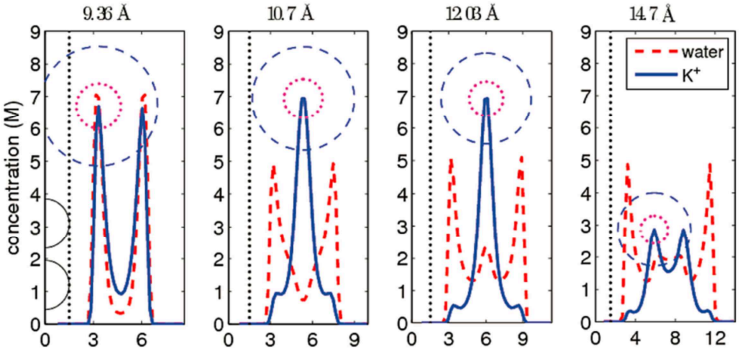

Fig. 12: Ion and solvent density profiles for different pore sizes. The dashed spheres on the top indicate the size of the bare and the solvated cations. For small enough pores the ion density is higher near the pore walls and not located in the central plane of the pore. With permission from [13]. © ACSNano.

2.4.5 Swelling of microporous electrodes upon charging

Recently the measurement of the macroscopic electrode expansion upon charging using In-situ dilatometry has been implemented [8, 9, 18, 19]. The kinetics of expansion showed clear correlations to the kinetics of the accumulated charge, calculated from the integration of the current signal. The highest measured expansions were about 2%, which is lower compared to expansions observed for intercalation processes [9]. In many times a large expansion at negative polarizations and a smaller expansion at positive potentials was found [19]. Several mechanisms for swelling or contraction of a porous electrode injected in a liquid electrolyte are proposed in literature.

In recently published dilatometry studies on microporous carbon EDLC electrodes the swelling was sometimes attributed to a pressure induced by the steric repulsion of ions and related to an increased total ion concentration within the pores on applying a potential [18]. A similar idea is the so-called insertion model where a sufficient number of pores is initially empty at 0V and only wetted with electrolyte on applying a potential. In this case the overall number of ions within the electrode increases as well[19].

In some studies [20, 52] the pore swelling behavior of carbon is discussed as follows. It is suggested that in particular the electron insertion and extraction on the carbon electrode surface is responsible for the positive expansion for both positive and negative applied potentials. The band structure of graphite reveals a nearly fully occupied conduction band (corresponding to bonding states) and a nearly empty valence band (antibonding states) with the Fermi-level at the minimum of the electronic density of states (more in section 3.1.1). If electrons are inserted they occupy antibonding states, which weaken the chemical bonding. If electrons are removed from the valence band by applying a positive potential the chemical bonding is weakened as well. Although the bonding and antibonding states overlap at the Fermi-level this argumentation is still valid. Thus for both cases positive and negative applied potentials the surface stress is decreased, which enables expansion of the porous electrode. However, recently the occurrence of a contraction applying positive potentials was reported also for carbon electrode materials [20, 21], supported by DFT simulations on graphite intercalation compounds and carbon nanotubes [53, 54].

Another swelling effect of a porous system could be caused by an excess osmotic pressure, which occurs due to an excess concentration of ions caused by the double-layer formation on the pore walls. Due to entropic reasons (which lead to the exponential concentration decay) the potential of the diffuse layer does not reach zero at the center of the pore. Thus an excess amount of ions compared to the bulk electrolyte causes an excess osmotic pressure which may cause the porous structure to swell. The question is whether the amount of charge on the electrode side remains

constant, when going to smaller pores or if the inability to form the complete diffuse layer lowers the charge. The applied voltage could not anymore completely drop on the electrode/electrolyte interface. The charge density on the electrode surface would become lower and thus the capacity decreased [55].

Furthermore an effect called electrocapillarity, corresponds to the change of surface tension due to the repelling forces of charges with equal sign on the electrode surface [56]. For an ideally polarized electrode the Lippman equation is valid.

$$\left(\frac{\partial\sigma}{\partial\psi}\right)_{\mu} = -q \tag{34}$$

The change of the surface tension σ with the electric potential ψ is equal to the charge area density q on the electrode surface if the chemical potential and thus the concentration of the involved species is constant. Around the PZC the surface tension decreases parabolic in both directions, at positive and negative applied potentials. Deviations from this behavior are caused by specifically adsorbed anions [36, 38, 56].

3 Experimental

3.1 Materials

3.1.1 Electrode

The material characterization, presented in the following was mostly performed by the Energy Materials Group of Presser V., INM Saarbrücken. In order to obtain highest capacitance, high surface area materials like activated carbons are widely used as supercapacitor electrodes. The activated carbons YP-50 and YP-80 (Kuraray Chemicals Co, received as a powder) are mixed together with a small amount (5-10%) of binder (PTFE) and rolled to a film with 300µm thickness. The SEM images of the electrode film indicate the morphology of the electrode surface (Fig. 13). The carbon particles with a size in the micrometer range are hold together by the polymer binder.

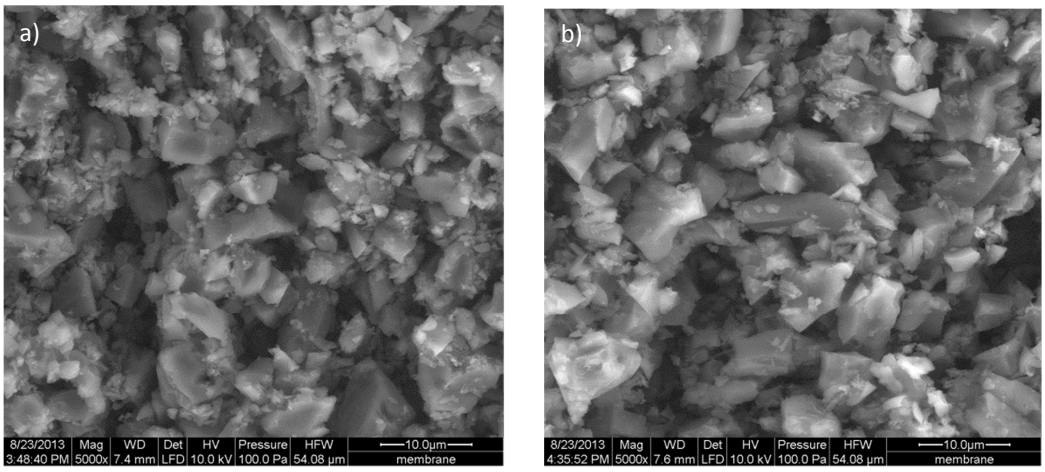

Fig. 13: SEM images of YP-50 (a) and YP-80 (b) electrode films. The images were provided by the Energy Materials Group of Presser V., INM Saarbrücken.

A significant amount of pore volume is represented by the space between the large carbon particles (macropores: >50nm). The large pore volume of smallest pores within the carbon particles is referred to as micro- (<2nm) and mesopore (2-50nm) volume.

The micro- and mesopore surface area of the carbon powders and prepared films are characterized by N2 gas sorption at -196.15°C using the Brunauer-Emmett-Teller-Equation (BET) and the quenched solid density functional theory (QSDFT). The pore size distributions in Fig. 14b indicate the small decrease of accessible pore volume in the carbon films compared to the

powder. YP-80 shows a bimodal distribution causing the larger specific surface area compared to YP-50. The specific surface area, the pore volume and the average pore size values are shown in Table 1. It is important to mention that pores larger than 20nm and in particular the volume of macropores are not contained in the values of Table1.

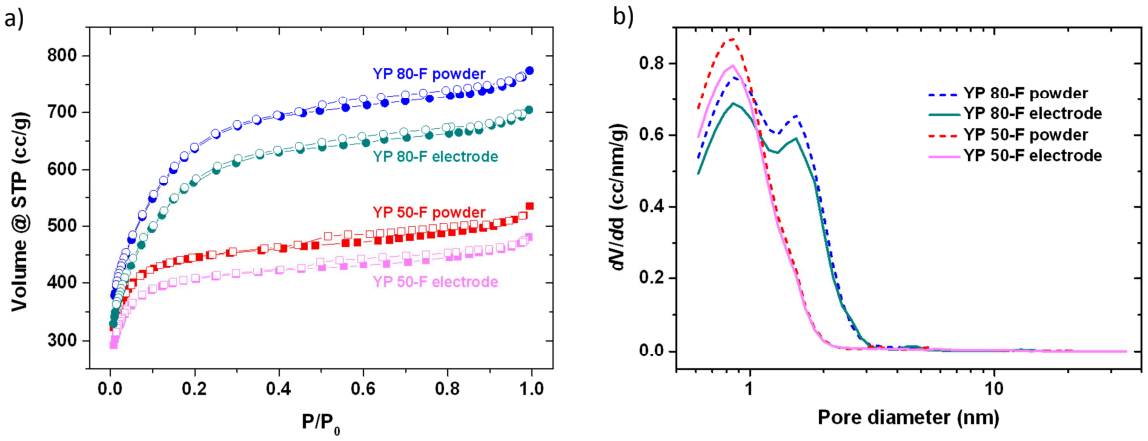

Fig. 14: N_2 sorption analysis of both YP-50 and YP-80 powders and electrode films. From the adsorption isotherms in a) the pore size distributions in b) can be calculated. The bimodal distribution for YP-80 is responsible for the larger surface area and the larger average pore size with respect to YP-50. The BET analysis was performed by the Energy Materials Group of Presser V., INM Saarbrücken.

Table 1: Results of the BET analysis of YP-50 and YP-80 powder and films

	Specific surface area (m^2/g)		**Pore volume (cm^3/g)**	**Volume-weighted average pore size d50 (Å)**
	BET	DFT		
YP-50 powder	1720	1520	0.73	10
YP-50 electrode	1560	1380	0.67	10
YP-80 powder	1955	1825	1.09	13
YP-80 electrode	1760	1660	0.99	13

Using the measured density values of the electrode films, the carbon skeleton density (density of "bulk" carbon) and the micro- and mesopore volume of Table 1 the macroporosity and micro-/mesoporosity can be calculated respectively. The carbon skeleton density was measured by Perre E. from the Presser Group using a Helium gas pycnometer instrument. From both the measured density of the YP-80 electrode and the carbon skeleton density, the specific volume was calculated. For the pore volume of the micro- and mesopores the data from the N_2 sorption analysis was used (Table 1). Both total and macropore volumes are obtained from simple subtractions, as shown below. The porosity values represent the fraction of the respective specific pore volumes with respect to the total specific electrode volume.

1. YP-80 electrode film:

Density YP-80 electrode: 0.427g/cm^3 -> 2.342 cm^3/g

Carbon skeleton density YP-80 electrode: 2.20g/ cm^3 -> 0.4545 cm^3/g

Pore volume micro- and mesopores: 0.99 cm^3/g

- Total Pore volume: 2.342 cm^3/g - 0.4545 cm^3/g = 1.8875 cm^3/g
- Total porosity: Φ_{total} = 1.8875/2.342 = **0.806**
- Macroporosity: 1.8875 cm^3/g - 0.99 cm^3/g = 0.8975 cm^3/g -> Φ_{macro}=0.8975/2.342=**0.3832**
- Micro- and Mesoporosity: $\Phi_{micro+meso}$ = 0.99/2.342 = **0.4227**

2. YP-50 electrode film:

Density YP-50 electrode: 0.615g/ cm^3 -> 1.626 cm^3/g

Carbon skeleton density YP-50 electrode: 2.20g/ cm^3 -> 0.4545 cm^3/g

Pore volume micro- and mesopores: 0.67 cm^3/g

- Total Pore volume: 1.626 cm^3/g - 0.4545 cm^3/g = 1.1715 cm^3/g
- Total porosity: Φ_{total} = 1.1715/1.626 = **0.7205**
- Macroporosity: 1.1715 cm^3/g - 0.67 cm^3/g = 0.5015 cm^3/g -> Φ_{macro}=0.5015/1.626=**0.3084**
- Micro- and Mesoporosity: $\Phi_{micro+meso}$ = 0.67/1.626 = **0.4121**

Table 2: Micro- Meso- and total pore volume of the activated carbons YP-50 and A1 YP-80 in comparison

	YP-50	**YP-80**
Micro- and Mesopore volume	0.67 cm^3/g	0.99 cm^3/g
Macropore volume	0.5015 cm^3/g	0.8975 cm^3/g
Total pore volume	1.1715 cm^3/g	1.8875 cm^3/g

The electric resistivity of both carbon films, measured with a four-point probe, is about 120 Ωcm (provided by Perre E., Presser Group, INM Saarbrücken). Compared to bulk graphite the resistivity is about 4 orders of magnitudes higher, mainly due to its highly defective structure. Compared to graphene, graphite reveals a non-zero density of states at the Fermi-level, causing the semi-metal behavior (Fig. 15). Subsequent discussions will be based on the electronic structure of graphite, although the structure of activated carbons might differ significantly (e.g. quantum capacitance of activated carbons can be explained by a DOS similar to the one in Fig. 15b [47]).

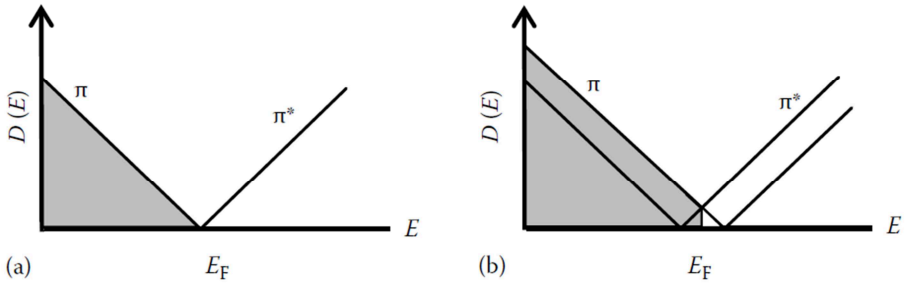

Fig. 15: Schematic representation of the density of states (DOS) for a single graphene layer (a) and graphite (b). With permission from [57]. © Taylor and Francis Group.

3.1.2 Electrolyte

A 1 molar CsCl aqueous solution was chosen to be the electrolyte. The selection of the electrolyte was mainly based on the electron density contrast of the ions for the 8keV X-ray beam. In order to be able to distinguish between cation and anion movement independent from each other the difference between the electron densities has to be large. Furthermore CsCl dissociates easily in an aqueous solvent. Cs^+ ions contain 54 electrons, while Cl^- ions contain 18 electrons. Since the ion diameters are similar (Table 3) [58], the electron density for Cs^+ ions is much higher. According to the two-phase model the scattering intensity is proportional to the square of the electron density. Thus the Cl^- ions should be nearly invisible with respect to the surrounding water molecules having 10 electrons. In Table 4 the estimated electron densities of all electrolyte species are given. The contrast matching of ions to the solvent molecules provides an elegant possibility to simplify things. Furthermore the ion mobilities of Cs^+ and Cl^- are rather similar (see Table 5).

Table 3: Crystal, Stokes and Hydrated radii of Cs^+ and Cl^- ions [58].

	Crystal radius [Å]	**Stokes radius [Å]**	**Hydrated radius [Å]**
Cs^+	1.69	1.19	3.29
Cl^-	1.81	1.21	3.32

Table 4: Estimated electron densities for all species within the electrolyte. Therefore the number of electrons was divided by the ion/molecular size. The ion/molecular size is in turn estimated by calculating the volume of a sphere with the crystal radius of the ion/molecule. The water molecule diameter is estimated from [59].

	Cs^+	**Cl^-**	**H_2O**
Electron density [e-/ Å^2]	2.67	0.72	0.71
(Electron density [e-/ Å^2])^2	7.13	0.53	0.50

Table 5: Diffusion coefficients and ion mobilities of Cs^+ and Cl^- at 25°, calculated by a molecular dynamics simulation [60].

	Diffusion coefficient D [$10^{-9}m^2s^{-1}$]	Ion mobility u [$10^{-8}m^2V^{-1}s^{-1}$]
Cs^+	1.88 ± 0.17	7.32 ± 0.66
Cl^-	1.77 ± 0.08	6.88 ± 0.31

3.2 The in-situ experiment

3.2.1 In-situ cell design

In order to be able to study the ion movement within the pores of the working electrode (WE) only, a special design for the electrochemical cell had to be developed. In Fig. 16 the general experimental set-up of the in-situ measurement is sketched on three different length scales. While the X-ray beam hits the sample a potential is applied via the potentiostat, which is connected to the cell via the current collectors (CC). The scattered intensity is recorded by the SAXS/WAXS detectors and the corresponding transmission by the photodiode, mounted on the beamstop. The cell consists of a stack of golden current collectors (CC), counter electrode (CE), working electrode (WE) and the ion separator in between, in order to prevent electrical contact between the electrodes (Fig. 16 center).

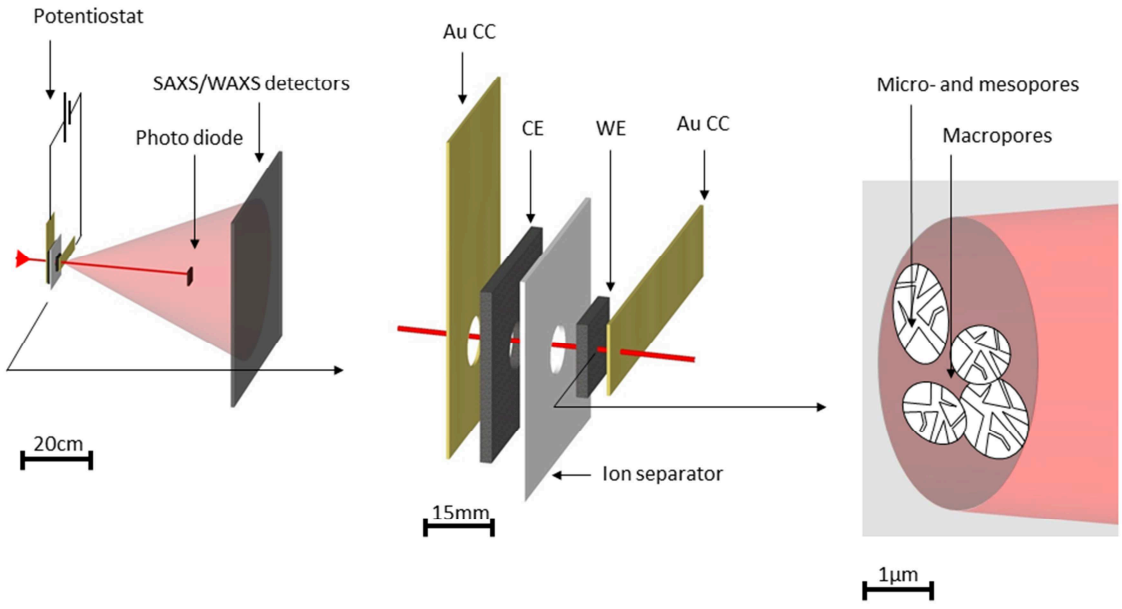

Fig. 16: Schematic representation of the In-Situ experiment, the In-situ supercapacitor cell and the different pore size levels investigated with scattering and transmission signals.

To ensure a low equivalent serial resistance (ESR), the layered components have to lie on top of each other. The hole (diameter of 12mm), which has to be cut in all layered materials except of the WE and the connected CC, enables the investigation of processes with X-rays within the WE only. As mentioned before, the carbon electrode consists of carbon particles which themselves exhibit micro- and mesopores. With scattering mainly the micro- and mesoporous structure is studied, while the transmission signal is sensitive to all pore size regimes, including the macropores (space between particles).

The stack (photograph in Fig. 17) is infiltrated with a 1M CsCl aqueous electrolyte and sealed by a plastic casing with either Kapton® or Scotch® tape windows at the spot where the beam hits the cell. Additionally the Scotch® tape enables an adhesion to the carbon on the one side and to the CC or the carbon on the other side. Hence the occurrence of an additional liquid layer in-between the layered components (Fig. 17, Fig. 16) is not possible, enabling quantitative estimations like the calculation of the ion concentrations. The in-situ cell is mounted on a special sample holder pressing the stack together to reduce the contact resistance.

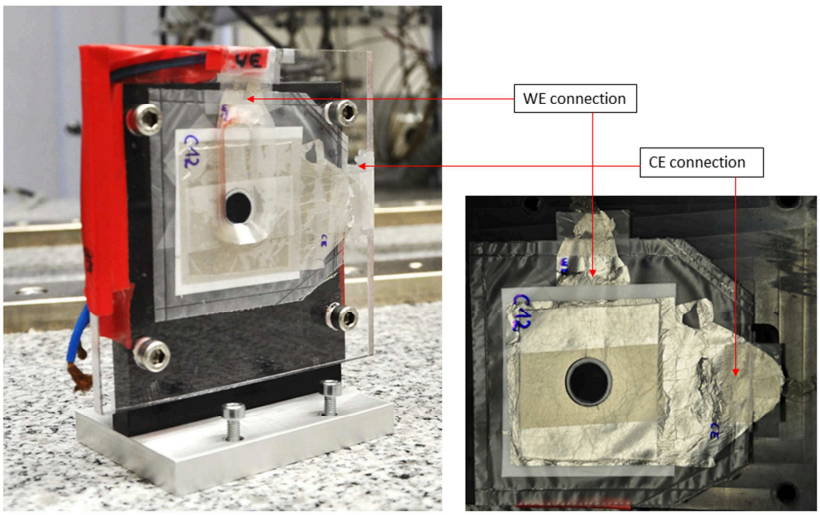

Fig. 17: The in-situ sample holder consists of two plates putting pressure on the multilayered supercapacitor cell. On the right a photo of the cell, sealed with a plastic casing and a Scotch® tape on top of the "measurement window" is given. In this case the platinum CCs are connected by additional platinum grids.

To prevent corrosion in the highly corrosive environment (Cl^-) either gold or platinum with a thickness of 100-200nm is used as the CC material. Platinum turned out to be the better choice, since gold corrosion was observed at large positive potentials. The WE with an area of 1.5x1.5cm is about 5 times smaller than the CE with an area of 3.5x3.5cm. Thus the recorded current is defined by the WE (smaller capacitance), the potential drop at the WE is about 5 times larger compared to the CE.

The hole cut into some of the materials may cause a kinetically driven local dependency of the ion transport on the WE. To investigate kinetic effects, caused by the carbon resistivity on the one hand and the limited ion diffusion within the electrolyte on the other hand, two different cell designs have been used (Fig. 18). The D8 cell design has no hole on the current collector behind the WE, in contrast to the D9 cell design. With the D9 design a possible influence of the low carbon conductivity to the local time constants of ion diffusion could be studied.

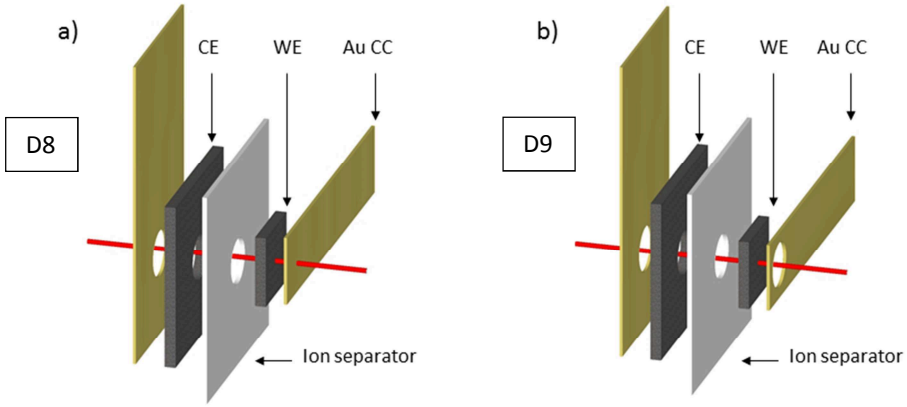

Fig. 18: In a) a sketch of cell design D8 is shown. The CC contacting the WE has no hole in the "measurement window" region; in contrast to cell design D9, as indicated in b).

To study the local dependency systematically three different spots on the WE, going from the center to the edge of the so-called WE measurement-window, are measured. As indicated in Fig. 19 approaching the edge of the measurement-window gives a smaller distance for ions to move from the CE to the WE.

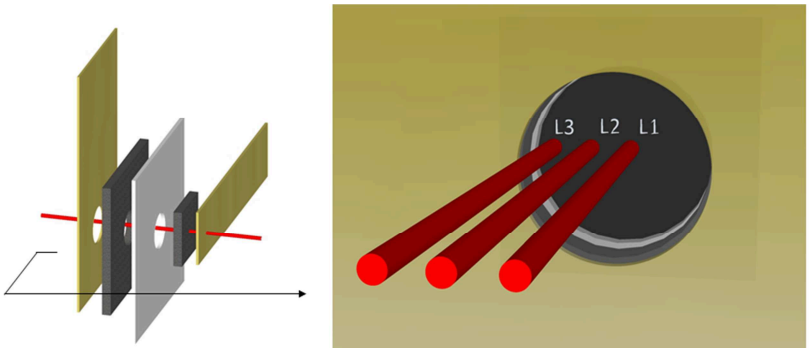

Fig. 19: A possible local dependency of the scattering and transmission signals were studied by measuring three different spots from the center to the edge of the WE "measurement window".

3.2.2 Experimental Set-Up at Elettra

In order to study changes on the scattering signal with a subsecond time resolution, an X-ray beam with high brilliance [Photons/mm^{2}srad^{2}0.1%bandwidth] is required [31]. Only modern Synchrotron X-ray sources are able to provide photonic fluxes enabling such in-situ experiments. Thus most experiments were performed on the Austrian SAXS Beamline at the Synchrotron facility ELETTRA in Trieste, Italy (Fig. 20).

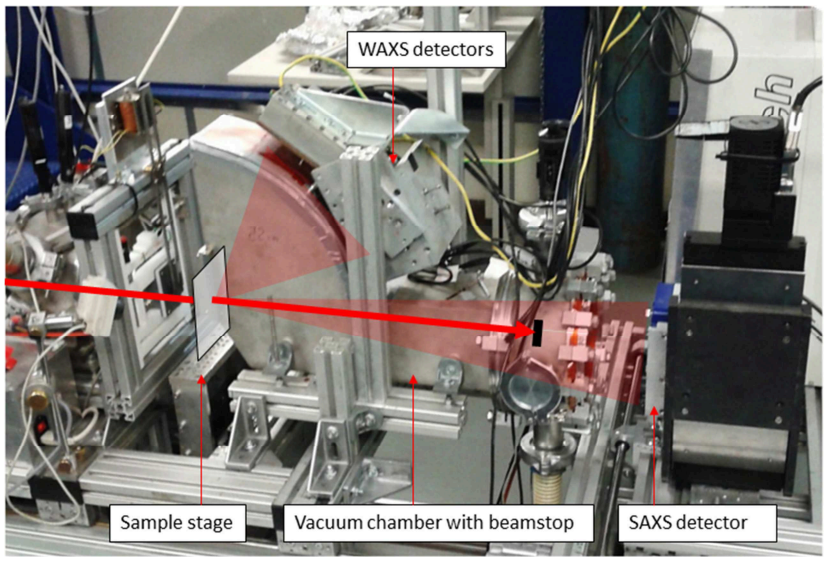

Fig. 20: Experimental set up at the SAXS Beamline at the Synchrotron Facility ELETTRA in Trieste, Italy.

In order to detect the scattering intensities for the SAXS and WAXS scattering angles of interest three detectors were recording simultaneously. A Pilatus single photon counting detector was used for the SAXS regime, while two CCD cameras recorded the WAXS regime [24].

3.2.3 Experimental Set-Up Nanostar

The photon flux of the in-house X-ray source (Nanostar) is too low to perform In-situ scattering experiments. Nevertheless using a strong scatterer (glassy carbon) behind the In-situ cell, transmission changes in the order of 0.01 and a time resolution of about 20 seconds are feasible (Fig. 21). Therefore the scattering intensity of the glassy carbon is integrated over the entire detector area, which is proportional to the sample transmission. In a good approximation the transmission is calculated by dividing the integrated intensity of “sample plus glassy carbon” through the integrated intensity of “glassy carbon” only [61]. In order to avoid air scattering and absorption the entire sample chamber is under vacuum during the measurements. Since the in-situ cell cannot be perfectly sealed the measurements have to be performed in air. In order to preserve ambient pressure at the sample stage a special conical vacuum chamber has to be

mounted. At the backside of the sample chamber the electric contacts of the potentiostat are guided through a small but covered hole, preventing X-rays from leaving the sample chamber.

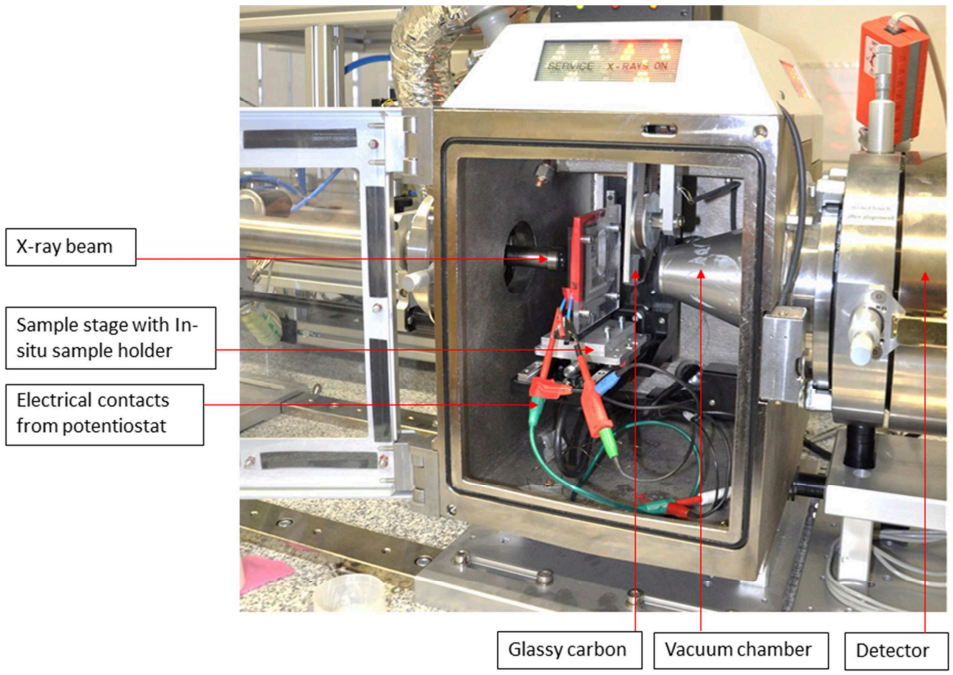

Fig. 21: Experimental set-up at the in-house SAXS/WAXS system. The use of liquid electrolyte requires measurements in air. Due to the limited photonic flux only transmission signals can be recorded with a time resolution of about 20 seconds. With scattering experiments only systems at equilibrium positions (constant potentials) can be studied.

3.2.4 Electrochemical methods

A large amount of different electrochemical methods to characterize EDLCs are nowadays available. Using impedance spectroscopy, complex equivalent circuit models were developed (e.g. Transmission Line model by de Levie [62]), which led to a deeper understanding of the diffusive ion transport within highly porous electrode materials. Cyclic Voltammetry (CV), Galvanostatic measurements and Chronoamperometry (CA) are direct methods to characterize the performance of an EDLC.

Cyclic Voltammetry corresponds to a measurement of the current while applying a triangular potential signal as indicated in Fig. 22a. The slope represents the potential scan rate and is often varied in order to investigate time-dependent effects due to diffusion. In Fig. 22b the corresponding Cyclic Voltamogramm with the Capacitor specific hysteresis is shown. An ideal EDLC without any faradaic charge transfer would lead to a constant positive current at positive potential and vice versa at negative potentials. The small deviations from this behavior when approaching +0.9V and -0.9V can be attributed to the onset of chemical reactions such as water

decomposition. If the time constant of the capacitor together with its serial resistance is negligible small, the CV curve would be rectangular shaped.

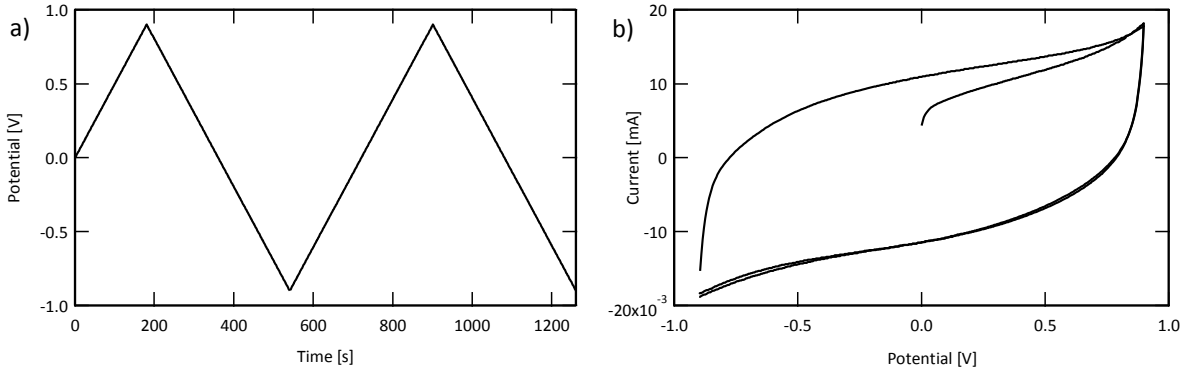

Fig. 22: In a) the applied potential signal with a scan rate of 5mV/s is indicated. In b) the corresponding cyclic voltammetry (CV) curve is shown. Pure capacitive behavior with negligible serial resistance would lead to a rectangular curve. The increase in positive and negative current at 0.9V and -0.9V respectively is typically for the onset of faradaic processes. In the case of an aqueous electrolyte this can be attributed to the decomposition reactions of water.

Chronoamperometry (CA) corresponds to a rectangular shaped applied potential signal, thus the charging behavior of the capacitor can be studied as a function of the applied potential. For a plate capacitor the current response upon applying any potential step is given in equation (17) in section 2.4.3. Since a realistic EDLC usually contains electrodes with a complex pore structure the behavior cannot be described with a single time constant (R*C). If the potential is kept constant for long enough time, the equilibrium behavior of the ion arrangement can be studied [63].

The widely used three-electrode configuration (WE + CE + reference electrode) enables the exact study of the current-voltage dependency of the WE. Due to simplicity a two-electrode cell configuration was used in the present work. Using a smaller WE causes a large potential drop at the WE and a current limited by the WE. Thus, an asymmetric two-electrode cell enables in a good approximation the study of the WE only. However, calculated capacitance values strongly depend on the electrode configuration used [64].

3.3 Data treatment

3.3.1 SAXS/WAXS data correction

Depending on the sample the absorption process influences the absolute scattering intensity, although it is independent on the scattering angle in the case of small angles. In particular for In-situ experiments, a transmission data correction is absolutely necessary because not only the

scattering signal but also the absorption changes during the experiment. Although absolute scattering intensities are not considered here, without transmission correction the actual scattering signal changes are overlaid by transmission changes and thus difficult to interpret.

An X-ray beam with the incident flux ϕ_0 in (photon/s/mm^2) and a cross section A in (mm^2) hits a sample with the thickness d. $\Delta\Omega = p^2/L^2$ represents a solid angle element of a detector pixel with the size $p\ (mm)$ at a specimen-detector distance of $L\ (mm)$. $\varepsilon(x,y)$ is the detector efficiency. Before a photon of the incident beam gets scattered at position x in the sample the beam is weakened by a factor $e^{-\mu x}$. After the scattering process the scattered beam is again weakened due to absorption, now by a factor of $e^{-\mu(d-x)}/\cos\theta$. The integral over all possible x-positions gives the intensity which is recorded on the detector at the angle θ ($Q \sim \sin\theta$).

$$I(\theta) = \int_0^d \phi_0\, A\, \varepsilon(x,y)\, \Delta\Omega\, e^{-\mu x}\ \frac{e^{-\mu(d-x)}}{cos\,\theta}\ \frac{d\Sigma}{d\Omega}\ dx \tag{35}$$

The instrumental constant K is defined as follows.

$$K = \phi_0\, A\, \varepsilon(x,y)\Delta\Omega \tag{36}$$

At small angles $\cos\theta \cong 1$, the integration gives

$$I(\theta) = K\, d\, e^{-\mu d}\frac{d\Sigma}{d\Omega} = K\, d\, \tau\frac{d\Sigma}{d\Omega}, \tag{37}$$

with τ being the sample transmission. Since not only the scattering intensity but also the transmission signal is changing with time, the transmission might have a big influence on the time dependent scattering intensity. Thus a normalization of the as measured intensity is done by a simple division of the transmission τ. The effect of a possible increase of the entire scattering intensity $I(Q)$ due to a decreased absorption coefficient is filtered out. In practice for an In-Situ measurement the scattering intensity and the corresponding transmission value are recorded simultaneously. In order to be able to compare the scattering intensities of measurements with different exposure times, the as-measured scattering intensity is additionally divided by the exposure time. If absolute intensity measurements would be requested several methods for the determination of the instrumental constant K are possible [61]. The instrumental constant changes slightly due to changes of the incident flux ϕ_0. These changes are considered for the correction of both transmission values and scattering intensities. Apart from the primary beam the instrumental constant K is assumed to stay constant when changing the sample. It is not necessary to determine K for our purposes [65].

3.3.2 Analysing the In-Situ Experiment

In Fig. 23 the measured and spherical averaged scattering intensity of a working cell with the activated carbon YP-80 infiltrated with 1M CsCl aqueous electrolyte at 0V is shown. Due to the

high brilliance of the Synchrotron X-ray beam such frame needs a recording time of only a few seconds. On the right the evolution of a scattering curve over time is visualized in a 3D color coded plot (top view). The time dependent changes of the as-measured scattering intensity correlates to the applied potential signal. As indicated both SAXS and WAXS Q-regions were recorded simultaneously. In addition the transmission was measured by a photodiode mounted on the beamstop. The scattering signal recorded with the second CCD camera (WAXS: >30nm^{-1}) is not shown and in the following skipped for most discussions.

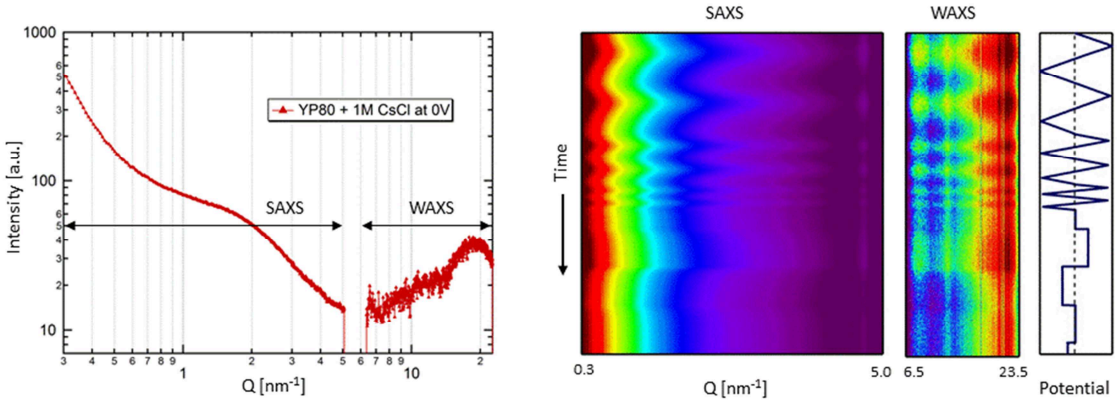

Fig. 23: The scattering curve I(Q) (here: spherically averaged, transmission and background corrected) was recorded every 10s making changes in the intensity visible, indicated in the color coded plot on the right. The large changes of the as-measured intensity (here: spherically averaged, but not transmission and background corrected) in the color coded plot are mainly caused by changes of the sample's transmission and correlate with the applied potential signal. Note the classification in SAXS and WAXS Q-regions, which were recorded with different detectors.

As stated above the transmission signal changes if the applied potential is changed. Thus every recorded scattering curve has to be corrected with the corresponding transmission value (transmission correction). In addition the scattering signal was divided by the exposure time (time normalization). Furthermore the scattering intensity is multiplied by a factor describing the changes of the incident beam flux. The sample thickness was assumed to stay constant between the various samples. In fact the electrodes expand to a small extend during cycling, but the dimensional changes due to strain cannot cause transmission changes, since the overall amount of matter (atoms) is rather constant. Indeed, small changes of the total number of electrons are expected due to the sample expansion in lateral direction, while the irradiated area on top of the sample remains constant. Still, this effect is negligible (a lateral strain of 10^{-3} would cause a relative change of the electron number of about 10^{-6}).

Beside the transmission correction the scattering contribution of the in-situ cell (Scotch® or Kapton® tape) and the surrounding air have to be subtracted (background correction). Hence, the corresponding reference measurements have to be performed. Since only the WE filled with

electrolyte is the system of interest, the scattering curve of the gold layer (no gold layer for cell design D9) together with two layers of Kapton® tape fixed in the in-situ sample holder were subtracted after transmission correction and time normalization (layered cell designs, section 3.3).

After transmission correction the time- and potential dependent changes in the scattering curves are very small. In order to investigate the small changes systematically, integral parameters were determined, describing all possible changes of the scattering curve within a specified Q-regime. Usually these parameters are not calculated for a defined Q-regime, as discussed below [66]. The integrated intensity $\tilde{I}$ corresponds to an integration of the scattering intensity $I(q)$ within a specified Q-regime.

$$\tilde{I} = \int_{Q1}^{Q2} I(q) q^2 dq \tag{38}$$

An increase of the integrated intensity represents an increase of the average intensity value within the defined region and is sketched in the right inset in Fig. 24. The so-called correlation length L_c, given in eqn. (39), corresponds to the ratio of the first and second moment of the scattering curve and is sensitive to a shift of the “center of mass” of the specified region of the scattering curve I(Q).

$$L_c = \frac{\int_{Q1}^{Q2} I(q) q dq}{\int_{Q1}^{Q2} I(q) q^2 dq} \tag{39}$$

As indicated in the inset in Fig. 24 an increase or decrease of the correlation length can be related to a change of the slope of the scattering curve in a defined Q-regime. Any errors in the scattering curve that are caused by wrong transmission corrections or other normalizations are cancelled out when calculating L_c.

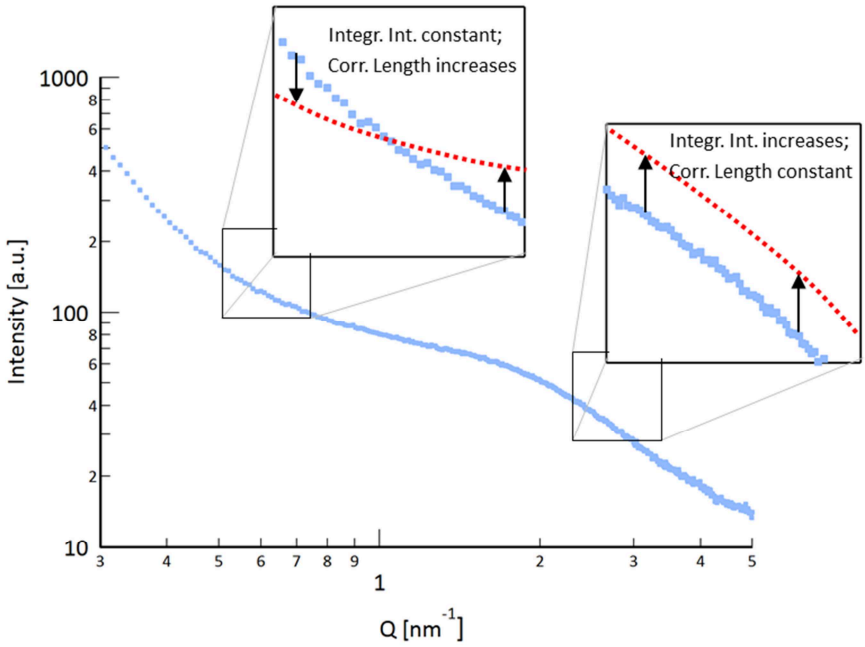

Fig. 24: SAXS scattering curve I(Q) with two sketches in order to explain the integral parameters Integrated Intensity and Correlation Length. A change of the center of mass correlates with a Correlation Length change, indicated by the hypothetical curve in red in the left inset. A change of the mean intensity correlates with a change in the integrated intensity, indicated by the hypothetical curve in red in the right inset.

Looking at the time (potential-) dependency of these parameters in different defined Q-regimes enables the study of scattering curve changes taking place on different length scales in real space.

Integrated intensity and correlation length are two complementary integral parameters which qualitatively contain the information needed to describe any change of the I(Q) curve. In addition to these two signals the transmission signal represents another time- and potential dependent quantity, containing further integral information on ion concentration changes. In fact $\tilde{I}$ and L_c as defined in the literature [66] are usually integrated from 0 to ∞. In this case the absolute values of $\tilde{I}$ and L_c can be related to the total number of electrons and the mean width of the correlation function $\gamma(r)$ of the irradiated structure, respectively [66]. Here we are only interested in relative changes of different regions on the scattering curve. Using the integral parameters enables the study of changes of a defined region on the scattering curve. Basically other parameters describing the qualitative changes of the scattering curve could have been used as well. Those changes and their time dependencies might be rather different for different Q-regions and are in general rather complex to interpret.

4 Results and Discussion

4.1 Ex-situ scattering experiments

Before investigating potential dependent changes of the scattering curve, the carbon electrode in air and filled with electrolyte at 0V, have to be studied.

In Fig. 25 the SAXS curve of the dry activated carbon YP-80 is shown. The high intensity at small angles can be attributed to the influence of the scattering from the carbon particles [67]. Since these particles have diameters in the micrometer range, it is the porod regime of the carbon particle scattering intensity contributing to the overall scattering intensity. The porod regime is usually described by a power law with an exponent of -4, requiring sharp interfaces between the two phases causing the scattering. Beside the particle contribution at small angles the SAXS-scattering intensity of highly porous carbons is often fitted with the Debye-Anderson-Brumberger (DAB-model), derived for the scattering on materials with randomly distributed pores [68].

$$I(Q) = \frac{a^4 B}{(1+a^2Q^2)^2} \tag{40}$$

Adding the particle porod contribution and a constant background to eqn. (40) gives a model describing the entire SAXS intensity indicated in Fig. 25 [22, 67, 69].

$$I(Q) = \frac{A}{Q^4} + \frac{a^4 B}{(1+a^2Q^2)^2} + BG \tag{41}$$

Fitting such models to the scattering intensity of activated carbons does not lead to a fundamental understanding of the carbon structure. The main fit parameter of the DAB model is the correlation length a, which can be related to the average pore diameter (do not confuse with the correlation length introduced in section 3.3.2). The DAB-model assumes an exponentially decaying correlation function ($\gamma(r)$ as described in section 2.2.4), which is most probably not true for the porosity of an activated carbon. Still, the fit (black curve in Fig. 25) works quite well, resulting in a correlation length of $a=0.359nm$. The time-dependent changes on the scattering curve (relative changes in the order of 10^{-2}) are rather small for all experiments in the present work. Hence, the quality of the fit is too bad to systematically study the fit parameter changes upon charging the in-sit cell.

A power law fit ($I(Q)=A*Q^{exp}$) performed for the Q-region between 3.2-5nm^{-1} gives an exponent of -2.85, which means a large deviation of the porod behavior. The two-phase model requires sharp interfaces, which is not true when going to larger Q-values where the electron density distribution

of the single atoms gets more and more resolved. Ruland et al. introduced an explanation to the non-integer exponents in the porod regime [70, 71]. The electron density fluctuations within the carbon matrix as well as the smoothening of the electron density discontinuity at the interfaces cause another Q^{-2} term added to the Q^{-4} term. However, a quantitative analysis of the SAXS curve, extracting parameters like the surface to volume ratio of the pore structure is difficult. Due to the limited significance of the model fit parameters the study of the relative SAXS curve changes using integral parameters seems to be the best strategy.

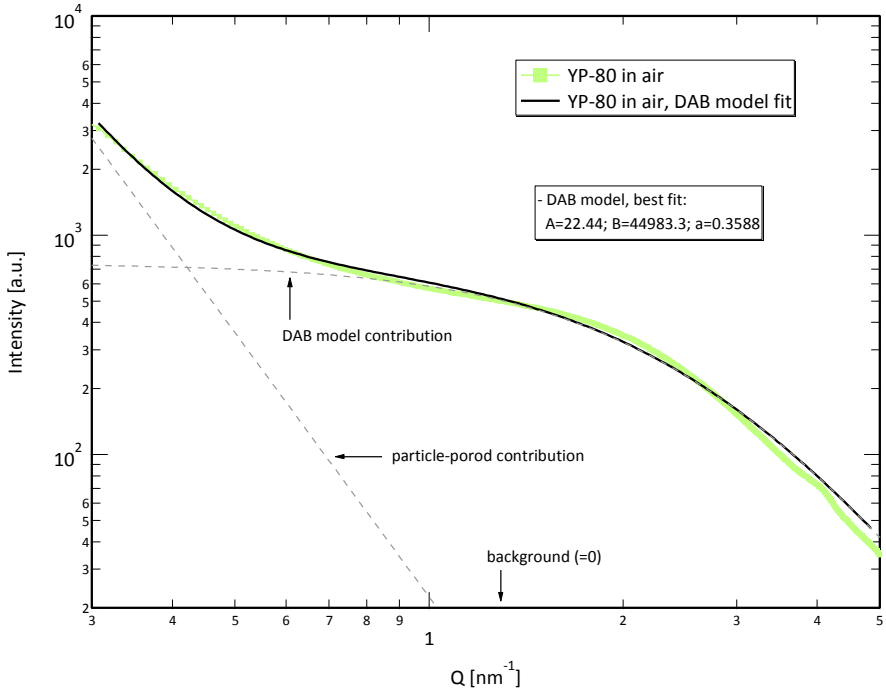

Fig. 25: The SAXS intensity of YP-80 in air (green) is fitted with the DAB model, according to eqn. (41) (black). The greyish dashed curves correspond to the DAB-model contribution (micropores) and the particle porod contribution. The fit parameters are given in the textbox on the upper right.

In Fig. 26 the scattering intensity I(Q) of the two activated carbons YP-50 and YP-80 for the SAXS (0.3-5nm^{-1}) and the WAXS Q-regime (6.5-23.5nm^{-1}) is shown. In dark-green and dark-blue the fits according to the DAB model for the SAXS Q-regime between 0.3 – 5nm^{-1} are indicated. The differences between the two carbons can be attributed to the difference in the pore size distributions measured by nitrogen adsorption (section 3.1.1). Indeed the correlation length for YP-50 is smaller, meaning that the average pore size is smaller as well. Neglecting the Q-region below 1nm^{-1}, the YP-50 scattering intensity is slightly shifted to higher Q-values, which is reasonable due to the smaller average pore size. The differences at small Q-values might be caused by the different electron density contrast between particle and macropores. YP-80 exhibits a significantly larger porosity leading to a lower mean electron density of the entire

particle. The electron density contrast with respect to the empty macropores is therefore lower, leading to a lower intensity from particle scattering. The particle sizes of both carbons are similar (SEM figures, see section 3.1.1). In some studies the particle porod contribution was subtracted in order to obtain scattering curves caused by micro- and mesopores only [69]. However, to subtract this contribution an extension of the Q-region to smaller scattering angles would be necessary.

In the WAXS Q-regime around 18nm^{-1} a maximum in the carbon structure factor is visible, corresponding to the stacking of graphene like carbonaceous planes (002-reflection) [72]. The degree of order is very low; sometimes the carbon is referred to as “turbostratic” [73, 74]. In a graphite crystal the stack of graphene-like planes would be perfectly ordered. Since the correlation peak for YP-50 is more pronounced the crystalline ordering is higher. The broader peak of YP-80 indicates most probably a smaller correlation between the graphene layers (or smaller domains where the crystalline order is to some extend maintained).

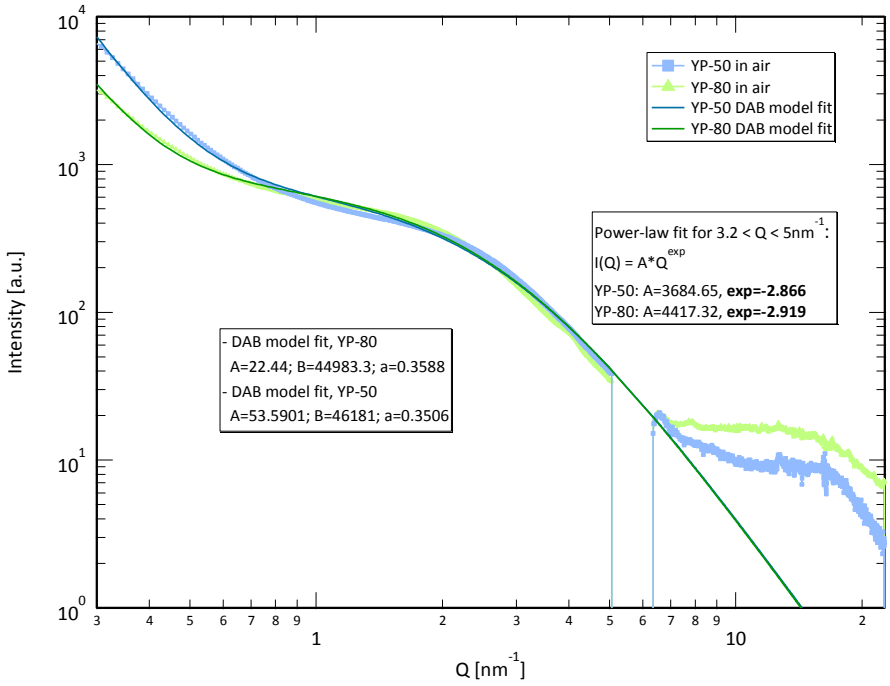

Fig. 26: Scattering intensity for both WAXS and SAXS Q-regions for both activated carbons YP-50 and YP-80 in air. Small deviations of the two scattering signals in the SAXS Q-regime can be explained qualitatively when comparing the pore size distributions measured with nitrogen adsorption. The difference in the WAXS Q-regime indicates a difference in the atomic structure of the carbons. The scattering intensities of the WAXS signals are shifted manually in y-direction but equally for both carbons with respect to the SAXS signal.

In Fig. 27 the SAXS and WAXS scattering curves of the two activated carbons YP-50 and YP-80 infiltrated with the 1M CsCl electrolyte are shown. The greyish curves in the background correspond to the YP-80 and YP-50 scattering curves in air. Wetting the activated carbons with

electrolyte leads to a strong decrease of the SAXS scattering intensity. According to the two-phase model of Small-Angle Scattering (section 2.2.3) the electron density contrast $\Delta\rho$ between pores and matrix (carbon atoms) determines the absolute value of the scattering intensity. If the pores are filled with electrolyte the electron density in the pores increases compared to the empty pore. Since the mass density correlates with the electron density a simple contrast estimation is possible. The carbon matrix is assumed to have a density of about 2.2g/cm^3 (according to the skeleton density measurements, shown in section 3.1.1), which corresponds to the density of a monolithic graphite block. The neutral 1M aqueous CsCl electrolyte exhibits a density of about 1.13 g/cm^3 – upon applying a potential the ion concentration may change and thus the electron density within the pore. However, since the electron density contrast $\Delta\rho$ between matrix and pores filled with electrolyte decreases compared to the empty carbon structure, the entire scattering curve is decreased in intensity.

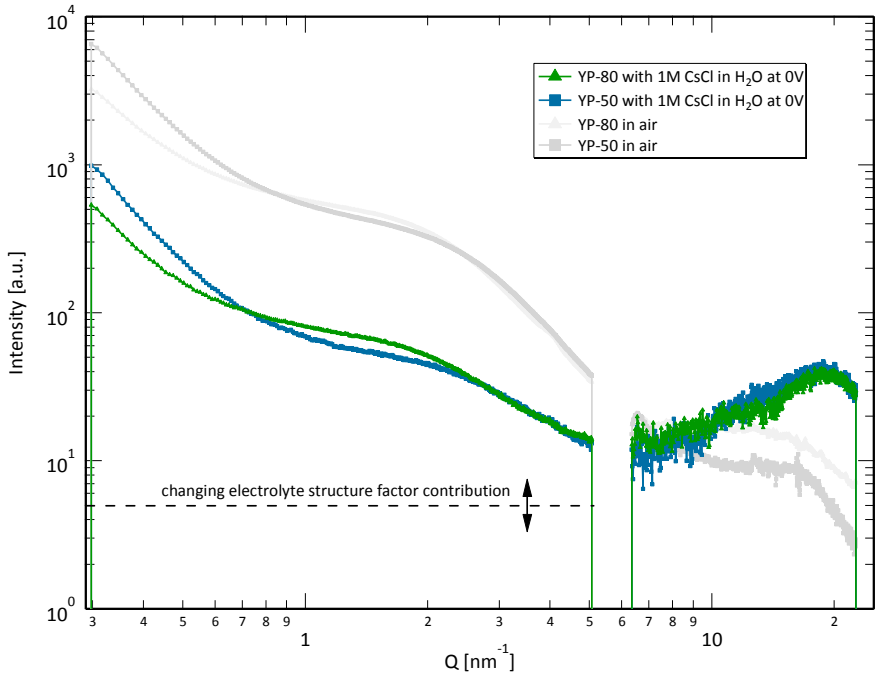

Fig. 27: Scattering intensity I(Q) for both activated carbons YP-50 and YP-80 infiltrated with electrolyte. The SAXS signal looks similar to the dry carbons although the intensity is in general lower due to the different electron density contrast between pores and matrix. In the WAXS signal mainly the scattering of the liquid electrolyte (electrolyte structure factor) is visible. The possible influence of the electrolyte structure factor in the SAXS-regime is indicated with the dashed black line. The scattering intensities of the WAXS signals are shifted manually in y-direction but equally for both carbons with respect to the SAXS signal.

Compared to the dry carbon the slope (in the log-log plot) in the Q-region from 3-5nm^{-1} (power law behavior) is much smaller. The smaller slope can be attributed to the occurrence of a constant intensity contribution of the electrolyte structure factor. In the following section the explanation

for this statement is developed. Beside this contribution the porous carbon filled with electrolyte gives a SAXS curve qualitatively equivalent to the dry carbon. The dashed black line indicates the constant electrolyte structure factor contribution, which might change upon changing the applied potential and thus the ion concentration within the electrolyte.

In the WAXS regime mainly the structure factor of the electrolyte contributes to the scattering intensity. Around 20nm^{-1} the first structure factor maximum of the aqueous electrolyte is located. The contribution of the carbon structure factor intensity is smaller and plays only a subsidiary role for the electrolyte wetted carbons.

In order to investigate the contribution of the liquid structure factor in the WAXS regime, liquid measurements in quartz glass capillaries (diameter about 1mm) were accomplished at the Nanostar SAXS/WAXS system. Distilled water in comparison to aqueous CsCl electrolytes with three different concentrations were measured (Fig. 28). The salt concentration within the aqueous solvent was varied in order to investigate the influence of the ions on the scattering intensity. To record the large range of Q-values two measurements of each specimen were performed for both 6cm and 25cm sample-to-detector distance. As explained above Cl^- ions are nearly invisible with respect to water. Thus only Cs^+ can significantly influence the scattering intensity. As stated above the peak around 20nm^{-1}, visible for both bulk electrolyte and electrolyte within the carbon, clearly represents the first structure factor peak of the liquid electrolyte [30]. In section 2.2.2 the structure factor for a liquid or amorphous solid was introduced. The increasing intensity of the electrolyte scattering curve with increasing CsCl concentration enables an understanding of the ion contribution to the scattering intensity at smaller angles. A concentration of 1 mol/l means one Cs^+ ion and one Cl^- ion per 55 H_2O molecules. Thus the mean distance of one ion to the other is rather large and any spatial correlation in the bulk electrolyte becomes unlikely. As explained in section 2.2.4 a completely uncorrelated solution of particles (in particular Cs^+ ions) causes a constant scattering (Laue Scattering) depending on the concentration of particles/ions. Only at large angles the ion scattering contribution reveals an intensity decay due to the atomic form factor. The atomic form factor considers the spatial extension and non-uniformity of the electron density within a specified atom [27].

The scattering curve of a bulk electrolyte is a superposition of the water scattering curve and the contribution of ion Laue scattering (constant in Q). The latter depends on the Cs^+ concentration, confirmed by the intensity increase of the three different electrolyte measurements in Fig. 28. The curves of the SAXS Q-region exhibit higher noise (in particular for the 1M concentration, due to the high transmission) and were measured with a larger sample-to-detector distance. The scattering intensity of the bulk electrolyte is rather constant for all Q<9nm^{-1}. Thus, a considerable constant intensity caused by the structure factor of the electrolyte within the carbon pores, is also

assumed in the SAXS curve of the working EDLC. The grey curve represents the scattering intensity of the electrolyte-filled carbon indicating the large conformity to the bulk electrolyte measurements at large Q-values. Indeed the structure factor peak within the carbon seems to be slightly shifted to lower Q-values, which is not surprising due to the interaction of water molecules with the carbon surface.

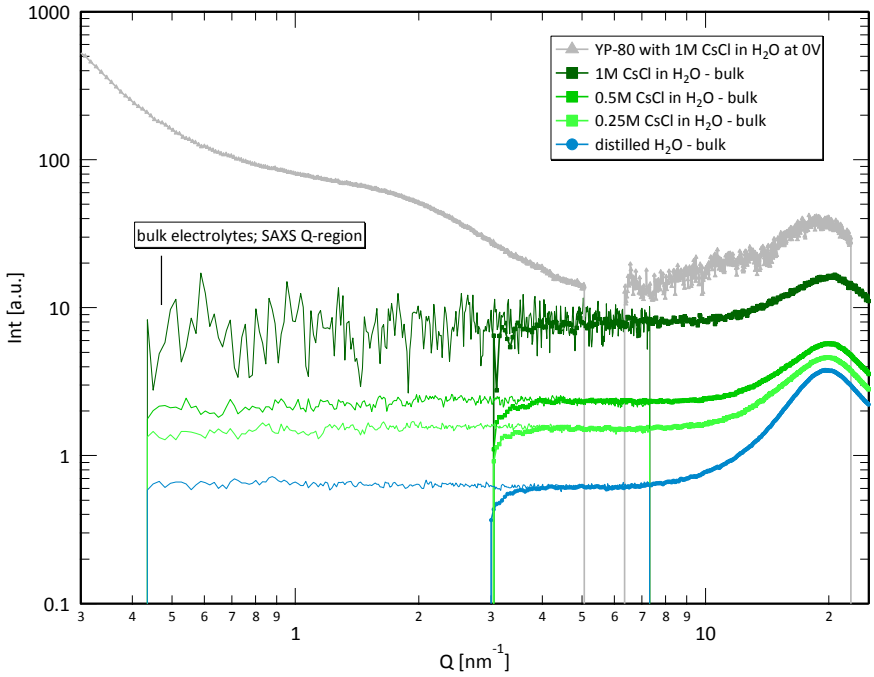

Fig. 28: Scattering intensity of bulk water and bulk electrolyte with three different (0.25, 0.5 and 1M) salt concentrations. With increasing salt concentration the scattering intensity generally increases. In grey the scattering curve of YP-80 infiltrated with a 1M electrolyte is given, shifted arbitrary in y-direction for better visualization.

In the following the time- and potential dependent In-situ experiments are analyzed using integral parameters as described in section 3.3.2. In Fig. 29 a rough Q-regime classification for the SAXS Q-regime (in red) and a more detailed classification for both SAXS and WAXS Q-regimes (in black) is given. The Q-regimes are in the SAXS region are equidistant. In the WAXS region the width of the Q-regimes is varied, depending on the feature or behavior of I(Q) that wants to be tracked. The WAXS Q-regime recorded by the second CCD camera (28-40nm^{-1}, Q-D and Q-E) is skipped for most of the following evaluations. Nevertheless, for the sake of completeness the time-dependency behavior of this Q-regime is presented for one measurement in the following chapter.

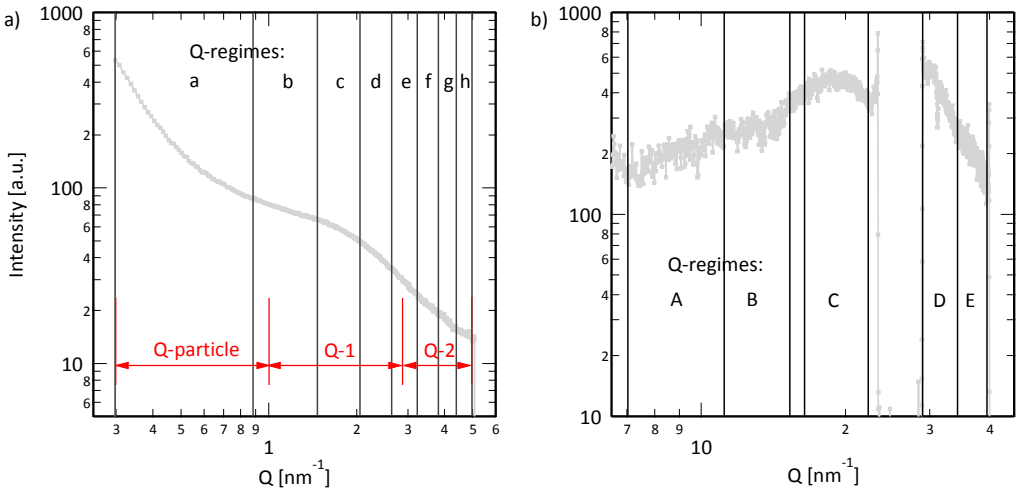

Fig. 29: In a) the Q-regime classifications of the SAXS region is shown. The red arrows represent a rough classification the black letters a more detailed one. In b) the classification for the WAXS Q-regime is given.

4.2 In-situ experiments

In the following the time- and potential dependent behavior of the integral parameters, for applying a combined CV and CA potential signal, is analyzed. The integrated intensity and the correlation length for the SAXS Q-regimes Q-1 and Q-2 (see Fig. 29) are calculated; most information can be extracted from these two regimes. The measurements were performed on three different spots on the WE (going from the center towards the edge of the working electrode measurement window) for the two cell designs D-8 and D-9 as described in section 3.2.1. Since the physical meaning of the absolute $\tilde{I}$ and L_c values are lost when calculating them for a restricted Q-region, both signals are normalized and only relative changes studied. The two integral parameter signals are the result of several potential driven processes taking place simultaneously. Furthermore each process can affect the scattering signal in more than one way. For instance, the change of the ion concentration within the micropores can cause a change in the electron density contrast according to the SAXS two-phase model and simultaneously change the flat intensity contribution of the electrolyte structure factor. In general it's hard to distinguish between all contributions of the superimposed $\tilde{I}(t)$ and $L_c(t)$ signal. However, investigating the changes of different Q-regimes and looking particularly on the time-dependency provides some information to estimate the origin of the contributing processes.

The only measurement shown in this work for the activated carbon YP-50 is given in Fig. 30. For several measurements the behavior of YP-50 and YP-80 was found to be rather similar. Hence, the most important measurement series presented in the following (D8 and D9) was performed using YP-80 only. However, the integral parameters of the Q-regimes Q-1 and Q-2 for a long-term CA

measurement with different potential step heights indicate the need of higher applied voltage in order to resolve structural changes. In general the behavior of the Q-1 and Q-2 signals differ significantly. The correlation length signal of the Q-1 region show features (in particular around 20000s) so far not explainable by the electrolyte structure factor or the contribution from the carbon pore structure filled with electrolyte ("Two-phase-model contribution"). The drift of $L_c(t)$ to lower L_c values is probably caused by a slight drift of the incident X-ray beam. At large potentials (+1V) the cell broke, due to corrosion of the golden current collectors. Hence the distinct features at these potentials are not of interest.

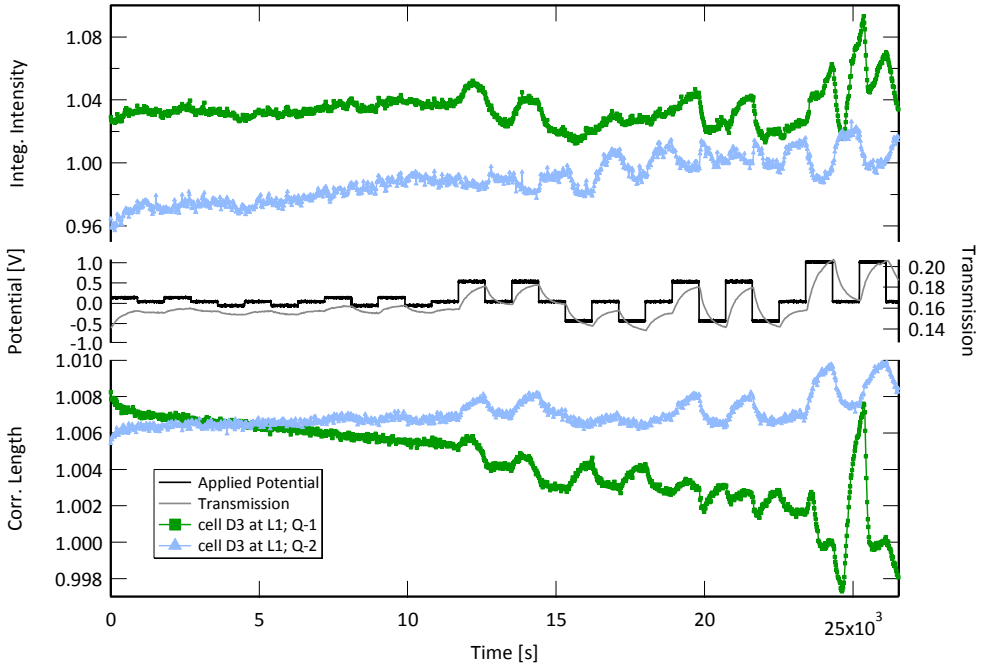

Fig. 30: Integral Intensity and Correlation length signals for a long-term CA measurement are given for the Q-regimes Q-1 and Q-2 for the cell D3 (YP-50) at position L1 (center of the WE as explained in section 3.2.1). Cell D3 corresponds to cell design D8 as explained in section 3.2.1. The integral SAXS signals are shifted arbitrarily in y-direction for better visualization. The scattering curves are time normalized, transmission and background corrected (section 3.3.1).

An equivalent long-term measurement performed for the activated carbon YP-80 exhibit qualitatively similar integral parameter behavior as for YP-50 (Fig. 31).

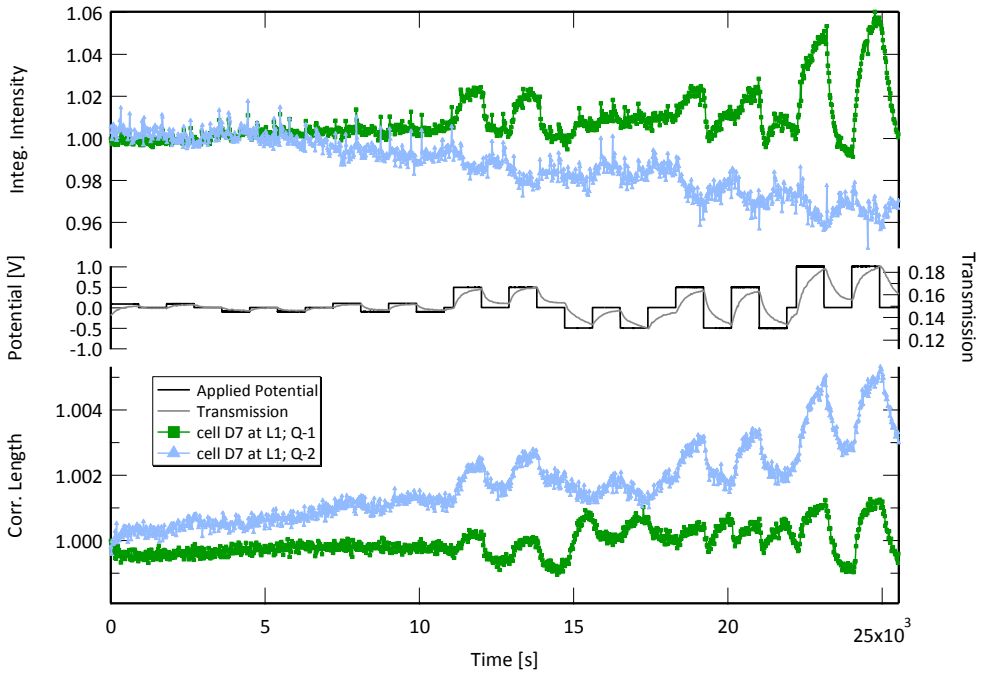

Fig. 31: Integral Intensity and Correlation length signals for a long-term CA measurement are given for the Q-regimes Q-1 and Q-2 for the cell D7 (YP-80) at position L1 (center of the WE as explained in section 3.2.1). Cell D7 corresponds to cell design D8 as explained in section 3.2.1. The integral SAXS signals are shifted arbitrarily in y-direction for better visualization. The scattering curves are time normalized, transmission and background corrected (section 3.3.1).

In Fig. 32 the time dependent signals of the center position L1 on the WE of cell D8 is shown. In the center of the graph the applied potential together with the measured transmission is indicated. The negative logarithm of the transmission signal is in a good approximation proportional to the Cs^+ concentration within the irradiated volume. The contribution of Cl^- to the transmission value is about ten times lower (see Table 6 in section 4.3.2) [33]. Due to the small absolute transmission changes the transmission signal (as shown in most plots) correlates with the inverse of the Cs^+ concentration (the non-linearity due to the exponential function is negligible, a detailed explanation is given in section 4.3.2). However the transmission signal shows the expected time-delay with respect to the potential, ascribed to the diffusive nature of the ion transport. Faster cycling (5, 10, 20mV/s) leads to a smaller transmission change.

The integrated intensity signal $\tilde{I}(t)$ (top) is in particular for Q-1 difficult to interpret. $\tilde{I}(t)$ contains the SAXS intensity changes due to ion concentration dependent changes of the electron density contrast between pores and carbon matrix (two-phase-model contribution). This contribution is expected to change periodically with minima at negative and maxima at positive applied potentials. If the Cs^+ concentration is increasing (negative applied potentials) within the pores, the electrolyte electron density will increase with respect to the carbon electron density. Therefore the contrast is lowered (and vice versa at positive applied potentials). The Q-2 regime indeed

reveals a periodic behavior than the Q-1 signal, but with maxima at negative and minima at positive applied potentials. Due to the strong decay of the SAXS two-phase-model contribution at larger Q-values (according to the SAXS curve as shown in Fig. 25) the influence of the structure factor intensity is believed to become stronger at large Q-regimes (Q-2). The correlation length signal of Q-1 shows strong peaks at negative applied potentials having a time-delay with respect to the potential signal. The time-delay of the transmission signal is larger (indicated with red arrow). The different time-delay of the correlation length signal and the transmission signal with respect to the applied potential in the case of negative potentials is indeed remarkable. At positive applied potentials no difference is visible. The signal for Q-2 shows a periodicity same as for the applied potential signal and fits to the maxima of the Q-1 signal at positive potentials. Obviously the Q-1 signal is the superposition of the signal of Q-2 (blue curve) plus another contribution having a different time-constant compared to the transmission signal (red ellipse).

Here and for all future discussions the time-delay corresponds to minima or maxima of a signal with respect to the minima or maxima of the potential signal in a CV cycle. Since the time constant of the exponential-like signals at applied potential steps (CA) is more difficult to evaluate, the minima/maxima time-delay at CV measurements seem to be a good way to study the diffusive behavior of the ion transport. Still, one has to be careful when comparing the maxima/minima of the various signals with each other, since the physical origin may be completely different. Even if the ion transport would exhibit only one time constant, the recorded signals (e.g. $\tilde{I}$, L_c, transmission) may have different time-delays due to the different physical mechanisms enabling the tracking of the ion transport.

The signals at the L2 position (Fig. 33) differ from the signals at L1. Still the integrated intensity signal is for both Q-regimes difficult to interpret and most probably a superposition of several contributions. At least one of the contributions to the integral parameter signals seems to have a different time-constant compared to L1, changing the entire appearance of the signal. The integrated intensity signal for Q-1 consists of a periodic contribution with maxima at positive potentials. Additionally a small peak occurs at negative applied potential. Despite of this small peak, the behavior could be explained by the change in the electron density contrast between filled pores and carbon matrix. At low Cs^+ concentration within the pores the electron density contrast and thus the scattering intensity should be highest, which is observed for the Q-1 signal. At larger scattering angles the influence of the electrolyte structure factor intensity becomes larger. It is expected to change in the opposite way, having maxima for high Cs^+ and minima for low Cs^+ concentrations. Both Q-1 and Q-2 correlation length signals show a similar behavior as those observed at the L1 position. By naked eye there is no difference between the time delays of the correlation length and the transmission signal visible, at both positive and negative potentials.

The same measurement series was performed at WE-position L3, which is the closest position to the ion separator and CE edge. The behavior for the integrated intensity and the correlation length looks qualitatively very similar to those of position L2 (Fig. 33, 34). Also the time-delay behavior for the transmission and the two integral parameters is comparable to L2.

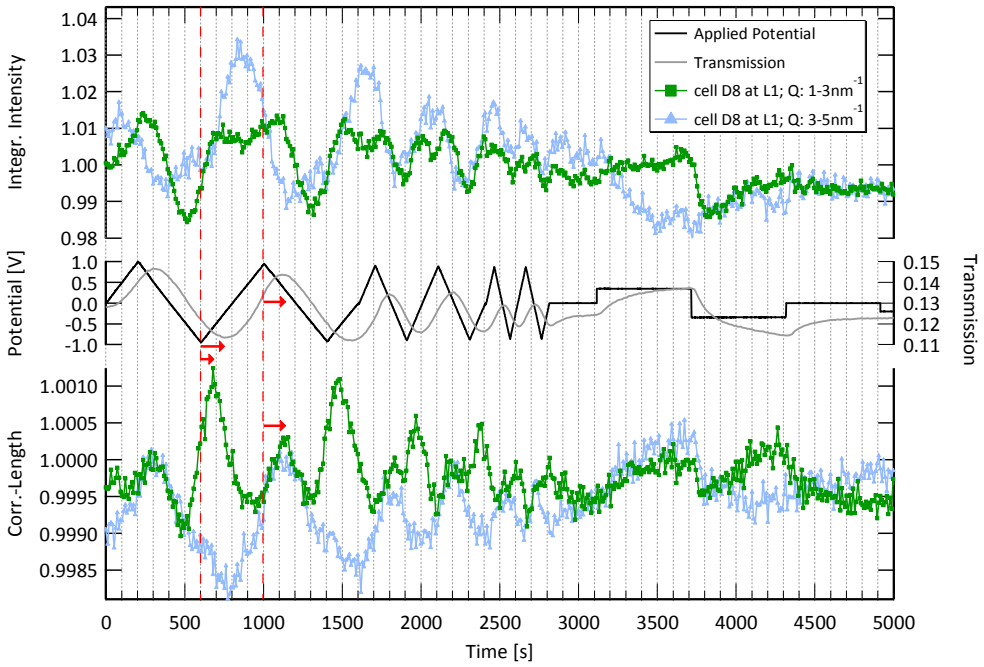

Fig. 32: Integral Intensity and Correlation length signals for a combined CV and CA measurement given for the Q-regimes Q-1 and Q-2 for the cell D8 (YP-80) at position L1. The integral SAXS signals are shifted arbitrarily in y-direction for better visualization. The scattering curves are time normalized, transmission and background corrected (section 3.3.1). The time-delay of both correlation length and transmission signal with respect to the applied potential is indicated with red arrows.

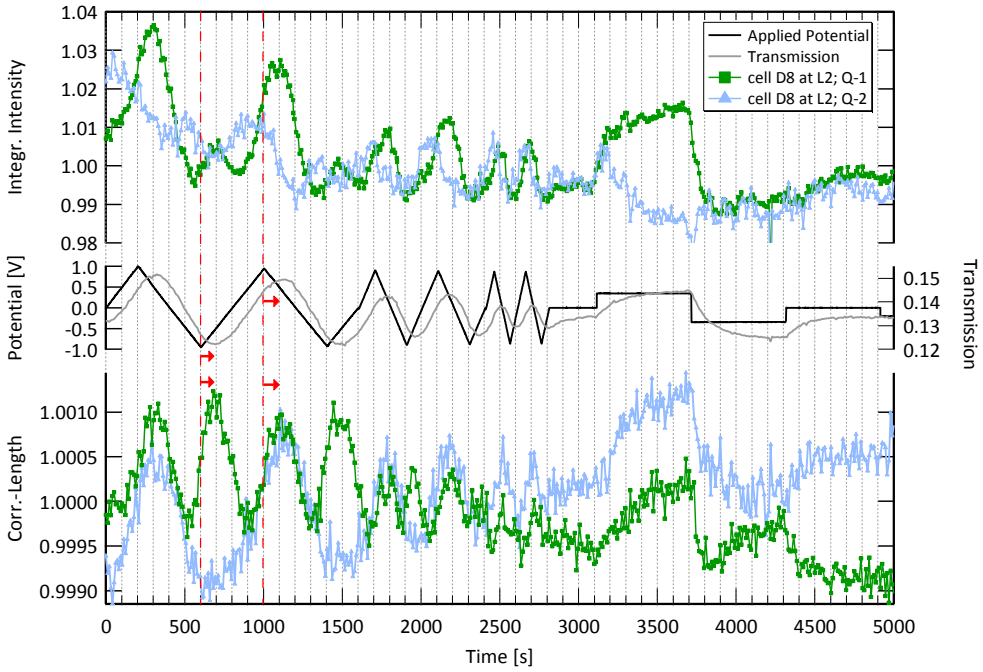

Fig. 33: cell D8 at position L2; description same as for Fig. 32

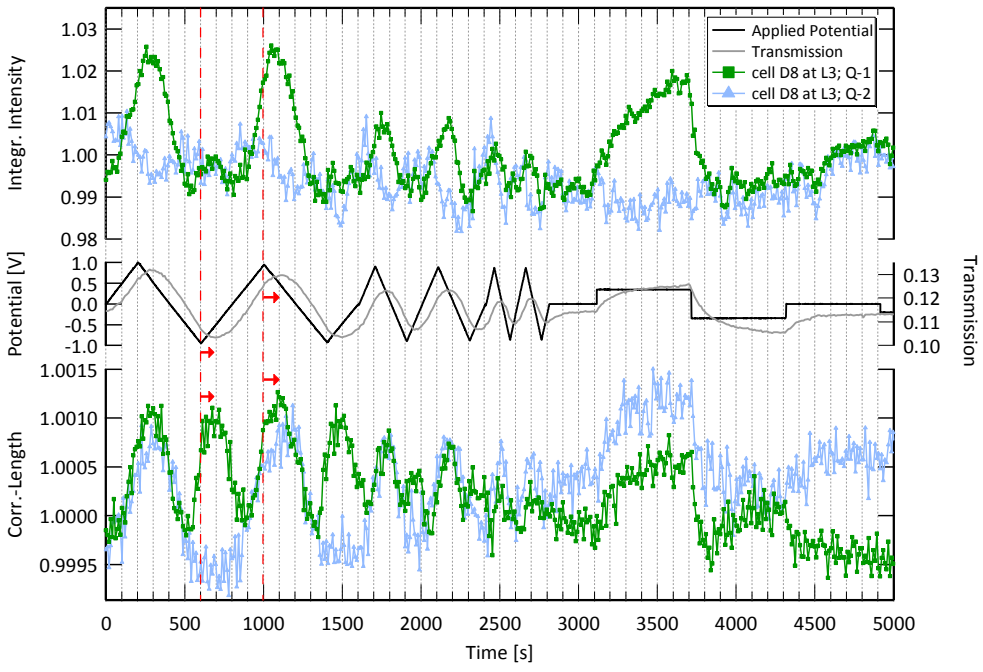

Fig. 34: cell D8 at position L3; description same as for Fig. 32

The D9 cell-design has in contrast to D8 a hole in the CC behind the WE at the area of the mentioned measurement-window. Thus, the distance for electrons or holes to move from the CC

to the center of the WE measurement-window is rather large. The In-situ measurement at the L1 position (Fig. 35) looks qualitatively similar to that of D8-L2 and D8-L3. Beside the time-delay of all measured signals compared to the potential could be expected. There is no difference between the time-delay of the scattering integral parameters and the transmission signal visible.

In Fig. 36 and 37 the measurement series for the D9 cell at position L2 and L3 is given. The signals look qualitatively similar to L1, but the time-delay for all signals seems to become smaller when approaching the outer region of the measurement-window. Especially when looking at the fast CV cycles (20mV/s) the large phase shift for the L1 position compared to L2 and in particular to L3 is visible. Since this local dependency effect seems to be strong compared to the transmission signal of the D8 cell, the carbon conductivity might play a critical role.

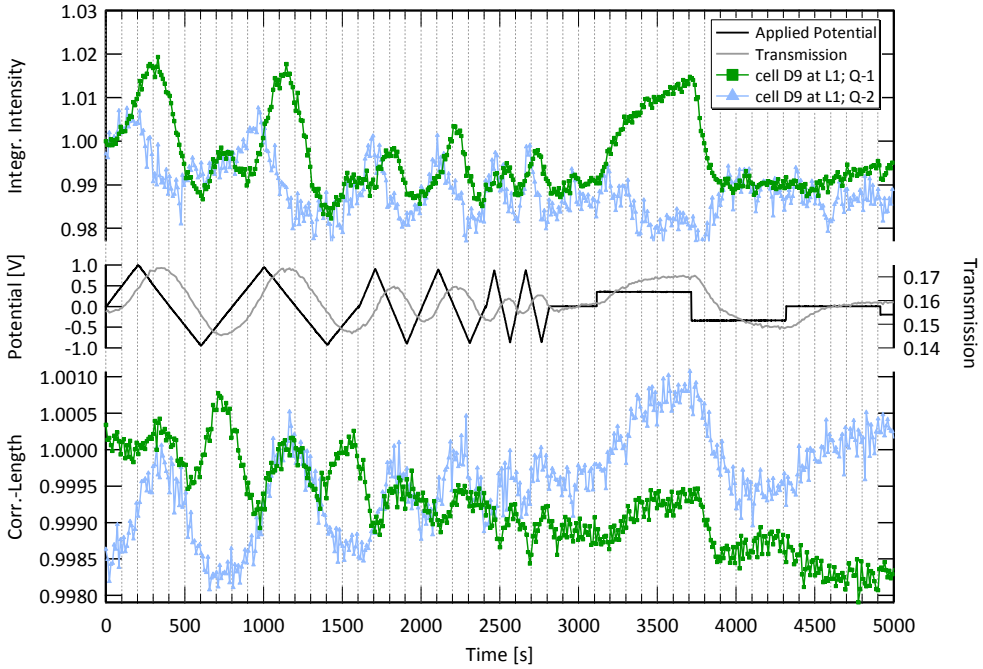

Fig. 35: cell D9 at position L1; description same as for Fig. 32

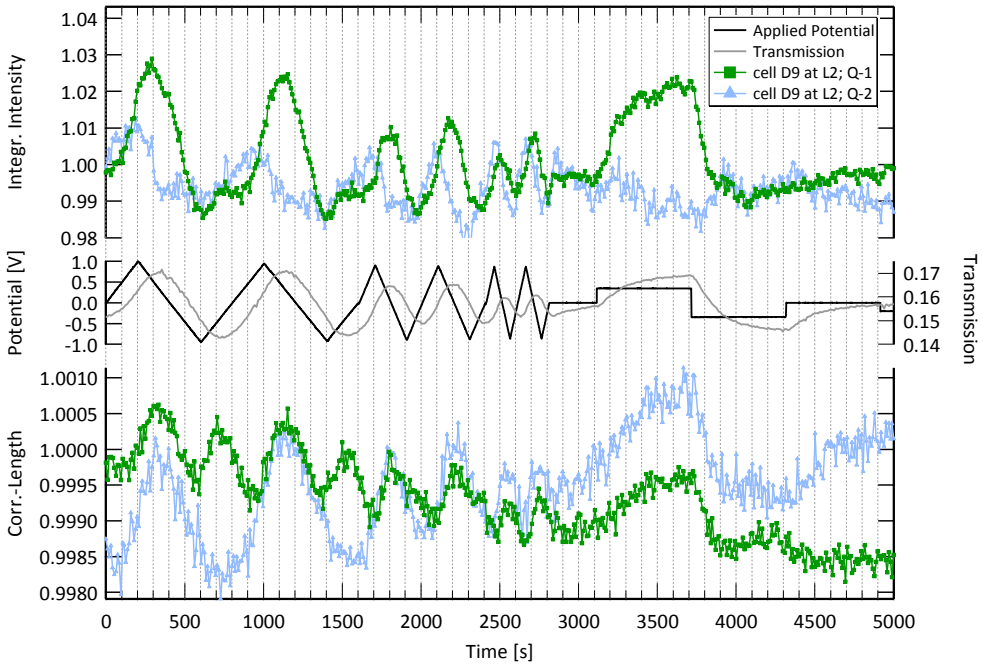

Fig. 36: cell D9 at position L2; description same as for Fig. 32

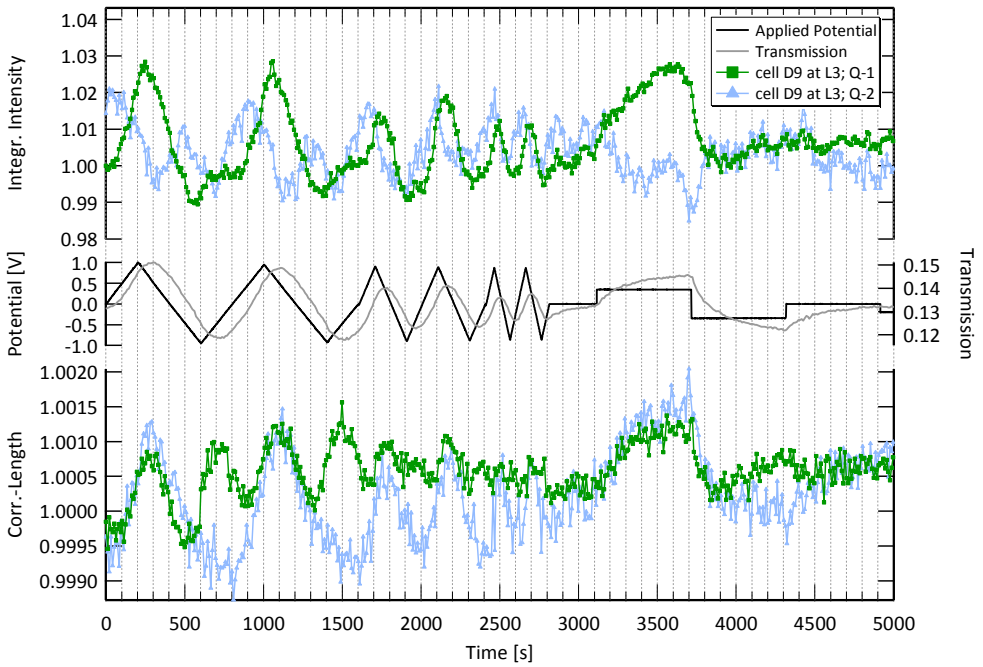

Fig. 37: cell D9 at position L3; description same as for Fig. 32

In an electrical double layer the Cs^+ ions may arrange in a rather densely packed configuration. The average distance of the hydrated ions would be in the range of the hydrated ion diameter

(3.29Å, see section 3.1.1). Thus a possible correlation peak due to dense packing of Cs^+ ions could be found around 10nm^{-1} ($2\pi/0.329nm$). A large amount of densely packed Cs^+ ions would influence also other region of the electrolyte structure factor since for a constant number of scattering ions the integrated intensity from zero to infinity remains constant. Therefore, in the neighboring regions of the correlation peak the electrolyte structure factor intensity has to decrease. The 0V WAXS scattering curve are compared for all D8 and D9 measurements in Fig. 38a. The D8 scattering curves look all very similar, although the slope of the intensity at smaller Q-values (around 8nm^{-1}) does not become constant, which was assumed from the bulk electrolyte measurements and required for the electrolyte structure factor subtraction. The D9 scattering signals look different to the D8 signals, although the materials are the same after subtraction and data correction. Especially for D9-L3 around the expected Q-value a peak is visible. A correlation peak is actually expected to appear on applying a potential and not at 0V. Furthermore there is no explanation why the correlation peak should occur at the L3 measurement and not at L2 and L1.

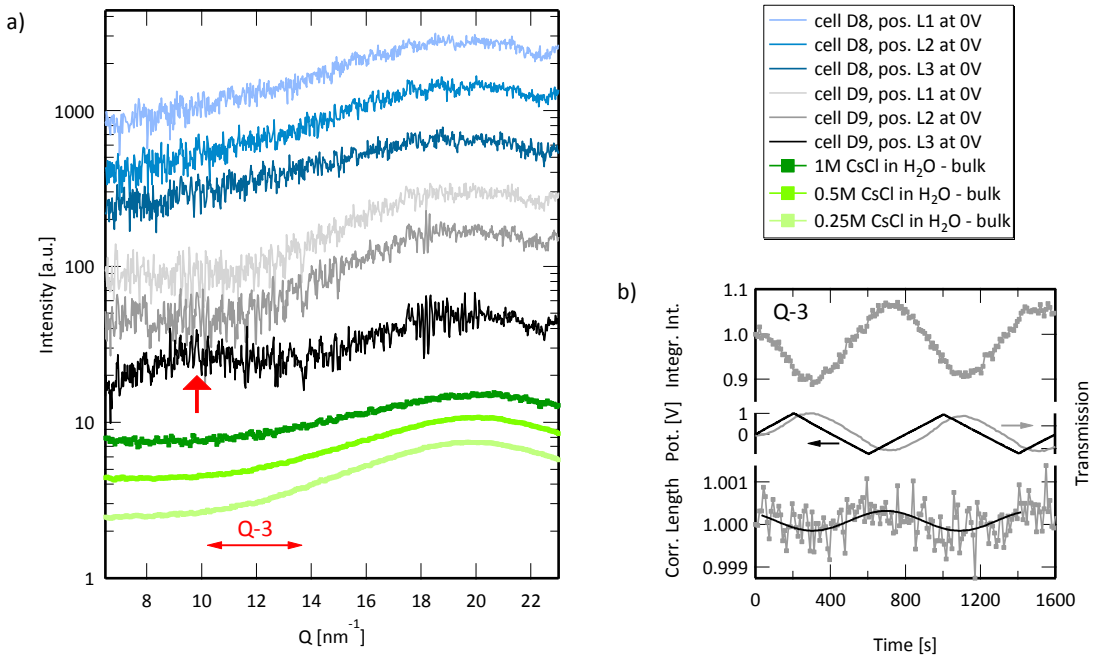

Fig. 38: In a) the scattering curves for the WAXS Q-regime (6.5-23nm^{-1}) of the D8 and the D9 cell at position L1, L2 and L3 is given. Furthermore the measurements of the bulk electrolyte at different ion concentrations are shown in green. The scattering curves are corrected and normalized according to chapter 3.3.1 and shifted arbitrarily in y-direction for better visualization. Remarkable is the peak around 10nm^{-1} for the D9 cell at position L3 (red arrow). Correlation length and integrated intensity indicated Q-3 region are given in b). If the correlation peak in a) would grow and shrink upon changing the potential the correlation length signal in b) is expected to have minima at negative and maxima at positive potentials. The opposite behavior was observed.

In Fig. 38b the integrated intensity and the correlation length signals for the D9-L3 measurement are indicated (valid for the Q-3 region indicated with red arrows in a)). If the correlation peak would grow upon increasing the Cs^+ concentration (negative applied potential), the correlation length should decrease. However the correlation length signal (Fig. 38b) exhibits a small maximum at negative potentials, most probably caused by the increased electrolyte structure factor contribution with respect to the constant correlation peak contribution. The origin of the peak occurring for the D9-L3 measurement remains unknown.

Calculating the integral parameters of the Q-regions in the WAXS regime (see Fig. 29), supports the correlation of the electrolyte structure factor with the Cs^+ concentration. The integrated intensity signals (as compared to those of the SAXS regime) make the contribution of the electrolyte structure factor to the SAXS signals better visible (Fig. 39). The change of the normalized integrated intensity signal caused by the changing Laue scattering intensity of the ions becomes smaller when going from Q-A to Q-C (according to the discussion of Fig. 28). The reason is that the water structure factor contribution (which is constant upon applying a potential) which becomes more dominant when approaching the Q-region around the peak ($20nm^{-1}$). At even larger Q-values the Cs^+ atomic formfactor causes a decay of the Cs^+ Laue Scattering intensity which is among other things responsible for the smaller amplitude at these Q-values.

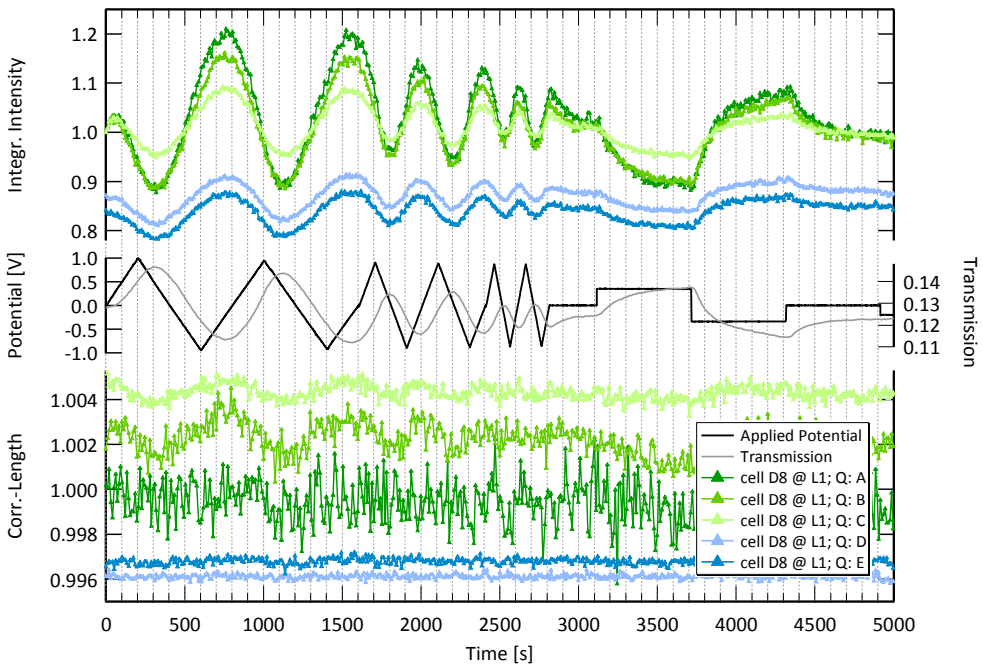

Fig. 39: Integral Intensity and Correlation length signals for a combined CV and CA measurement given for the various WAXS Q-regimes for the cell D8 (YP-80) at position L1. The integral WAXS signals are shifted arbitrary in y-direction for better visualization. The scattering curves are normalized and corrected according to section 3.3.1. No further data treatment was performed.

The correlation length changes are, similar like in the Q-2 region of the SAXS-regime, caused by the changing Laue Scattering intensity of the Cs^+ ions with respect to an intensity contribution being constant upon changing the potential. This latter contribution of the WAXS scattering intensity consists of water plus carbon structure factor. The intensity of carbon plus water structure factor increases with increasing Q, while the Cs^+ Laue scattering intensity is flat or slightly decreasing (atomic formfactor) with increasing Q. Thus the correlation length signal exhibits maxima at negative potentials and minima at positive potentials. In regions where the slope of the scattering curve of the two contributions ($C+H_2O$ structure factor vs. Cs^+ Laue scattering) is equal, the correlation length changes should vanish (Q-D and Q-E).

4.3 Advanced data treatment

In the following section the advanced data treatment is explained in detail. Explaining the data treatment exemplarily for specified measurements (D8-L1, CV & CA) seems to be advantageous.

4.3.1 Structure factor subtraction

The procedure to subtract the electrolyte structure factor contribution from the SAXS curves is based on several simplifying assumptions. Problems arising with these assumptions are discussed in the following chapters. The subtraction procedure requires an interpretation of the time-dependent SAXS curve changes discussed in section 4.1 and 4.2. Therefore one has to be careful with the further interpretation of the subtracted data. However, the features leading to the main conclusions discussed in section 4.4 are already visible in the non-subtracted data.

Interpretation of the SAXS time-dependency

In section 4.1 the scattering intensities of the samples at 0V conditions were shown. According to the electrolyte bulk measurements, the electrolyte scattering within the carbon structure causes an intensity contribution in the SAXS Q-regime, which might change upon applying a potential. The influence of the changing electrolyte structure factor on the SAXS scattering intensity seems to be large. Hence investigating the time dependent behavior of the integral parameters may lead to misinterpretations when only considering the SAXS two phase model.

As explained in section 4.1 the electrolyte structure factor contribution depends (similar to the transmission) on the overall Cs^+ concentration. Due to the Laue scattering of the Cs^+ ions the structure factor changes its height with respect to the actual SAXS curve, described by the two-phase model (carbon with electrolyte filled pores). The intensity is assumed to increase, when the Cs^+ concentration increases; thus the behavior is opposite with respect to the transmission signal. The electrolyte structure factor influences both integrated intensity $\tilde{I}$ and correlation length signal

L_c. At small angles (Q<5nm^{-1}) the two-phase-model is applicable and a contribution to $\tilde{I}(t)$ and $L_c(t)$, due to electron density contrast changes is expected.

The main changes of $\tilde{I}(t)$ and $L_c(t)$ are caused by the changing electrolyte structure factor and the changing electron density contrast according to the two-phase-model. Remarkable is the time-delay of $L_c(t)$ for 1 < Q < 3nm^{-1} (Q-1) in comparison to the time-delay of the transmission signal in the D8-L1 measurement (Fig. 32). At larger Q-values (3 < Q < 5nm^{-1}, Q-2) the time-delay corresponds to the transmission time-delay. Both transmission signal and electrolyte structure factor changes correlate to the overall ion concentration change within the irradiated volume. Hence the time-delay of both signals should be equal, which was observed for $L_c(t)$ calculated for Q-2. Furthermore the periodic behavior of $L_c(t)$ fits to the assumption of an increasing structure factor intensity at negative potentials and vice versa at positive potentials. The increasing intensity (constant in terms of Q) with respect to the two-phase-model contribution (Power law behavior in the Q-2 regime) means an increase of the "center of mass" leading to a decrease in the correlation length.

The changes of L_c at large Q-values (3 < Q < 5nm^{-1}) are mainly caused by the change of the structure factor intensity with respect to the scattering intensity of the wetted carbon pore structure (two-phase-model contribution). The change of the electron density contrast (which acts as constant pre-factor to the scattering intensity) only affects the integrated intensity signal. Only a change of the slope of the scattering curve can cause a change in $L_c(t)$.

The behavior of $\tilde{I}(t)$ looks compared to $L_c(t)$ even more complex at first sight. A subtraction of the changing electrolyte structure factor contribution seems to be the only possibility to further study the potential driven changes of the actual SAXS curve. The constant electrolyte structure factor below 9nm^{-1}, as measured for the bulk electrolyte (Fig. 28), is a simplyfying assumption. A dense packing of Cs^+ ions in a double layer or within the micropores could cause a correlation (intensity-) peak around Q ≈ 9nm^{-1}. An intensity increase around this position at the same time gives rise to an intensity decrease in the neighbouring Q-regions. This fact makes the evaluation of the changing structure factor intensity problematic. However, since the electrolyte structure factor contribution is clearly visible on the correlation length signals a "trial and error method", with the verification of the resulting signal after subtraction seems to be the best strategy.

In the correlation length signal for the Q-region from 3-5nm^{-1} the "changing electrolyte contribution" prevails with respect to all other contributions. Thus this Q-regime seems to be best for the verification of the right structure factor intensity. Fitting a model correlation length signal (consisting of a flat electrolyte intensity + scattering signal of the carbon structure filled with electrolyte) to the measured one, enables the evaluation of the potential dependent Cs^+ electrolyte intensity in the SAXS region.

Structure factor evaluation (general)

The code for the electrolyte structure factor evaluation within the SAXS Q-region was written in the data analysis software IGOR Pro. In the following the procedure is described qualitatively.

1. Evaluate the normalized $\tilde{I}(t)$ of the WAXS Q-region from 6 to 9nm^{-1} ("relative amplitude" of the electrolyte structure factor contribution)

In the WAXS Q-regime from 6 to 9nm^{-1} $\tilde{I}(t)$ is assumed to represent the changes of the electrolyte structure factor only. In this Q-regime the "two-phase-model contribution" is nearly zero (see Fig. 26). The carbon structure factor is similar to the water contribution constant upon applying a potential. Furthermore the carbon structure factor is assumed to be constant within the SAXS Q-regime. Since the WAXS and the SAXS scattering intensities were recorded on different detectors only the relative change can be utilized from the Q-regime between 6 to 9nm^{-1}. The assumption of a constant electrolyte structure factor below 9nm^{-1} is not perfectly valid (compare Fig. 28 and 38). Nevertheless, $\tilde{I}(t)$ is normalized by its first value ($\tilde{I}(t=0)$ and further used to build up a model correlation length signal for the SAXS region from 3.5-5nm^{-1}.

2. Use the corresponding relative amplitude value to build up a model scattering curve in the SAXS Q-region from 3.5-5nm^{-1}. Therefore the fit parameter is needed, representing a scaling factor for the relative amplitude

As indicated in Fig. 40, the scattering curves consist of a flat electrolyte structure factor contribution and the contribution of the SAXS scattering intensity originating from the wetted pore structure (two-phase model: matrix + pores). Upon applying periodic potential signals (CV) both contributions will change, indicated in Fig. 40 on the right. The changing ion concentration within the pores changes the electron density contrast and thus the prefactor $(\Delta\rho)^2$ of the two-phase-model contribution. In order to calculate a model scattering intensity for each frame of the in-situ experiment the normalized electrolyte intensity value times an unknown fitparameter (dashed red curve in Fig. 40 on the left) are added to the corresponding two-phase-model contribution (blue curve in Fig. 40 on the left). The evaluation of the two-phase-model contribution is explained in section 4.3.3.

3. Calculate a model correlation length signal from the model scattering curves

As described above the model-scattering curves are evaluated for all frames recorded during the in-situ experiment. For each model scattering curve the correlation length is calculated, leading to the time-dependent correlation length signal $L_c(t)$.

4. Fit the model correlation length signal to the measured correlation length signal and evaluate the best fitparameter.

The model $L_c(t)$ is now fitted to the $L_c(t)$ of the measured SAXS intensity of the Q-regime from 3.5-5nm^{-1}. In Fig. 41 $L_c(t)$ of the measured scattering curves and a set of model $L_c(t)$ with different fit paramters are indicated. The fit error (residuum) corresponds to the sum of the absolute values of the difference between model- and measured correlation length values. The fit parameter leading to the lowest fit error is used to calculate the electrolyte structure factor intensity. Therefore the normalized structure factor intensity, obtained from $\tilde{I}(t)$ of the WAXS Q-region from 6-9nm^{-1}, has to be multiplied by the evaluated fit parameter.

5. Subtract the electrolyte structure factor contribution from the SAXS curves.

Each value of the obtained electrolyte structure factor intensity is now subtracted from the corresponding SAXS curve. To proof the quality of the fit $\tilde{I}(t)$ and $L_c(t)$ of the subtracted SAXS curves are evaluated and verified.

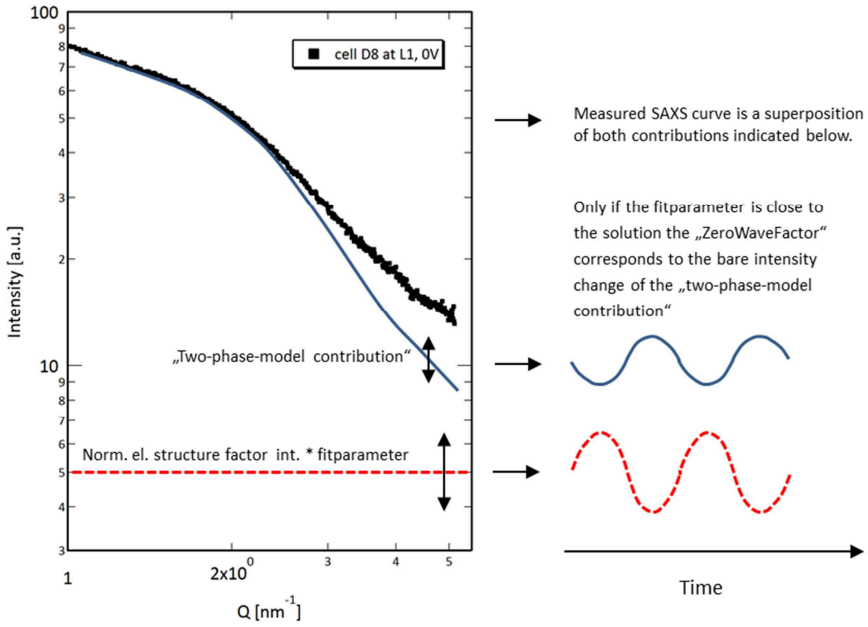

Fig. 40: The scattering intensity (SAXS) consists of the contribution of the porous carbon structure ("Two-phase model" contribution in blue) and the intensity of the electrolyte structure factor (in red, dashed). Both contributions behave opposite upon changing the ion concentrations. The relative change of the electrolyte structure factor is obtained from the WAXS signal. This relative amplitude is used as input for the actual fitting procedure where the absolute starting "height" of the electrolyte contribution is evaluated. Hence, the fit parameter corresponds to a scaling factor of the normalized electrolyte structure factor intensity which is obtained from the WAXS signal (6-9nm^{-1}).

Structure factor evaluation (detailed)

As mentioned the model scattering curve is produced by adding the normalized electrolyte structure factor intensity times the fitparameter to the two-phase-model contribution. The two-phase-model contribution (blue curve in Fig. 40 on the left) is in turn calculated by subtracting the

normalized electrolyte structure factor intensity times the fitparameter from the first (at t=0) measured SAXS curve(black curve in Fig. 40 on the left).

The time-dependent changes of the two-phase-model contribution are considered by multiplying the so-called “ZeroFrameFactor” to the two-phase-model contribution. The “ZeroFrameFactor” is evaluated by calculating $\tilde{I}(t)$of all measured SAXS curves, which are in prior to that subtracted by the normalized structure factor intensity times the fitparameter. Furthermore $\tilde{I}(t)$ is normalized by its first value $\tilde{I}(t=0)$.

For each model scattering curve the model correlation length is calculated. Doing this procedure for all frames of the in-situ experiment results in the model-correlation length signal as mentioned before. Below a hypothetical, for-loop for calculating the model correlation length, is shown.

$$for\ (i = 0; i < \#frames; i = i + 1)$$

$$ZeroFrameFactor[i] = \frac{integIntfunction(measSAXScurve[i] - fitparameter * normElectrolyteSFint[i])}{integIntfunction(measSAXScurve[0] - fitparameter * normElectrolyteSFint[i])}$$

$$ModelSAXScurve[i] = (measSAXScurve[0] - normElectrolyteSFint[i] * fitparameter) * ZeroFrameFactor[i] + normElectrolyteSFint[i] * fitparameter$$

$$ModelCorrLength[i] = corrLengthfunction(ModelFrame[i])$$

$$endfor$$

This model correlation length is caculated for a specified set of fit parameters and compared with the measured correlation length (as shown in Fig. 41). The residuum is calculated for all fit parameter values. The fit parameter leading to the minimum fit error is used for calculating the electrolyte structure factor intensity contribution.

Since first the structure factor contribution is subtracted from the measured scattering curve (to get the two-phase-model contribution) and subsequently added again (to get the model-scattering curve), one could wonder how the best fitting solution is found. If the fit parameter is far away from the best fitting solution the “ZeroFrameFactor” deviates significantly from the “true” behavior, which in turn influences the model-scattering intensity. The complete fitting procedure, written as Igor Pro code, is given in Appendix A.

In Fig. 41 the model correlation length signals for a set of fit parameters and the correlation length from the measured scattering curves are given. A large deviation of the fit parameter from the best fit-value still produces correlation length signals very similar to the measured one. The stability of the fit is therefore rather low, which makes an exact evaluation of the right fit parameters difficult.

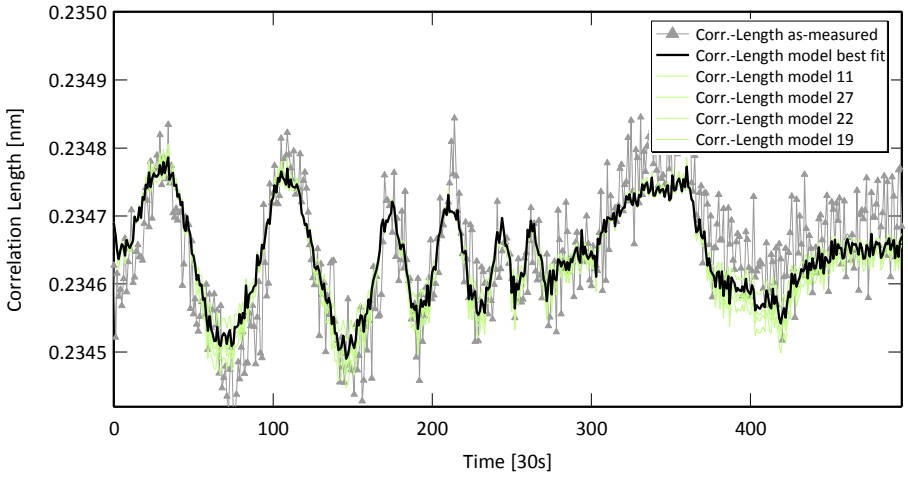

Fig. 41: The model correlation length signals for a set of possible fitting results are shown in green and black. All fit parameters give signals with only small deviations from the measured signal. The fitting procedure is therefore rather unstable.

Results after subtraction

A detailed look on the results after subtracting the structure factor contribution gives immediate information on the quality of the fitting result. The constant correlation length signal for Q-2 is a good indicator for the quality of the subtraction procedure. Since the electrolyte structure factor change was assumed to be the only reason for the correlation length change in the Q-regime from 3.5-5nm^{-1} after successfull subtraction $L_c(t)$ in this Q-regime should become constant. Any additional contribution causing L_c changes within Q-2 could either be gathered by the fit (and wrongly subtracted) or lead to problems with finding the right fit parameter. The latter is more likely to happen.

The integral parameter signals of the subtracted D8-L1 data are given in Fig. 44. Both $\tilde{I}(t)$ and $L_c(t)$ are now much easier to interpret. All the changes can be ascribed to changes of the carbon pore structure filled with electrolyte. In particular the integrated intensity signal shows features which were not visible before. The time-dependecy of the extremal points in the curve fit to the correlation length signal. Obviously the ion transport processes tracked with scattering exhibit a different time constant than the processes tracked with transmission.

Although the procedure above is based on several simplifying assumptions all conclusions that are drawn in the following could have been made on the non-subtracted data. The occurrence of the most important features in the non-subtracted data was verified retrospectively (after the interpretation of the subtracted data).

4.3.2 Ion concentration calculation

In order to calculate the absolute ion concentration changes within the pores of the carbon electrode both transmission and electrical current signals are utilized. As explained in section 2.3 the X-ray beam intensity decays exponentially within the penetrated material and can be split into the contributions of its single components (Fig. 42).

$$\tau = \frac{I(d)}{I_0} = e^{-\mu_{cell} d_{cell}} = e^{-\mu_{Cs} d_{Cs}} * e^{-\mu_{Cl} d_{Cl}} * e^{-\mu_{H2O} d_{H2O}} * e^{-\mu_{carbon} d_{carbon}} \quad (42)$$

Only the ion concentration is assumed to change significantly (red arrow in Fig. 42) upon applying a potential, the carbon and water contribution within the pore is assumed to be constant. Although in some literature the exchange of water molecules in larger pores (>1.3nm, according to [7]) is reported, the contribution should be negligible, since the absorption coefficient of water is relatively low. Also an expansion of the carbon structure in the order of 10^{-3} does not lead to a significant transmission change.

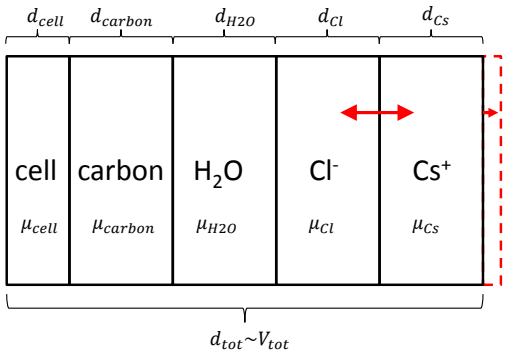

Fig. 42: The layer model of the in-situ cell indicating all contributions to absorption. All absorption coefficients are assumed to be constant. Only the thickness d_{cl} and d_{cs} will change upon changing the ion concentrations. Furthermore the sum of d_{cl} and d_{cs} and consequently the total thickness d_{tot} may change as well.

Since the ion concentration is changing during a charging/discharging process, the product μd will change as well. Thus the logarithm of the transmission as a function of time (or the applied potential) gives the following expression.

$$ln(\tau(t)) = -X_{Cs}(t)(\mu d)_{Cs,0} - X_{Cl}(t)(\mu d)_{Cl,0} + constant \quad (44)$$

$X_{Cs}(t)$ and $X_{Cl}(t)$ are factors which correspond to the relative change of the ion concentration $c(t)$ as a function of time (e.g. $X_{Cs} = c_{Cs}(t)/c_{Cs,0}$ where $c_{Cs,0}$ is the Cs^+ starting/initial concentration at 0V). All other parameters are measurable. The ion concentrations are given in number of elementary charges per cm^3. The measurable constant in eqn. (43) is defined as follows.

$$constant = -\mu_{H2O} d_{H2O} - \mu_{carbon} d_{carbon} - \mu_{cell} d_{cell} \quad (44)$$

The term $\mu_{cell}d_{cell}$ corresponds to the logarithm of the transmission of the empty cell, including 2x Scotch© tape (or Kapton© tape) and any air absorption. The contribution of water $\mu_{H2O}d_{H2O}$ is evaluated by measuring once the dry carbon and once the carbon wetted with water. The water is assumed to wet the carbon pores to the same extend as the electrolyte does. Subtracting the logarithm of the dry carbon transmission from the logarithm of the wetted carbon transmission gives the water contribution to transmission. Furthermore the wetted pore volume can be estimated (using the thickness d_{H2O} which is proportional to the pore volume), since the theoretical absorption coefficient of water μ_{H2O} is known. Comparing these values with another transmission measurement of the carbon wetted with electrolyte enables the calculation of the ion concentration within the pores at 0V conditions. Therefore a sample design similar to the in-situ cell explained in section 3.3 but without the need of electric contacts have to be used. In this way an infinite reservoir of electrolyte surrounds the measurement-window, allowing the diffusion of ions into the carbon pore structure in the case the equilibrium concentration differs within the pores. The initial ion concentration within the pores is needed as a starting point for the calculation of the absolute ion concentration. The concentration of negative and positive ions entering the pores at 0V is assumed to be equal ($c_{Cs,0} = c_{Cl,0}$).

The cation/anion concentration changes, tracked by the transmission signal, are assumed to correspond to the number of electrosorbed charges within the micropores. This is certainly a weak point in the ion concentration calculation. However, at the end of section 5.2.3 strong indications for the validity of this assumption are provided. Additionally it is assumed that the electrosorbed charge $N(t)$ (in units: number of elementary charges) corresponds to the difference of the number of cations and anions within the pores. $N(t)$ is calculated by integrating the measured current signal over time. Since we deal with concentrations these quantities are normalized by the pore volume V_{pore} . Hence, the relative change of the Cl^- concentration can be expressed as follows:

$$X_{Cl}(t) = \frac{N(t)}{C_{Cs,0}V_{pore}} \pm X_{Cs}(t) \qquad (45)$$

It depends on the sign convention of $N(t)$ if we have a plus or minus in the equation. Putting eqn. (45) in eqn. (43) leads to an equation with only one unknown variable, which is the relative change of the Cs^+ concentration X_{Cs}.

$$ln(\tau(t)) = -X_{Cs}(t) * (\mu d)_{Cs,0} - \left(\frac{N(t)}{V_{pore}} \pm X_{Cs}(t)\right) * (\mu d)_{Cl,0} + constant \qquad (46)$$

Due to the diffusive ion transport a local dependency of the transmission signal on the measurement spot on the WE may occur. Thus only the equilibrium concentrations are used for the ion concentration calculations. To minimize the error first the initial concentration at 0V is

measured and afterwards the ion concentration change calculated, based on this starting value. With the initial concentration the values $d_{Cs,0}$ and $d_{Cl,0}$ can be calculated. The ion size of Cl^- and Cs^+ is similar, thus $d_{Cs,0}$ and $d_{Cl,0}$ is assumed to be equal. The value d_{H2O} from the measurement mentioned above corresponds to the total pore volume that is wetted by the electrolyte. Knowing the initial concentration X_{in} gives $d_{Cs,0} = d_{Cl,0} = X_{in} * d_{H2O}$. As a result, knowing the starting concentration at 0V and calculating the relative change of this concentration using eqn. (46), directly gives the absolute ion concentration change for a specified potential step for Cs^+. Subsequently eqn. (45) can be used to calculate the change for Cl^-. In Fig. 43a the charge, which is gained from an integration of the current signal over time and the transmission signal for 4 CA potential steps, is shown. In order to minimize the error the concentration change is not calculated by rearranging eqn. (46), but evaluated by using an exponential fit for every potential step of interest. In Fig. 43b the data points of the negative logarithm of the measured transmission for a discharging process of a potential step from -0.5 to 0V (e.g. in Fig. 43a around 5500s) is shown.

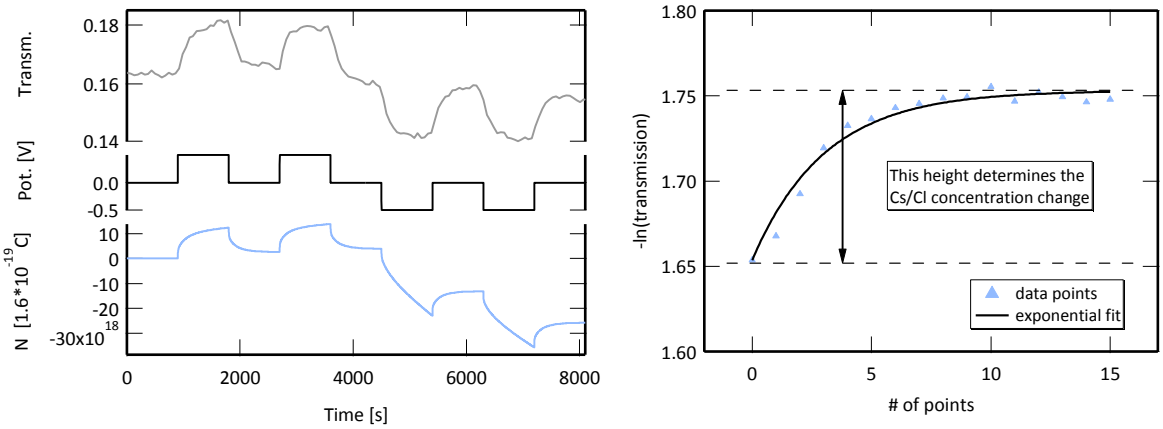

Fig. 43: In a) the transmission signal as well as the calculated charge (out of current signal) for 4 potential steps are given. Due to significant faradaic reactions in particular at negative applied potentials only the discharge currents are used for the ion concentration evaluation. In b) the exponential fit to the negative logarithm of the transmission signal is indicated. The signal belongs to a potential step from -0.5V to 0V (e.g. around 6000s in a). The height indicated with the black arrow determines the Cs^+/Cl^- concentration change.

In order to avoid contributions of leakage currents, which affect the charge N, only discharge processes are investigated. The large change of the calculated charge for negative potential steps (0 → -0.5V; see Fig. 43a) can be attributed to the onset of a water degradation reaction [1]. Thus the applied potential is zero and only the rearrangement of ions can cause a current. The fit function looks as follows.

$$const. + (\mu d)_{Cs,0}\ \frac{par1}{C_{Cs,0}}\left(1 - e^{-\frac{t}{par2}}\right) + (\mu d)_{Cl,0}\left(\frac{par1}{C_{Cs,0}} + \frac{\Delta N}{C_{Cs,0} V_{por}}\right)\left(1 - e^{-\frac{t}{par2}}\right) \quad (47)$$

V_{por} is the wetted pore volume, ΔN the difference of charge between the ±0.5V and the 0V equilibrium position and $c_{Cs,0}$ the initial ion concentration at 0V. The two exponential terms correspond to the opposed increase/decrease of the Cs^+/Cl^- concentration. Basically this formula is similar to eqn. (46) with the additional property of an exponential increase/decrease of the concentration. The first fit parameter *par1* represents the Cs^+ concentration change when going from ±0.5V to 0V. The second fit parameter *par2* is the time constant of the exponential discharging process.

By calculating random and independent, gauss distributed values of the input parameters the fitting results scatter slightly in the end. Performing the evaluation procedure about 100 times (for-loop) gives a good estimation of the experimental error of the entire calculation. The error was found to be surprisingly low, which is at first counter intuitive since a rather exact concentration evaluation is possible for both ion species, although the absorption coefficient of Cl^- is more than 10 times lower than the Cs^+ one. In fact first the Cs^+ concentration is evaluated by the fitting procedure indicated in Fig. 43b. The second exponential term, which corresponds to the Cl^- contribution to the transmission signal, is at least ten times smaller. Thus the result of the fitting procedure is not governed by the Cl^- contribution. After the Cs^+ concentration is evaluated, using eqn. (45) and ΔN instead of $N(t)$ the Cl^- can be calculated. As a consequent the error of the Cl^- concentration is not higher than the Cs^+ one. The complete Igor Pro code of this procedure is given in appendix B.

In Table 6 all attenuation coefficients and evaluated initial layer thicknesses, needed for the ion concentration evaluation, are given. The attenuation coefficients of Cl^- and Cs^+ are estimated by using the linear mass attenuation coefficients (μ/ρ) for Cs and Cl respectively. The density of both ions was evaluated by measuring the volume increase in water upon adding a defined mass of CsCl salt. Hence, the attenuation coefficients were calculated using $(\mu/\rho) = (\mu/\rho) * \rho$.

Table 6: Attenuation coefficients and initial layer thicknesses (at 0V) and measured transmission values needed for the ion concentration calculation.

Cell + carbon		H_2O	Cl^-	Cs^+
$\tau_{meas} = 0.91$	**μ [cm-1]**	10.35	189.9	2178.1
	$d_{initial}$ [cm]	0.034	0.000583	0.000583

4.4 Subtracted SAXS data

In the following the results of the position dependent measurements of cell D8 and D9 (both YP-80), after subtraction of the electrolyte structure factor (as described in chapter 4.3.1) are shown. As discussed above the subtraction procedure does not work perfectly for all measurements. However, the conclusions and interpretations drawn from the subtracted data could have been made already from the non-subtracted data. Nevertheless, this subtraction enables a clearer view on all processes contributing to the complex integral SAXS signals.

First the behavior for the D8 cell at position L1 is discussed (Fig. 44). According to the subtraction procedure, the correlation length signal for the Q-2 region should become constant, since it was assumed that the entire correlation length changes in Q-2 were caused by the change of the electrolyte structure factor contribution (see e.g. Fig. 32). The correlation length signal in Q-2 represents thus a quality criterion of the subtraction procedure. In the case of D8-L1 the subtraction indeed worked very well. Apart from a slight drift the signal is constant within the statistical error. The integrated intensity signal for Q-2 corresponds to the behavior expected from the two-phase model. The signal correlates with the inverse of the Cs^+ concentration within the micro- and mesopores. In the case of Q-1 an additional small intensity peak comes up at negative potentials. At the same position a large peak in the correlation length signal is present. The time-delay behavior remained similar with respect to the non-subtracted signals. The scattering integral parameters have a clearly smaller time-delay with respect to the potential minmum as compared to the transmission signal.

This remarkable time-delay behavior at the L1 position is not visible for the L2 and L3 position (Fig. 45 and 46), as already observed for the non-subtracted data. Beside these kinetic effects the qualitative behavior is similar for all three positions. The main change in the integrated intensity signal is caused by the change in the electron density contrast. Other features like the peaks in the correlation length signal or the deviation of the Q-1 integrated intensity signal (with respect to the integrated intensity signal of Q-2) have to be studied in more detail.

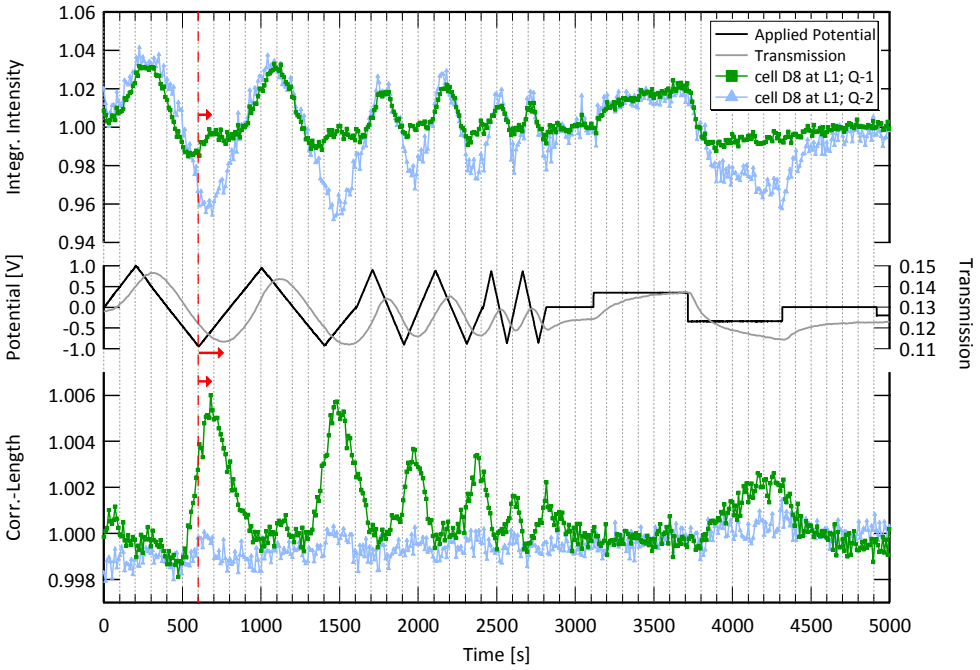

Fig. 44: Integrated intensity and correlation length signals for a combined CV and CA measurement given for the Q-regimes Q-1 and Q-2 for the measurement at position L1 (cell D8). The scattering curves are normalized and corrected according to section 3.3.1. Additionally the electrolyte structure factor contribution is subtracted. In contrast to the non-subtracted signals (chapter 4.2) the integral SAXS signals are easier to interpret. As indicated with the red arrows the remarkable time-delay behavior between the different signals is maintained with respect to the non-subtracted signals (as shown in chapter 4.2).

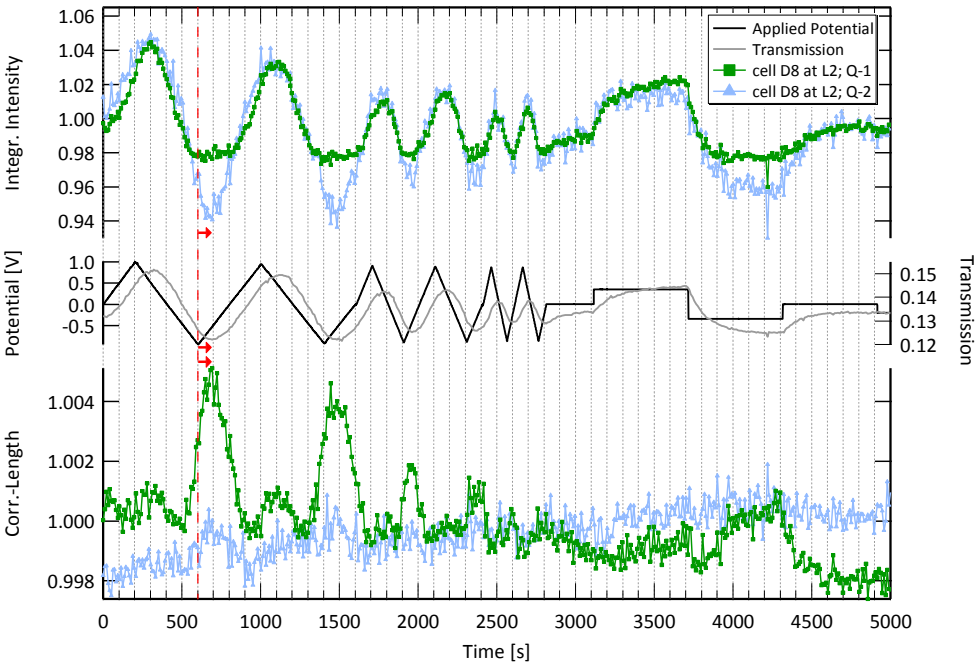

Fig. 45: cell D8 at position L2; description same as for Fig. 44

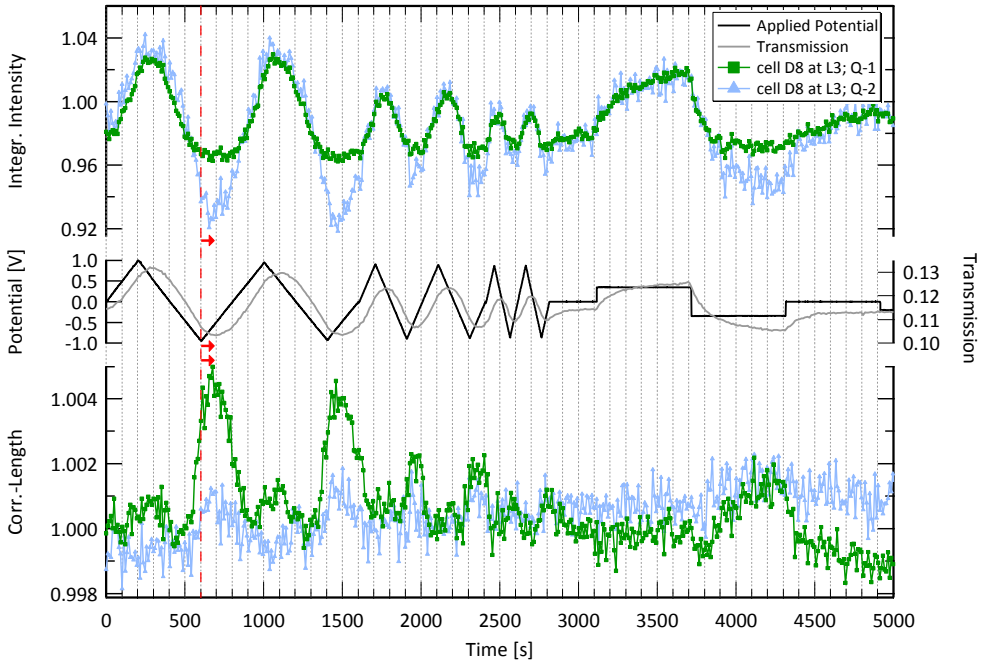

Fig. 46: cell D8 at position L3; description same as for Fig. 44

Beside the difference in the kinetic behavior, (as mentioned in chapter 4.2), the signals of D9 look similar to those of D8 (Fig. 47, 48, 49). Remarkable is however the bad quality of the subtraction procedure indicated by the peaks in the correlation length signal of Q-2. The WAXS scattering curves at 0V (see Fig. 38) already indicate strong differences between the D8 and the D9 measurements. The simplifying assumptions of a flat electrolyte structure factor contribution going up and down is probably not applicable to the D9 cell. The formation of a correlation peak of dense packed Cs^+ ions may change the situation, as discussed for Fig. 38. Still, there is no explanation available why the D9 measurements are that different compared to D8.

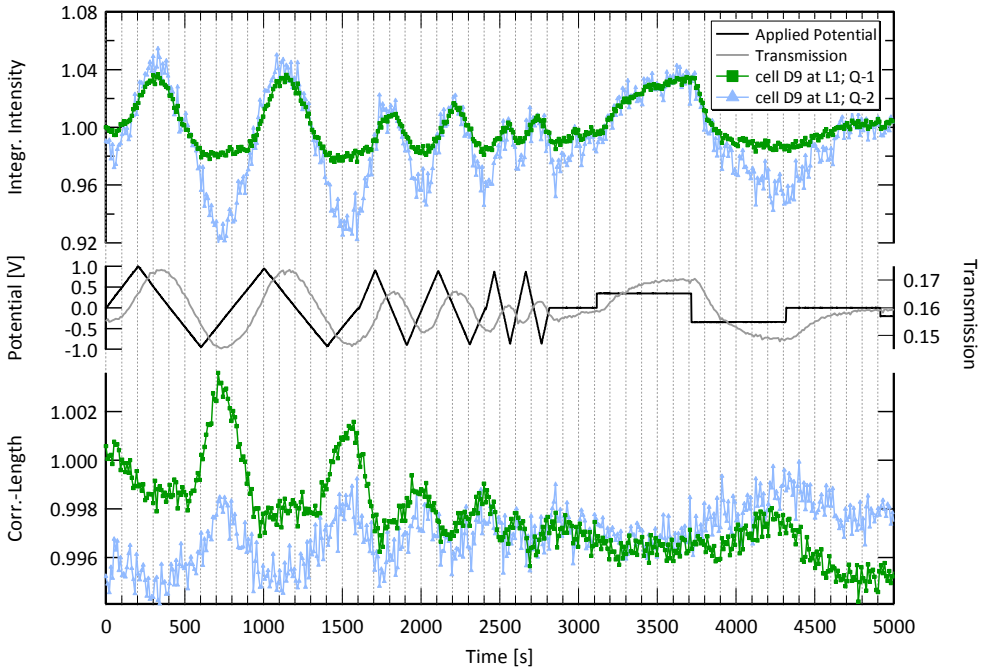

Fig. 47: Integrated intensity and correlation length signals for a combined CV and CA measurement given for the Q-regimes Q-1 and Q-2 for the measurement at position L1 (cell D9). The scattering curves are normalized and corrected according to section 3.3.1. Additionally the electrolyte structure factor contribution is subtracted. In contrast to the non-subtracted signals (chapter 4.2) the integral SAXS signals are easier to interpret. Remarkable is the bad quality of the electrolyte structure factor subtraction, observable on the features in the correlation length signal for Q-2.

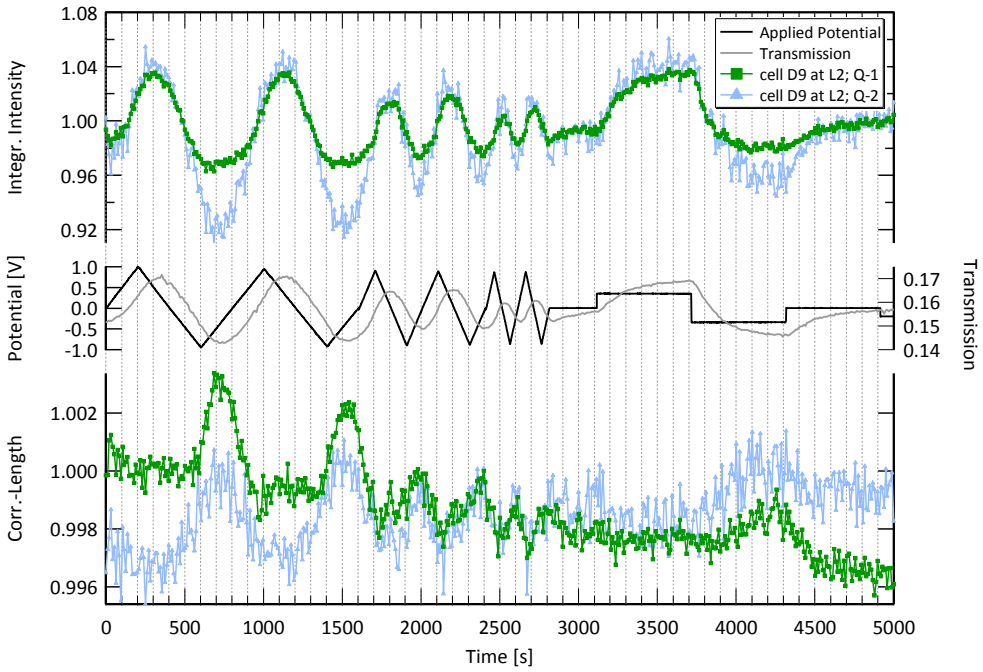

Fig. 48: cell D9 at position L2; description same as for Fig. 47

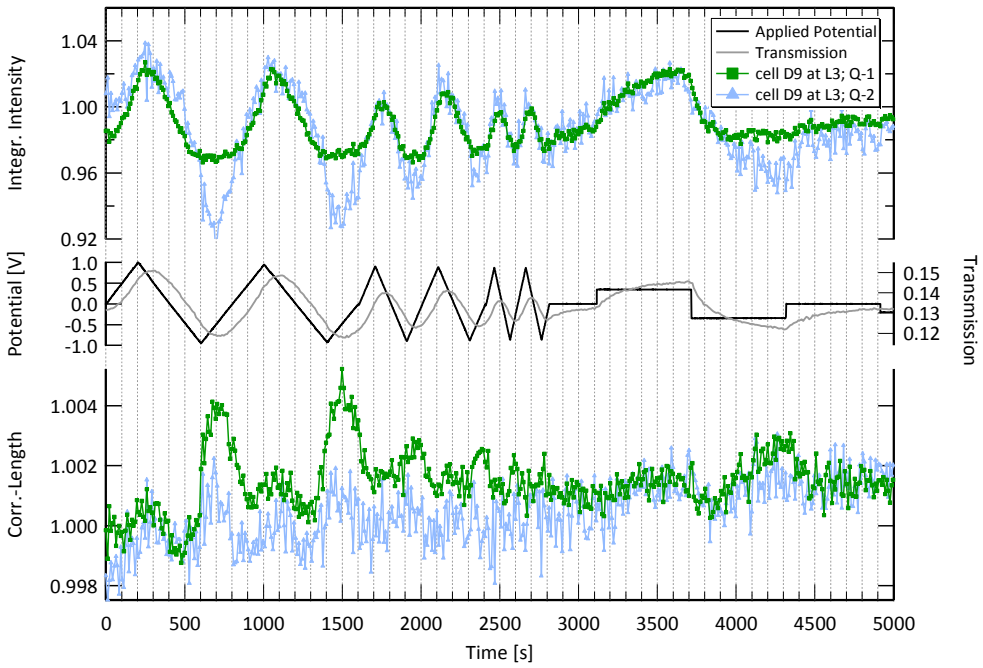

Fig. 49: cell D9 at position L3; description same as for Fig. 47

4.4.1 Ion kinetics

The chronologically ordered plots of the data presented above provide only a limited understanding of the physical processes behind the ion transport and rearrangement. Thus a more detailed analysis is necessary. In many cases only the relative change of the signals is of interest. For a better visualization the curves might be shifted in y-direction. In the following the subtracted data shown in section 4.4 are analyzed in detail. All scattering data was time normalized, transmission and background corrected according to section 3.3.1 before subtracting the electrolyte structure factor contribution. The main conclusions are drawn on effects basically traceable in the non-subtracted data shown in section 5.2.1.

For the D8 cell at position L1 a time-delay difference between scattering and transmission signals has been observed. The absolute time delay values are extracted by fitting a polynomial to the maximum or minimum region of the signal of interest. Subsequently the difference between the maximum/minimum positions of the polynomial compared to the maximum/minimum of the potential signal is calculated. In general the time-delay can be attributed to the diffusive nature of the ion transport. Hence also a dependence on the frequency of the CV-cycles is expected. For both scattering and transmission signals the normalized time-delay was found to increase with faster cycling rate (Fig. 50). The time delays are normalized by the time of the corresponding

period, thus representing a phase shift. When cycling faster the ions are not able to follow the signal anymore, which causes the larger phase shift.

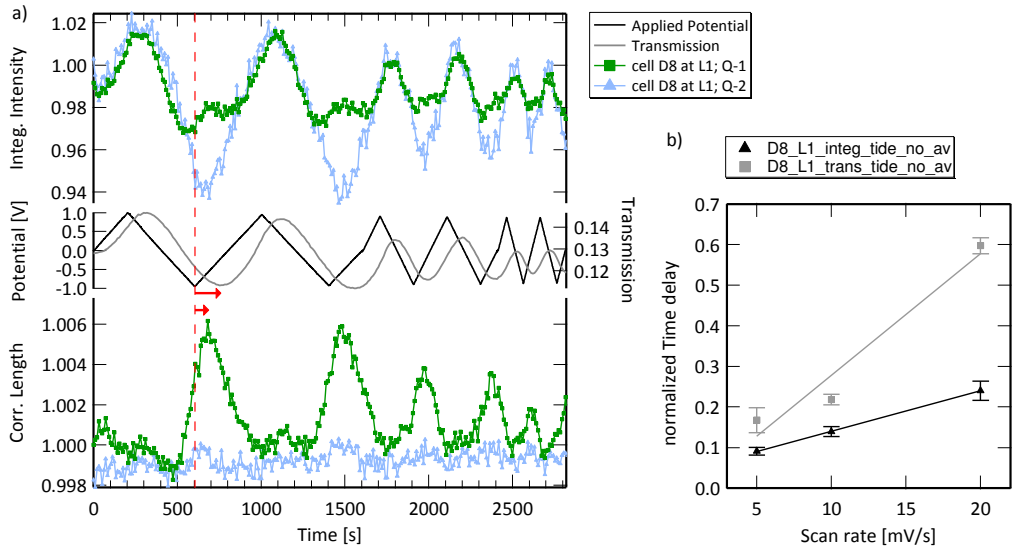

Fig. 50: Integrated intensity and correlation length of Q-regimes Q-1 and Q-2 for D8 at the WE position L1 is given in a). The transmission signal exhibits a different time delay with respect to the potential as compared to the scattering signals (indicated with red arrows). In b) the frequency dependency for the time delays for both transmission and scattering signal is given.

Due to the diffusive nature of the ion transport, a local dependency of the ion kinetics seems possible. In the case that a macroscopic ion transport takes place, the special cell design with its large “measurement window” (diameter of 12mm) forces the ions to move different distances from the counter electrode to the corresponding measurement spot. The distance for ions to move from the CE to the L1 spot is largest. As explained earlier the transmission signal is sensitive to any concentration change within the irradiated spot and is therefore an integral signal measuring Cs^+ concentration changes within all pore size regimes. The scattering integral parameters for Q-values larger than about $1nm^{-1}$ are restricted to processes taking place in micro- and mesopores. A local ion transport from the macropores between the carbon particles into the micro- and mesopores wouldn’t cause any observable transmission change. Indeed the fact that the transmission signal changes indicates that a net ion transport into the irradiated volume must take place, having its origin at the CE and the ion separator.

The transmission signals for all spots on the WE and for both D8 and D9 cell are given in Fig. 51. In chapter 4.2 a local dependency of the transmission signals of the D9 cell was discussed; due to the special cell design probably caused by the low carbon conductivity. In fact the D8 cell exhibits a local dependency as well, due to the metal contact at the backside of the WE most probably caused by ion diffusion. The time delay values of the different measurement spots on the WE

indicate indeed a local dependency of the ion concentration (Fig. 51). In Fig. 51b the absolute time-delay of the transmission in seconds for the different positions on the WE is plotted. According to the diffusion paths of the ions from the CE to WE, the time-delay increase towards the center of the measurement-window seems reasonable.

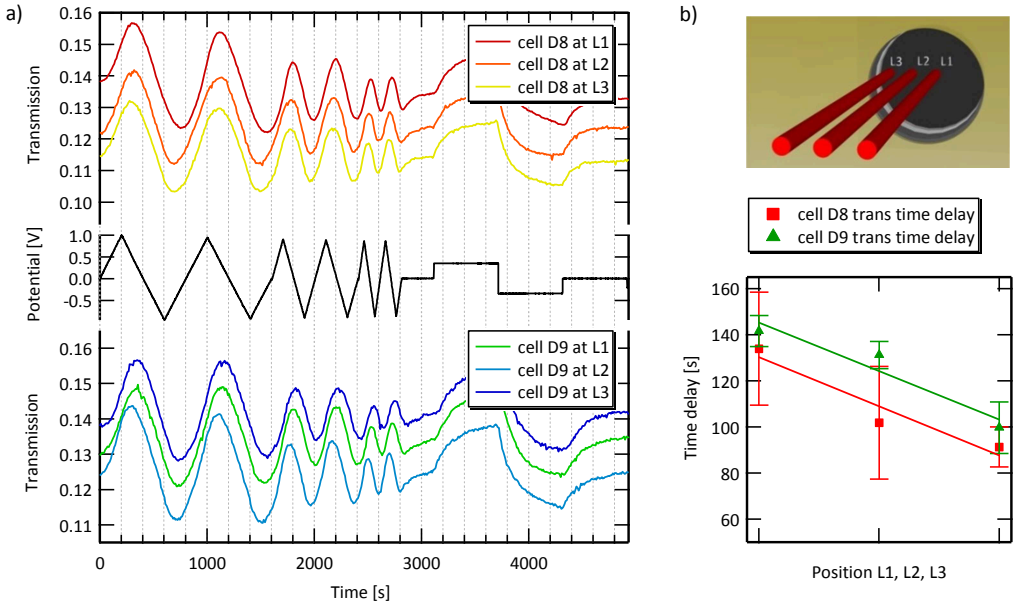

Fig. 51: In a) the transmission signals for both cells D8 and d9 at the positions L1, L2 and l3 are given. The transmission curves are arbitrarily shifted in y-direction. For both cells the time-delay with respect to the potential decreases when approaching the edge of the "measurement window" (see b)). The time delay of the D8 cell is in general lower, although not statistically relevant.

In particular the transmission signal of the D8-L1 measurement exhibits an asymmetry, having steeper positive slopes for the repelling of Cs^+ ions than negative slopes for the insertion of Cs^+ ions. Both Cs^+ and Cl^- have similar hydrated and dehydrated ion sizes and the mobility properties are similar as well (see section 3.1.2). Since the X-ray transmission signal is mainly sensitive to Cs^+ changes only, the insertion and desertion process obviously have a different time constant. However, this should be an intrinsic property of the Cs^+ ion movement when applying a potential and occur independently of the WE measurement spot. In order to proof these results further investigations on the Nanostar Lab SAXS/WAXS system have been performed (see Fig. 52). The time-delay was evaluated using a sinusoidal fit, even though there is no physical reason for a harmonic (sinusoidal) transmission behavior. In general the statistical noise is higher compared to the measurements with Synchrotron radiation. However, the sinusoidal fit shows the clear dependence of the time-delay on the local spot of the WE (red arrows). The asymmetry of the transmission signal seems to be a negligible effect; the local dependency effect is confirmed.

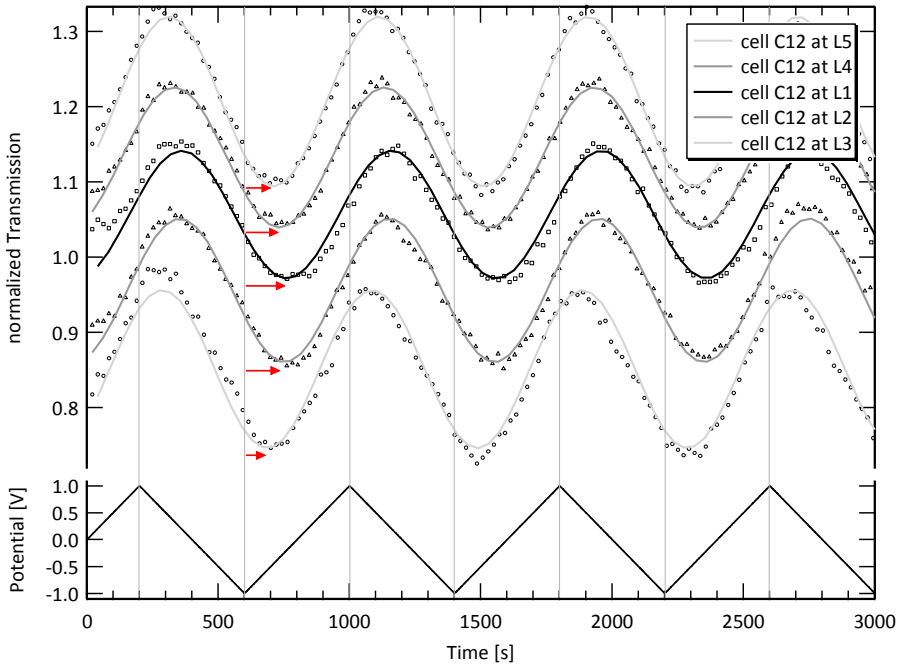

Fig. 52: Transmission signals measured on the in-house Nanostar SAXS system for a cell design similar to D8 at the positions L1, L2, L3, L4 and L5. The positions L4 and L5 correspond to L2 and L3 respectively, approaching the "measurement window" edge in the opposed direction than for L2 and L3. In contrast to the measurements at Elettra, for the current collector a ≈200nm thick platinum foil was used (C12 cell). The red arrows indicate the local dependency of the time delay.

The electrolyte filled pore volume within the space between the carbon particles (macropores) is roughly the same as the micro- and mesopore volume, as discussed in section 3.1.1. Thus the ions needed for electrosorption within the micro- and mesopores, could be provided by the bulk electrolyte in between the particles. The question arises what drives the ions moving the long distance from the CE to the WE.

A study of the integral parameters according to a more detailed Q-regime classification (according to Fig. 29) should provide further insight on the time-delay behavior discussed in particular for the D8-L1 measurement. The integral intensities for D8-L1 exhibit a periodic behavior with similar amplitude for all Q-regimes (Fig. 53). Furthermore at negative potentials a peak forms up when going to smaller Q-values. Both maxima or minima on the integrated intensity signal exhibit a different time-delay as compared to the transmission signal. The fact that the relative intensity change of the periodic contribution is equal for all Q-values (neglecting the peak formation at small Q-values) leads to the assumption that the Cs^+ concentration change is equal for all pore size regimes covered (two-phase-model). The oversimplified assumption that the Q-value corresponds to a distance in real space equal to π/Q is in general not true [66]. In particular for disordered structures like activated carbons all distances in real space contribute to a defined Q-

value, although for large Q-values the contribution of smaller distances (smaller pores) becomes larger and vice versa. Furthermore from the equal change of the ion concentration we can assume that the initial ion concentration is equal as well for all pore size regimes. In fact, in many simulation papers a strong dependency of the ion arrangement on the pore size was reported, especially when going below the pore size where space for one only hydrated ion is left [11-13].

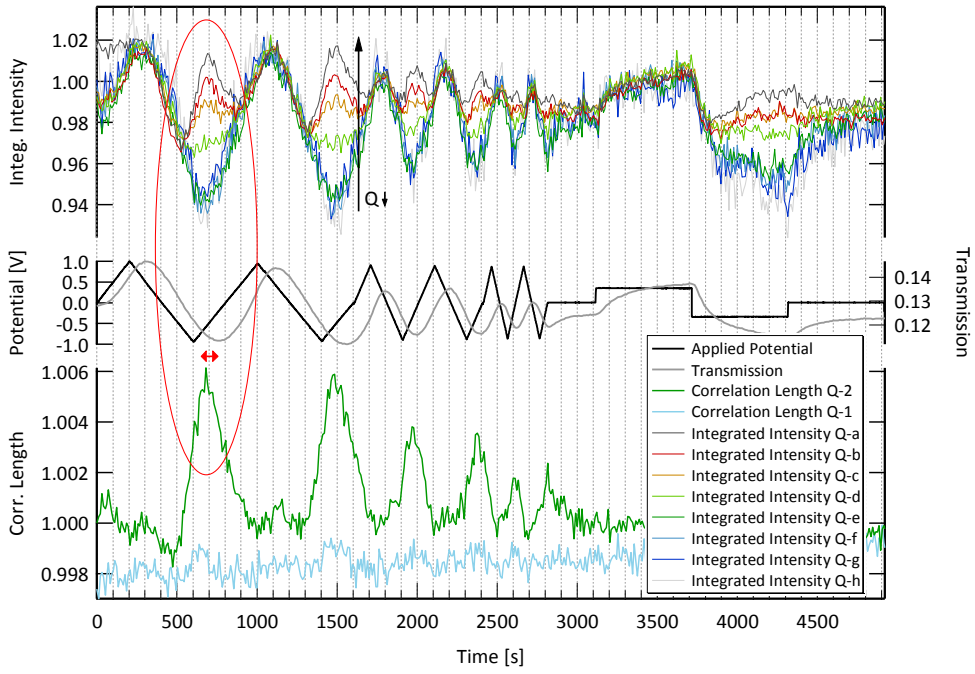

Fig. 53: Detailed integral parameter study of the D8-L1 measurement. At small Q-values and negative potentials an additional peak forms on the periodic integrated intensity signal. The peak formation at small Q-values is responsible for the correlation length peak of the Q-region Q-2. The red arrow indicates the different time-delay of the scattering signal as compared to the transmission signal (compare the time-delays of all signals within the red ellipse).

Due to the experimental restriction of Q-values below 5nm^{-1} one can assume in a good approximation that the electron density fluctuations of the single ions and water molecules within the pores are not resolvable with SAXS. One could argue that any detectable influence of e.g. electron density fluctuations are “corrected out” in the correlation length signal of Q-2 by the electrolyte structure factor subtraction procedure. If so, the additional contribution of e.g. electron density fluctuations would be subtracted equally for the complete SAXS curve (all Q-values)). Hence, even if such contribution is additionally subtracted it would become visible on signals for smaller Q-values (e.g. 2-3nm^{-1}), because in these regions such contribution can be excluded. This was however not observed. Most probably only an average electron density level of the electrolyte, hence only an average ion concentration change is detectable. Although the

arrangement of ions may change with the pore size, within the experimental precision the average density does not.

Since the scattering integral parameters are sensitive to changes within the micro- and mesopores, and the transmission signal is sensitive to all pore size regimes the experimental data indicate that processes take place on two time scales depending on the pore size regime; A rather fast ion transport into/from the micro- and mesopores and a slower transport into/from the macropores. A further comparison of the time delays of the scattering signals with the transmission signals of the first two CV cycles with a scan rate of 5mV/s leads to a better understanding (Fig. 54). While the transmission signals show clearly a local dependency, the scattering signal does not. Since the process within micro- and mesopores happen "fast" independently on the WE-spot, the macropores between the carbon particles indeed have to serve as ion reservoirs for the actual electrosorption process. The macroscopic ion transport and its local dependency occur only within the macropores and is in general "slower" than the electrosorption process. Only at the very edge of the "measurement window" the macroscopic and the local ion transport have similar time constants.

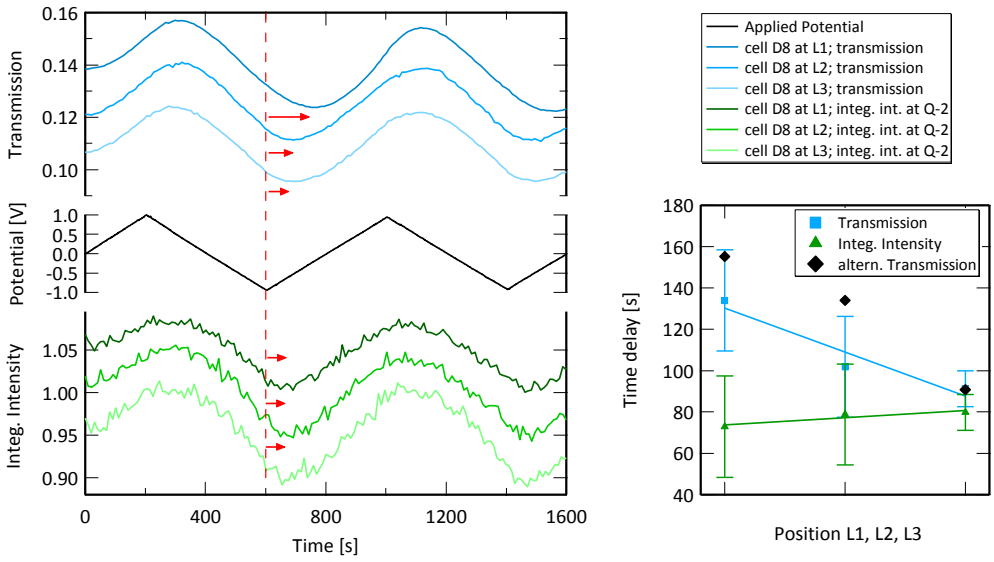

Fig. 54: Time delay study for both transmission and integrated intensity signals for the D8 cell at the positions L1, L2 and L3. While for the transmission signal the time delay increases when approaching the center of the WE, it stays constant for the integrated intensity. Since the experimental error for the time-delay values is rather high, the values of the in-house transmission measurements (shown in Fig. 52) are indicated as well ("altern. Transmission"). The values of position L2, L4 and L3, L5 were averaged respectively.

Exemplarily the situation at negative applied potentials is explained. For the following discussion we imply that the total ion concentration within the pores remain constant. Only the ratio of cations to anions is changed upon applying a potential. In section 4.4.2 this assumption is verified

by calculating absolute ion concentrations. If a negative potential is applied to the carbon electrode additional Cs^+ ions are forced to enter the micro- and mesopores coming from the macroporous surrounding. Simultaneously Cl^- are expelled from the micro- and mesopores leading to an excess amount of negative and a depleted amount of positive ions in the bulk electrolyte of the macropores. This excess amount of Cl^- again causes an electric field which tries on the one hand to expel the excess Cl^- ions and on the other hand attract Cs^+ ions from somewhere else. Since after complete electrosorption the charge on the carbon particle (e^-/h^+), counterbalanced by the ions within the micro- and mesopores, the unbalanced electrolyte system within the macropores have to be balanced by ions coming from the CE.

Not only the electric field but also the concentration gradient causes ions to diffuse from the CE or the ion separator to the specific spots on the WE. According to the Nernst-Planck equation (eqn. (33)) the concentration and the electric potential gradient determine the ionic flux. In the case of a complete decoupling of the two ion transport processes or an infinitesimal time step, at positive potentials Cs^+ ions are first repelled from the meso- and micropores and simultaneously accumulated in the macropores. Responding to this process a macroscopic ionic flux sets in, caused by the step-like concentration or electric potential function within the bulk electrolyte of the macropores (as sketched in Fig. 55 on the top). The gradient of both ion concentration and electric potential and thus the ionic flux is highest at the edge of the measurement window near to the CE and the ion separator. Therefore the time delay is smallest at the edge of the measurement window. In the case of negative applied potentials a step like function opposed to the one sketched leads to the opposed macroscopic Cs^+ ion transport. In both cases the time-delay is largest in the center of the WE “measurement window”.

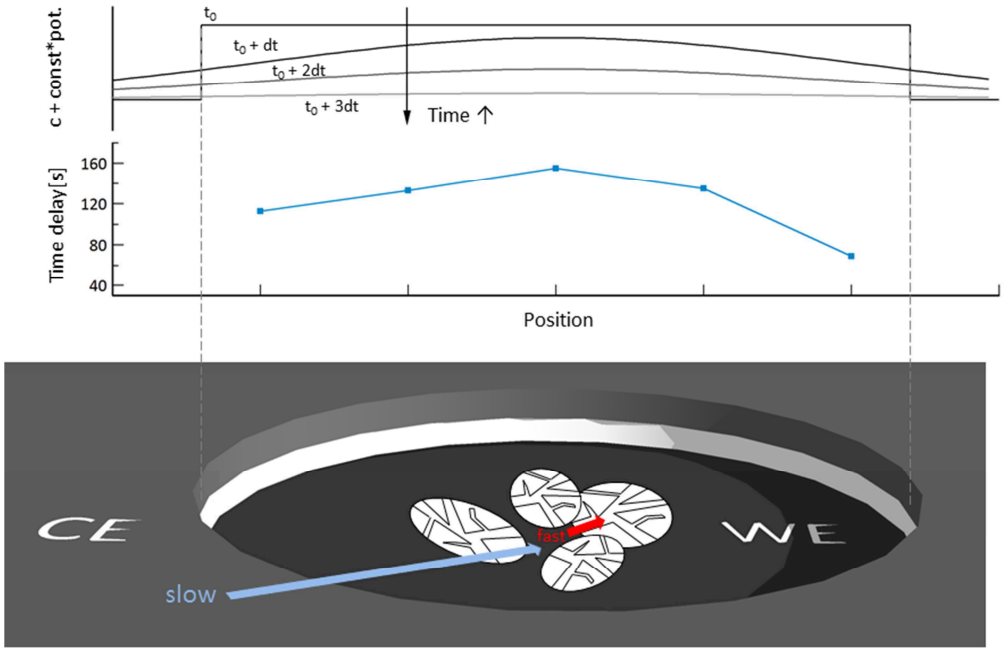

Fig. 55: Sketch of the ion transport mechanisms happening with different time constants on different hierarchical levels. After the "fast" electrosorption into the micro- and mesopores took place a retarded, "slow" macroscopic ion transport sets in. In reality both processes happen simultaneously and can only be investigated due to the large time-delay for the macroscopic transport in the center of the electrode. The time-delay values of the transmission measurement shown in Fig. 52 are given in blue. Furthermore the sum of the concentration and potential gradient at positive potentials for an infinitesimal time step is sketched on the top.

The question arises whether the described kinetic behavior can have a direct influence on the supercapacitor performance. Since the actual electrosorption happens faster, the influence of the slower macroscopic transport on the power density capability should not be too large. Still, a certain degree of coupling between the electric field within the macropores (built up due to the excess amount of one ion species) and the electric field of the charge carriers on the carbon side (forcing ions to go into the micropores) may slow down the charging process. Therefore an optimized cell design with small distances between CE and WE seems to be best for highest current densities. Furthermore a certain volume of ion reservoirs surrounding the parts with highest porosity is certainly advantageous, since the ions for electrosorption are provided from there.

At very low scattering angles the porod regime of the carbon particle scattering represents the main contribution to the scattering intensity (see Fig. 25). For a detailed investigation of the carbon particles one has to go far below $0.3nm^{-1}$ (Ultra-SAXS). Nevertheless in Fig. 56 the correlation length signals for the lowest measured Q-values are shown.

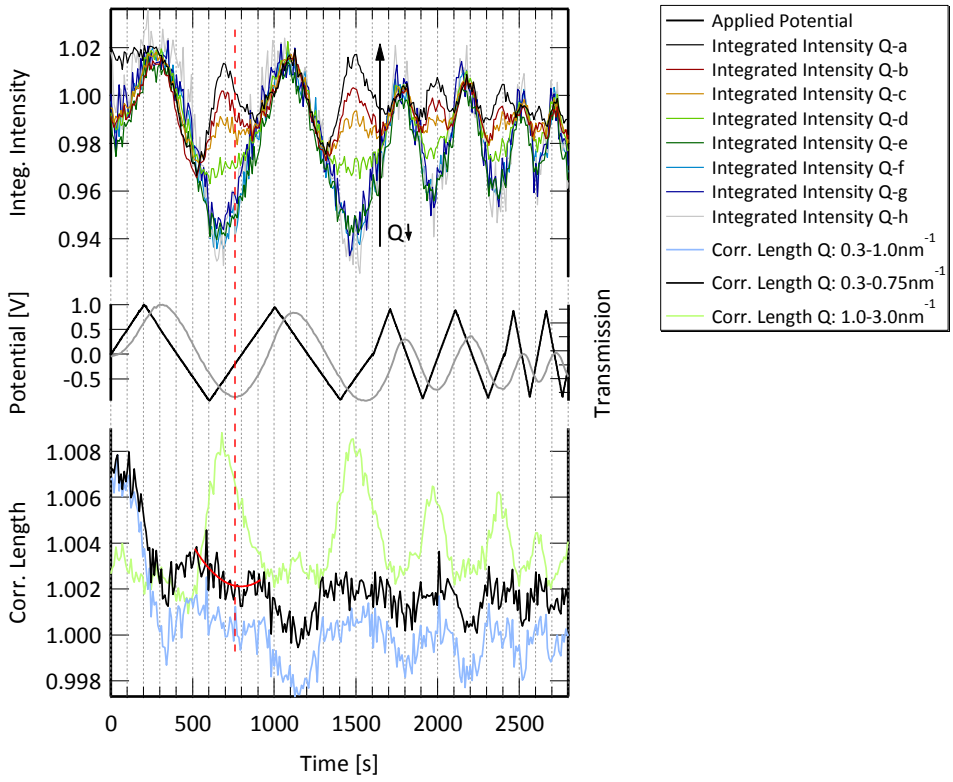

Fig. 56: Detailed integral parameter study of the D8-L1 measurement. Going to smallest possible Q-regimes (macropore contribution via the particle porod regime) a minimum on the correlation length signal with a time-delay equal to the transmission signal was found.

Due to the small width of the Q-regime the signal is very noisy and it is clear that no major statement can be based on this data, but for negative potentials a minimum seems to be present with a time delay different to the other scattering signals and similar to the transmission signal (see red polynomial fit). If the minimum is real, this would be a further proof for the slow ion transport within the macropore regime. Although the quality of the data in Fig. 56 is too bad, to draw a final conclusion on the time-delay behavior, the investigation of smaller Q-regimes could lead to a better insight on time-dependent processes within the macropores.

Also for the cell design D9 a local dependency of the transmission signal was found. Here, in contrast to D8 also the scattering signal exhibits a local dependency (Fig. 57). The time-delay values of the transmission signal and the scattering signal behave similar, although the scattering signal values are systematically shifted to lower time-delays. In the case of the D9 cell not the ion mobilities are detrimental for kinetic effects but predominantly the low carbon conductivity, as discussed before. The electrons or holes within the carbon electrode have to travel a long distance to the center of the WE measuremen-window, having its origin in the CC. In this case the actual electrosorption, which corresponds to ion diffusion from the macroscopic reservoirs into

the micro- and mesopores, exhibits a local dependency caused by the electric transport within the carbon. The macroscopic transport from the CE into the macropores of the irradiated volume exhibits an additional retard (transmission signal), indicated as rather constant time delay difference between the two curves in the inset on the right (Fig. 57).

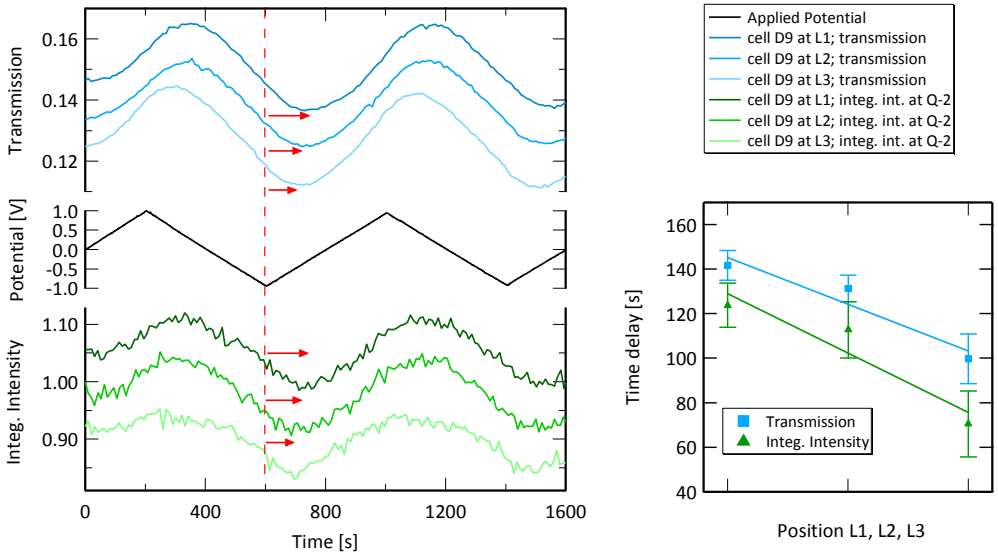

Fig. 57: Time delay study for both transmission and integrated intensity signals for the D9 cell at the positions L1, L2 and L3. Both transmission and integrated intensity signal show a local dependency of the time-delay values. Note the difference to the cell D8 as shown in Fig. 54. The absolute time- delay values are not completely comparable since they depend on the detailed cell design. In the case of the D9 cell the carbon conductivity seems to be mainly responsible for the local dependency of the time-delay.

The delay of the transmission compared to the integrated intensity signal is caused by the kinetics of the macroscopic ion transport which was explained in detail for the D8 cell. Since the kinetic effect due to the carbon resistance is assumed to dominate in the case of the D9 cell, the macroscopic ion transport does not cause an additional increase of the transmission signal slope with respect to the integrated intensity slope (inset on the right in Fig. 57). In the case of cell design D9 the low carbon conductivity limits the power density of the supercapacitor cell. Depending on the cell design either the ion mobilities or the carbon conductivity can be critical.

The electrochemical data of the D8 measurement series for the 5mV/s scan rate is given in Fig. 58a. The cyclic voltamograms reveal significant changes with further cycling. These changes are attributed to the corrosion of the golden current collectors. However, the impact of this electrochemical reaction on the in-situ scattering and transmission data is most probably small, since the changes in the CVs do not correlate with any position dependent quantity gained from scattering or transmission signals. In Fig. 58b the cyclic voltammogram of the in-house measurements shown in Fig. 52 (L1, L2 and L3) are indicated. The C12 cell design is equivalent to

the D8 cell design, apart from the current collector material. For C12 platinum was used instead of gold, inhibiting the strong corrosion reactions. Still the influence of reactions is visible (at large positive and negative potentials), probably due to the degradation of water. However, the in-house measurements using C12 exhibit reliable CVs. The local dependency of the transmission signals was still visible (see Fig. 52). Hence, the instability of the CVs of the D8 measurement series seems to have no impact on the conclusions drawn above. The CVs of the D9 measurement series behaved similar.

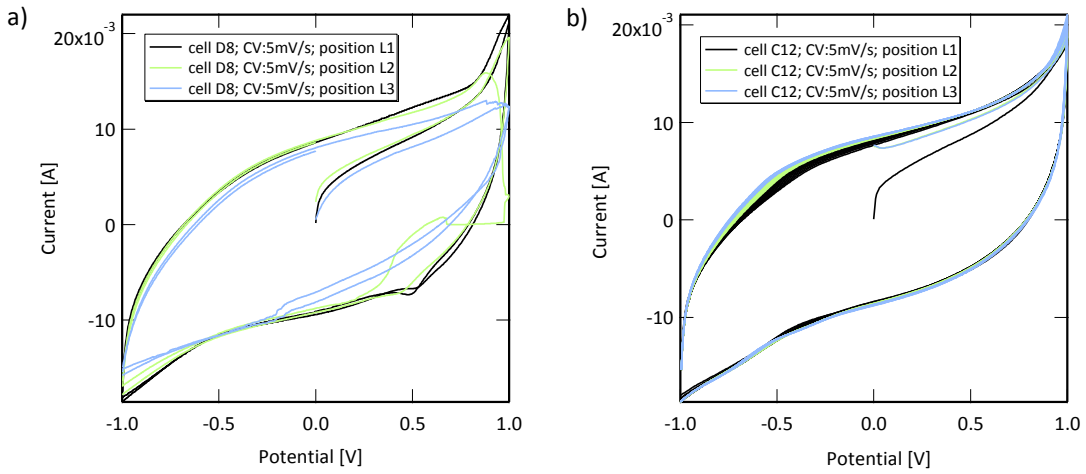

Fig. 58: a) Cyclic voltammogram (CV, scan rate 5mV/s) of the D8 measurement series (L1, L2 and L3). With further cycling the CVs changed significantly. In b) the cyclic voltammogram of the C12 measurements are shown. The C12 cell design corresponds to the D8 cell design apart from the use of platinum CCs instead of a golden CCs.

4.4.2 Pore swelling behavior

So far no explanation for the formation of the integrated intensity peak at small Q-values was given. A commonly known effect in highly porous supercapacitor electrodes is the significant swelling of the electrode when applying a potential. It is sometimes explained by an increased pressure due to an increase of the total ion concentration [Cs^++Cl^-] within the pores [18, 19]. Thus the origin of the macroscopic expansion is most probably the swelling of micro- and mesopores, which can be basically recorded with scattering.

As explained in chapter 4.1 the scattering curve of highly porous carbon materials is often described by the DAB model developed for randomly oriented porous materials (eqn. (41)). The correlation length occurring in the DAB model corresponds to the 1/e width of the exponentially decaying correlation function and is a measure for the average pore diameter [68]. Changing this parameter leads to a qualitative understanding how an isotropic expansion of the porous material affects the scattering intensity, indicated in Fig. 59. Going to smaller Q-values leads to a significantly increased scattering intensity for larger pore diameters. At larger Q-values the

increase becomes smaller and smaller. The slope for Q-values from 3-5nm^{-1} is steeper for the increased pore diameter. At very large Q-values the scattering intensity decreases in the case the pore diameter is increased.

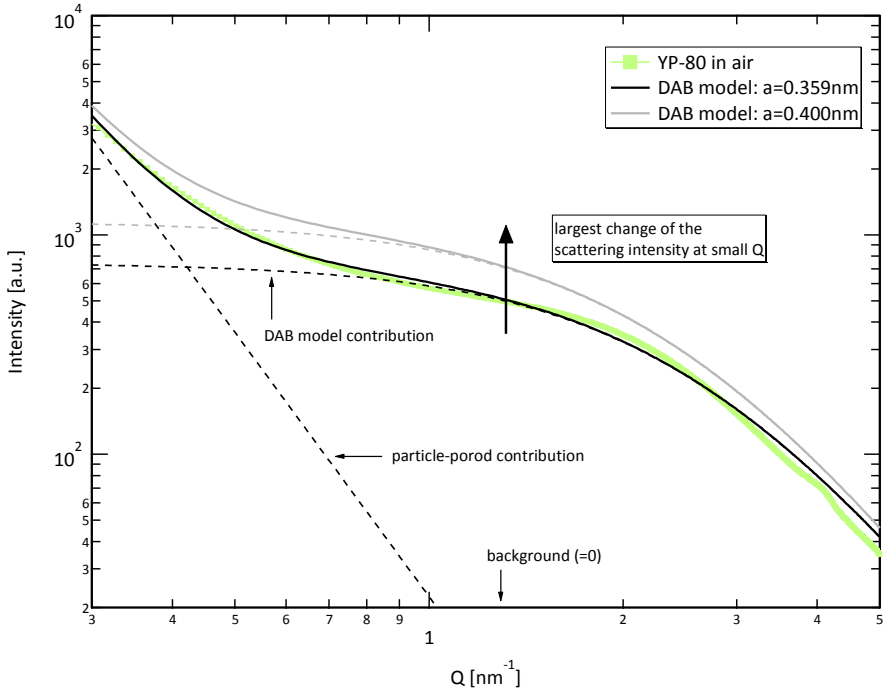

Fig. 59: The measured scattering intensity of YP-80 in air in comparison to the simulated scattering intensity of the DAB model (according to eqn. (41)) with a correlation length parameter of 0.359 and 0.40 respectively. The model curve with a=0.359 correspond to the best fit to the experimental data. The hypothetical model curve with a=0.40 should emphasize the impact of an increase in the average pore diameter on the SAXS curve. In reality changes about a factor of 10^{-3} were observed. The integrated intensity change is largest at small Q-values (note the logarithmic scale).

The behavior observed for the DAB model provides a hint on the nature of the peak formation in the integrated intensity signal at negative potentials. Like in the DAB model above for the D8-L2 measurement a significant integrated intensity increase is only seen for Q-regimes smaller than 3nm^{-1} (integrated intensity peak at negative potentials in Fig. 60). Since the intensity increase becomes larger at small Q-values, the slope of the SAXS curve in these regions will become steeper. Hence, the correlation length will increase, observable on the distinct peak in the correlation length signals at negative potentials. The periodic change of the integrated intensity caused by the changes of the electrolyte electron density level is equal for all Q-regimes and has thus no effect on the correlation length signal. The peaks in the correlation length signal might be a direct measure for the pore expansion.

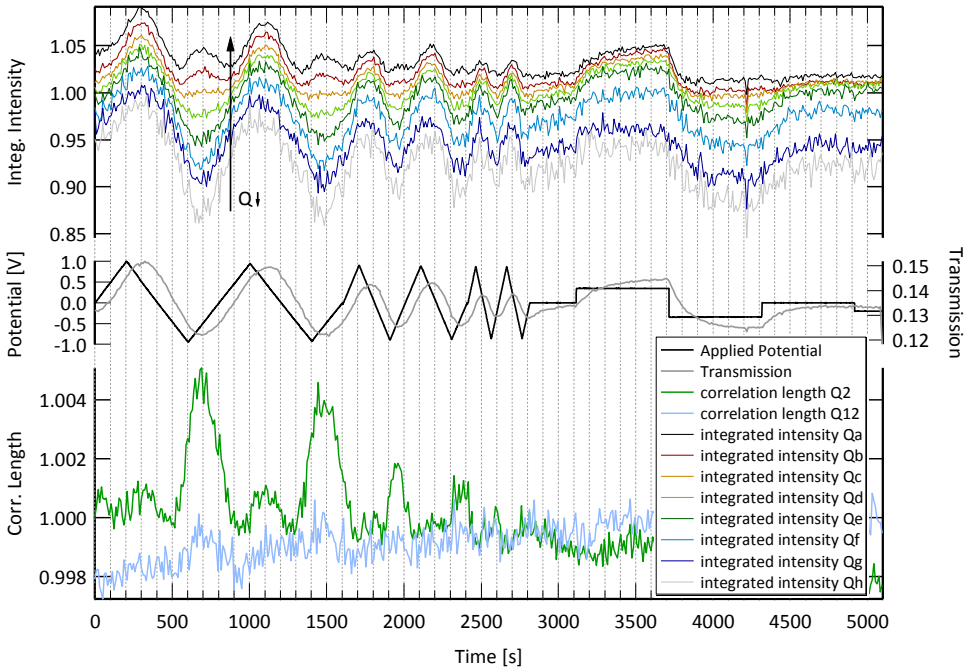

Fig. 60: Detailed integral parameter study of the D8-L2 measurement. At small Q-values and negative potentials an additional peaks forms on the periodic integrated intensity signal. The peak formation at small Q-values is responsible for the correlation length peak of the Q-2 region and may be attributed to pore swelling.

In order to check the pore swelling hypothesis a complementary dilatometry measurement of the macroscopic electrode expansion, applying a CV cycle with 5mV/s, was performed by Weingarth D., Presser Group, INM Saarbrücken (see Fig. 61). At negative potentials a large expansion and at positive potentials a small contraction was found. When starting from 0V the electrode contracts upon applying positive potentials. Around 0.5V the electrode starts to expand but remains in the negative strain regime. Going from 1V to 0V the electrode contracts again before it expands upon applying negative potentials. The dilatometry peaks indeed correlate nearly perfectly with the correlation length peaks of the scattering signal. This crosscheck proofs the possibility of measuring pore size expansions in the order of 10^{-3} using In-situ SAXS, even for very disordered pore systems like activated carbons. Recently several dilatometry studies of the macroscopic electrode expansion have been accomplished to study the ion kinetics within supercapacitor electrodes [8, 9, 18, 19]. The physical origin of swelling is still not clear, but the kinetics might be related to that of the actual electrosorption process.

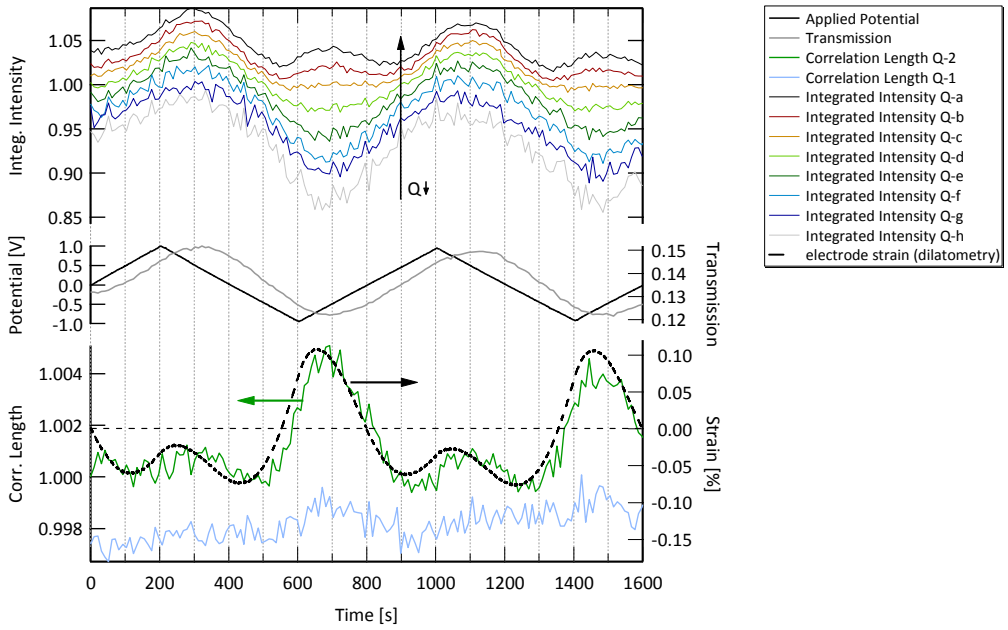

Fig. 61: Detail of Fig. 60. Furthermore the macrosocopic electrode strain measured by dilatometry is indicated (dashed black on the bottom). The integrated intensity and correlation length signal is shifted arbitrary in y-direction for better visualization. The dilatometry measurements were performed by Weingarth D., INM Saarbrücken.

Only two known dilatometric studies have reported contraction on charging carbon electrodes so far. In many times at positive polarizations a small expansion and at negative polarizations a large expansion occurred. Often the swelling effect is referred to an increased total ion concentration upon charging (as sketched in Fig. 62a) leading to an increased pressure (e.g. due to steric repulsion of ions) acting against the pore walls [18, 19]. Consequently the increased pressure should depend on the individual ion size [9]. An increase of the total ion concentration [Cs^++Cl^-] within the pores is possible if more ions are inserted into the pores than ions of the other sign are expelled when applying a potential.

The so-called “insertion model” assumes that at 0V conditions a significant amount of pores is not filled with electrolyte [19]. When applying a potential some of these pores are filled, leading to a pressure within the pores and causing the macroscopic swelling of the electrode (→ electrochemical activation [22]). This mechanism is very similar to the idea of a total ion concentration increase upon charging within every single pore. Here, at 0V conditions all pores would be already filled with electrolyte [19]. However, with a calculation of the ion concentration change using the transmission signal, one would not be able to distinguish between the insertion model and the total ion concentration increase within every single pore. An increase of the total ion concentration within a specified measurement volume would be recorded in both cases.

If the pore swelling/contraction as shown in Fig. 61 could be reduced to the total ion concentration change, the ion concentrations may behave as sketched in Fig. 62b. Since both ions have a similar size and similar diffusion coefficients (section 3.1.2) such asymmetric behavior seems unlikely. Furthermore the electrode strain as shown in Fig. 61 suggests the presence of more than one mechanism responsible for the strain. In particular the behavior at positive potentials (where both contraction and expansion occurs) indicates that the strain is not only controlled by the total ion concentration.

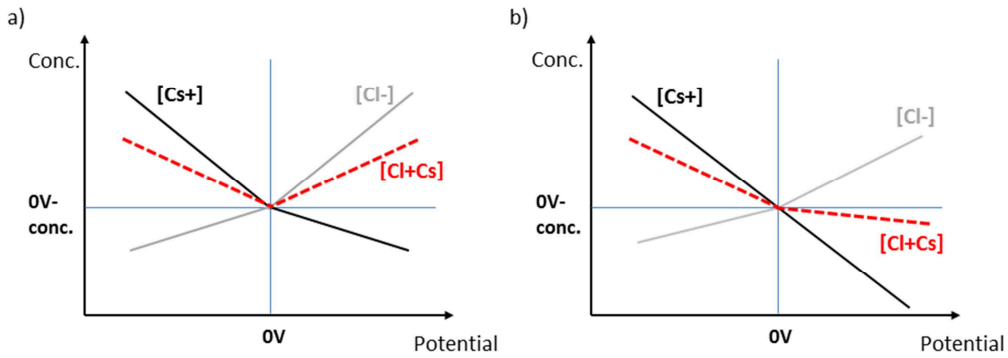

Fig. 62: Hypothetical potential-concentration dependencies within the micropores. The total ion concentration [Cl+Cs] corresponds to the sum of the [Cs^+] and the [Cl^-] contribution. Assuming that the pore strain correlates with the total ion concentration only the situation sketched in a) corresponds to equally expanding pores for both negative and positive potentials. Assuming a large expansion at negative polarization and a small contraction at positive potentials both the total and the single ion concentration behavior is rather asymmetric (as sketched in b)).

In order to study the ion concentration changes of both Cs^+ and Cl^- ions, the equilibrium transmission values are analyzed as described in section 4.3.2. Two positive and negative CA potential steps with ±0.5V, were applied to the In-Situ cell, while the transmission change was recorded with the Nanostar set-up (Fig. 63). The concentration change for both ion species is in the order of 0.5E+20 cm^{-3} starting with an initial concentration of 5.5 – 6.022E+20 cm^{-3} (which corresponds to 1mol/l).

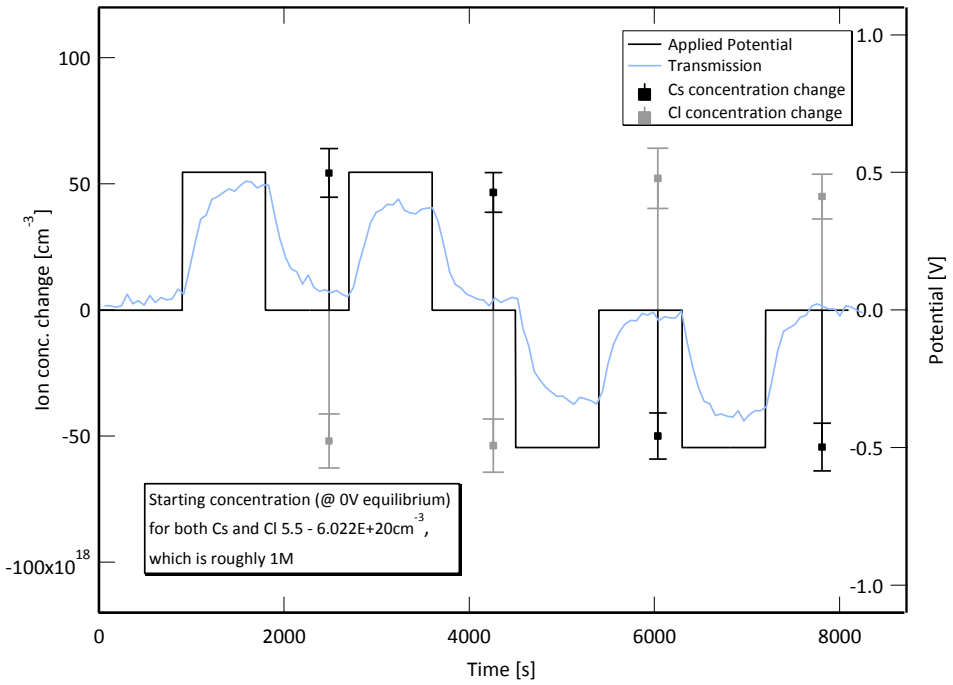

Fig. 63: Calculation of the absolute ion concentration change for the discharge of the indicated potential steps (black), according to the procedure described in section 4.4.2. The Cs^+ and the Cl^- concentration change is indicated in black and grey, respectively. The transmission signal is shown in blue.

The initial ion concentration was calculated from the transmission measurement of the dry carbon, the carbon infiltrated with water and the carbon infiltrated with electrolyte at 0V, as described in detail in section 4.3.2. As indicated in Fig. 64 the concentration change of the single ion species behave completely symmetric. The measurement exhibits a constant total ion concentration within the pores for both positive and negative potentials. A recent NMR-study on supercapacitor using organic electrolytes revealed a similar behavior for the absolute ion concentrations. Further measurements with ion concentration calculations at different potentials are necessary to proof the validity. Both hydrated and crystal ion diameters are rather similar (see section 3.1.2). In fact Cl^- is slightly larger, according to the calculated concentrations the pores would expand at positive and contract at negative potentials. Thus the simple hypothesis of an increased total ion concentration being responsible for the pore swelling is not supported by the measured data. Other mechanisms, as introduced in section 2.2.4 have to play an important role.

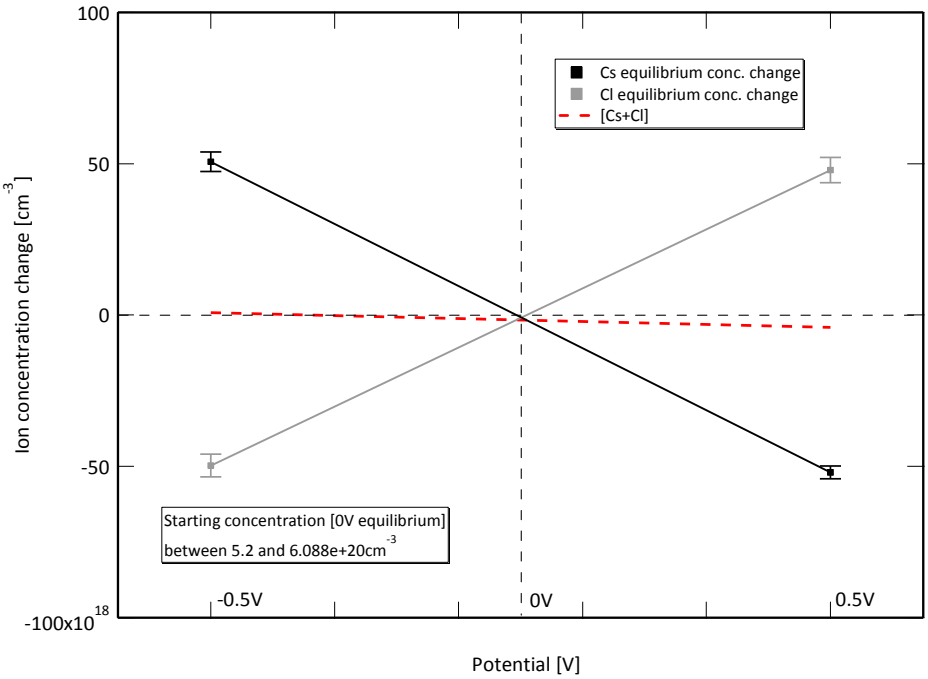

Fig. 64: The symmetric behavior of both ion species leads to a constant total ion concentration, leading to the conclusion that the mechanical pressure caused by the increased ion concentration cannot explain the observed pore swelling behavior.

Furthermore the concentration calculation indicates the presence of completely electrolyte-wetted electrodes at 0V, as predicted in [11, 14]. No additional electrolyte is forced into empty pores upon applying a potential. The charge accumulated on the electrode side is counterbalanced by changing the initial balance of cations and anions within the micropores. The total concentration remains constant. Depending on the potential one ion sort is depleted the other accumulated, as already reported in a recent NMR study [75].

In order to be sure that the ion concentration changes can be really attributed to changes within the micro- and mesopores a comparison of the transmission signal with the actual number of electrosorped charges (from the current signal) offers supporting arguments. Since the absorption coefficient of Cl^- is about one order of magnitude smaller than the one of Cs^+, in a good approximation we can neglect the Cl^- term in eqn. (46) for the transmission. Therefore the Cs^+ concentration change can be calculated directly (see Table 7). If we assume the mentioned symmetric behavior (same Cs^+ and Cl^- concentration changes) the Cs^+ concentration within the micropores can be estimated alternatively from the current signal (integration of current gives the charge Q; the half of the charge per pore volume gives the Cs^+ concentration; $[Cs^+]=Q/2V_{pore}$). Comparing these two quantities in Table 7 leads to the conclusion that indeed the cation concentration change measured by the transmission is similar to the number of electrosorbed

cations. Thus the concentration change tracked by transmission most probably corresponds to the concentration change within the micropores.

Table 7: Calculated change of the number of Cs^+ ions for a discharge CA step from ± 0.5V to 0V with the transmission signal (corresponds to a macroscopic ion transport) and the current signal (corresponds to the actual electrosorped ions)

	Cs^+ concentration change	**Cs^+ concentration change**
Calculated from	**Transmission signal**	**Current signal**
CA discharge: +0.5V -> 0V	4.86e+19cm^{-3}	5.06E+19cm^{-3}
CA discharge: -0.5V -> 0V	4.47e+19cm^{-3}	4.97E+19cm^{-3}

Furthermore, from the discussion of the kinetic behavior as described in section 4.4.1 one could already come to the conclusion that the transmission signal have to track the concentration change within the micropores. Neglecting the kinetic effects, the equilibrium concentration within the macropores should be 1mol/l. Hence only the excess/deficiency amount of ions within the micropores can lead to the transmission change.

Another remarkable result is the symmetry of the transmission signal change for charging both positively and negatively (e.g. Fig. 60, transmission is symmetric around x-axis). This means that roughly the same number of Cs^+ ions is inserted into the porous structure of the irradiated WE-volume for positive potentials, as Cs^+ ions are expelled at negative potentials. Apart from the exact ion concentration evaluation this fact provides already a strong hint on the constant total ion concentration for all applied potentials (as seen in Fig. 64), assuming a similar concentration behavior for Cl^- ions.

In general an asymmetric behavior (large expansion at negative and smaller expansion at positive potentials) of the pore swelling was found for a variety of different electrolyte systems [8, 9, 18, 19]. Changing systematically the ion sizes could not explain the asymmetric behavior indicating that the increase of the total ion concentration cannot be the only explanation [19]. An important factor is certainly the interaction of solvent molecules with the carbon surface. A swelling of highly porous materials upon changing the humidity or the water content within the material is a well-known effect [76]. However, the asymmetry was also found for ionic liquids having no solvent [18]. The electrocapillary effect, as described in section 2.4.5, might play a role. The expansion should however be mainly symmetrical, except of influences of specifically adsorbed species.

What remains is the influence of the electrode material. In some carbon materials, depending on the conductivity, a space charge region significantly contributes to the total double-layer capacitance [47]. According to [52] the change of the binding energy of the surface atoms upon

adding electrons/holes could be responsible for a change in the surface stress, leading to a macroscopic strain in highly porous materials. As described in section 2.4.5 the insertion of electrons in the antibonding or the withdrawal of electrons in the bonding states of carbon materials may be responsible for the swelling at both positive and negative polarizations. Quantum capacitance behavior of the carbon can be directly related to the density of states of electrons [47]. Thus the occurrence of such behavior in CV diagrams may be related to the swelling behavior of the carbon. So far this explanation would fit to recent findings in literature.

However, the strain found for the system studied in the present work was negative at positive potentials and positive at negative potentials. Recent studies on different carbon electrode materials have shown a similar behavior with a contraction at positive and expansion at negative potentials [20, 21]. Furthermore a DFT calculation for graphite intercalation compounds and carbon nanotubes revealed an increased C-C bonding length for negative polarization and vice versa for positive polarization using the jellium model [53, 54].

Within the experimental precision the total ion concentration in the micropores was found to be constant. As mentioned before the strain behavior at positive potentials might be caused by two contributions. Let's assume that the carbon electrode changes its interface properties upon charging as in [20, 21] leading to the large expansion at negative potentials and the contraction at positive potentials. Since the dehydrated Cl^- diameter is slightly larger and the total ion concentration was found to be constant a slightly increased pressure within the micropores might occur at positive potentials (increased amount of Cl^-). Hence the small expansion peak at large positive potentials may be caused by the contribution of an increased electrolyte pressure (due to the repulsion of Cl^- ions). This contribution is superimposed by the large strain contribution originating from the carbon electrode. However, further investigations are definitely necessary to get closer insights into the physical origin of pore swelling upon electrosorption.

In general the possible mechanisms inducing a macroscopic electrode strain upon charging either be related to a change in the isotropic electrolyte pressure inside the pores or to a change in the interface properties and hence the surface stress. Studying the strain on the atomic level by tracking the carbon diffraction peak shifts using in-situ X-ray diffraction may enables a distinction between these two mechanisms. The change in the electrolyte pressure acting on the pore walls would lead to an isotropic strain, causing shifts for both (002) and (10) diffraction peaks. An interface strain in slit-like pores may only be visible on the (10) in-plane peak shift [72].

5 Conclusions and outlook

In the present thesis the ion dynamics within a highly porous activated carbon electrode of a working Electrical Double-layer Capacitor (EDLC) or supercapacitor was investigated by In-situ Small-Angle X-ray Scattering (SAXS). In order to reach a time-resolution of seconds highest photon flux is required, only provided by Synchrotron radiation X-ray sources. Thus, the Scattering experiments were performed at the Austrian SAXS beamline on the Synchrotron facility ELETTRA, Trieste (Italy).

To study the ion concentration changes in different pore size regimes (micro-, meso- and macropores) and hence the different ionic fluxes, a special In-situ supercapacitor cell was developed. Beside the experimental difficulties in particular the data interpretation was challenging. The observed changes of the scattering signals are small. Nevertheless, stable integral parameters could be defined describing changes in the scattering curve as a function of time. To distinguish between processes on different size levels the integral parameters were calculated for several Q-regimes. In general the resulting integral parameter signals showed a rather complex behavior, due to different contributions to the scattering signal. The structure factor of the liquid electrolyte shows features mainly at Wide Angle X-ray Scattering (WAXS) Q-region and can be assumed to be constant in the SAXS Q-region. In order to reduce complexity, a fitting procedure was developed which evaluates the constant structure factor in the SAXS region as a function of the applied electrical potential. Subtracting this contribution leads to time-dependent signals which are much easier to interpret. In fact only the high time resolution allowed us to attribute scattering intensity changes to physical processes like the ion movement within the porous structure.

Beside the distinction between processes in different pore size levels (in particular at the level of macropores and meso-/micropores, respectively) a local dependency on the investigated electrode of the in-situ supercapacitor cell was found. Studying the local dependency of both transmission- and integral SAXS signals enabled a way to analyze the ion kinetics in different pore size regimes. The ion transport was found to take place in two separate processes, having different time constants and only distinguishable due to the special cell design. Upon applying an electrical potential, a local ion transport from the macropore volume (which serve as ion reservoirs) into the micro- and mesopore volume takes place, representing the actual electrosorption process according to the current signals. Depending on the cell design, the transmission signals have revealed a local dependency while the integral SAXS signals have not.

The transmission signal, which correlates to the concentration change within all pore size regimes (micro-, meso- and macropores), in general exhibited a larger time constant than the SAXS integral signals. Hence, a macroscopic diffusion process of ions from one electrode to the other only seems to take place within the macropores and as a response to the local transport into the micropores. A detailed study of the Ion transport using in-situ SAXS and providing a distinction between different pore size regimes, has been accomplished for the first time in microporous carbon based supercapacitors.

Furthermore micropore swelling in the order of 10^{-3} was tracked using In-situ SAXS and compared to the macroscopic electrode expansion recorded by dilatometry. In contrast to recently performed dilatometry studies [8, 9, 18, 19] at negative applied potentials a large expansion and at positive potentials a small contraction was found. In order to test the hypothesis of a relation between the total ion concentration (within the micropores) to the pore expansion, a new method to calculate absolute ion concentrations was developed. The cation and anion concentration change was evaluated, analyzing the transmission signal change of a chronoamperometry (step-like voltage signal) discharge cycle together with the electrosorbed charge gained from the integration of the current signal. Within the experimental precision these data suggest that the total ion concentration remains constant for both positive and negative potentials. Since the ionic sizes of both Cl^- and Cs^+ ions are similar the change of the electrolyte pressure (repulsion of the species within the micropores) seems to play a minor role in terms of pore expansion/contraction. It is believed that the carbon plays a critical role, but further systematic investigations are necessary to proof this hypothesis.

The better understanding of the ion kinetics in pores on different hierarchical levels and depending on the cell geometry may has an impact on the optimization of the power density of modern supercapacitors. The fact that macroscopic ion transport only takes place as a response of the local transport (which is responsible for electrosorption) might be considered for optimized cell designs. A hierarchically ordered pore system with larger ion reservoirs enabling a fast local electrosorption process, seems to be ideal to achieve high power densities.

This thesis is only a first step towards a contribution of SAXS to a better understanding and tailoring of electrical energy storage devices. Future activities may include experiments on the impact of different ion sizes on the kinetics. A dependency of the ion concentration change on the ion diameter is expected (→ ion sieving effect [7]). Furthermore in-situ WAXS enables the tracking of carbon diffraction peak shifts, may leading to a better understanding of the mechanisms contributing to pore swelling.

In order to understand the physics behind the various processes taking place simultaneously an electrode material with a less complex and more ordered structure in terms of scattering should

be utilized. A SAXS model could be applied to extract detailed information on the ionic arrangement and ordering, similar to a recent study on the investigation of water structure in confinement [77].

A different approach to gain information on the ion structure within the micropores might be the exact measurement of the electrolyte structure factor. The study of possible correlation peaks due to the ordering of electrosorbed ions could provide information on the ion arrangement within the micropores.

References

1. Béguin, F. and E. Frackowiak, *Supercapacitors; Materials , Systems, and Applications*. Materials for Sustainable Energy and Development, ed. G.Q. Max Lu. 2013, 69469 Weinheim, Germany: Wiley-VCH Verlag GmbH & Co.KGaA.
2. Simon, P. and Y. Gogotsi, *Materials for electrochemical capacitors.* Nature Materials, 2008. **7**(11): p. 845-854.
3. Conway, B.E., *Electrochemical Supercapacitors; Scientific Fundamentals and technological Applications*. 1999.
4. Chmiola, J., et al., *Anomalous Increase in Carbon Capacitance at Pore Sizes Less Than 1 Nanometer.* Science, 2006. **313**(5794): p. 1760-1763.
5. Chmiola, J., et al., *Desolvation of ions in subnanometer pores and its effect on capacitance and double-layer theory.* Angewandte Chemie - International Edition, 2008. **47**(18): p. 3392-3395.
6. Wang, H., et al., *In situ NMR spectroscopy of supercapacitors: Insight into the charge storage mechanism.* Journal of the American Chemical Society, 2013. **135**(50): p. 18968-18980.
7. Mikhael, D.L., et al., *Application of a quartz-crystal microbalance to measure ionic fluxes in microporous carbons for energy storage.* Nature Materials, 2009. **8**(11): p. 872-875.
8. Arruda, T.M., et al., *In situ tracking of the nanoscale expansion of porous carbon electrodes.* Energy & Environmental Science, 2013. **6**(1): p. 225-231.
9. Hantel, M.M., et al., *In situ electrochemical dilatometry of carbide-derived carbons.* Electrochemistry Communications, 2011. **13**(11): p. 1221-1224.
10. Richey, F.W., et al., *Ion Dynamics in Porous Carbon Electrodes in Supercapacitors Using in Situ Infrared Spectroelectrochemistry.* Journal of the American Chemical Society, 2013. **135**(34): p. 12818-12826.
11. Merlet, C., et al., *On the molecular origin of supercapacitance in nanoporous carbon electrodes.* Nat Mater, 2012. **11**(4): p. 306-310.
12. Feng, G. and P.T. Cummings, *Supercapacitor Capacitance Exhibits Oscillatory Behavior as a Function of Nanopore Size.* The Journal of Physical Chemistry Letters, 2011. **2**(22): p. 2859-2864.
13. Feng, G., et al., *Ion Distribution in Electrified Micropores and Its Role in the Anomalous Enhancement of Capacitance.* ACS Nano, 2010. **4**(4): p. 2382-2390.
14. Kondrat, S. and A. Kornyshev, *Superionic state in double-layer capacitors with nanoporous electrodes.* Journal of Physics: Condensed Matter, 2011. **23**(2): p. 022201.
15. Kondrat, S. and A. Kornyshev, *Charging Dynamics and Optimization of Nanoporous Supercapacitors.* The Journal of Physical Chemistry C, 2013. **117**(24): p. 12399-12406.
16. Shao, L.-H., et al., *Electrically Tunable Nanoporous Carbon Hybrid Actuators.* Advanced Functional Materials, 2012. **22**(14): p. 3029-3034.

17. Torop, J., et al., *Nanoporous Carbide-Derived Carbon Material-Based Linear Actuators.* Materials, 2009. **3**(1): p. 9-25.
18. Kaasik, F., et al., *Anisometric charge dependent swelling of porous carbon in an ionic liquid.* Electrochemistry Communications, 2013. **34**(0): p. 196-199.
19. Hantel, M.M., D. Weingarth, and R. Kötz, *Parameters determining dimensional changes of porous carbons during capacitive charging.* Carbon, 2014. **69**(0): p. 275-286.
20. Shao, L.-H., et al., *Electrocapillary maximum and potential of zero charge of carbon aerogel.* Physical Chemistry Chemical Physics, 2010. **12**(27): p. 7580-7587.
21. Biener, J., et al., *Macroscopic 3D Nanographene with Dynamically Tunable Bulk Properties.* Advanced Materials, 2012. **24**(37): p. 5083-5087.
22. Ruch, P.W., et al., *A dilatometric and small-angle X-ray scattering study of the electrochemical activation of mesophase pitch-derived carbon in non-aqueous electrolyte solution.* Carbon, 2010. **48**(7): p. 1880-1888.
23. Boukhalfa, S., et al., *Small-Angle Neutron Scattering for In Situ Probing of Ion Adsorption Inside Micropores.* Angewandte Chemie International Edition, 2013. **52**(17): p. 4618-4622.
24. Prehal, C., et al., *ELETTRA Experimental Report, Prop. nr. 20125153*. 2013, Synchrotron ELETTRA Trieste, Italy.
25. Schnablegger, H. and Y. Singh, *The SAXS Guide*. 2011, Austria: Anton Paar GmbH.
26. Feigin, L.A. and D.I. Svergun, *Structure Analysis by Small Angle X-ray and Neutron Scattering*, ed. G.W. Taylor. 1987, New York: Plenum Press.
27. Kittel, C., *Einführung in die Festkörperphysik*. 2006, München: Oldenbourg Wissenschaftsverlag GmbH.
28. Paris, O. *IMPRS lecture manuscript, Synchrotron Radiation in materials Science: Small Angle X-ray Scattering*. 2007.
29. Fratzl, P. and O. Paris *IMPRS lecture manuscript, Small-angle scattering*. 2005.
30. Mähler, J. and I. Persson, *A Study of the Hydration of the Alkali Metal Ions in Aqueous Solution.* Inorganic Chemistry, 2011. **51**(1): p. 425-438.
31. Als-Nielesen, J. and D. McMorrow, *Elements of Modern X-ray Physics*. 2011, Chichester, United Kingdom: John Wiley & Sons, Ltd.
32. Schilling, W., *Diffuse Streuung an Kristallen mit Fehlordnung*, in *Streumethoden zur Untersuchung kondensierter Materie - Vorlesungsmanuskript*. 1996: 27. IFF-Ferienkurs im Forschungszentrum Jülich. p. C5.1-C5.12.
33. Hubbell, J.H. and S.M. Seltzer. *Tables of X-Ray Mass Attenuation Coefficients and Mass Energy-Absorption Coefficients from 1 keV to 20 MeV for Elements Z = 1 to 92 and 48 Additional Substances of Dosimetric Interest**. 1996 December 9, 2011 September 17, 2009]; Available from: http://physics.nist.gov/PhysRefData/XrayMassCoef/chap2.html.
34. Béguin, F., E. Raymundo-Piñero, and E. Frackowiak, *Electrical Double-Layer Capacitors and Pseudocapacitors*, in *Carbons for Electrochemical Energy Storage and Conversion Systems*, F. Béguin and E. Frackowiak, Editors. 2010, Taylor and Francis Group: New York.
35. Kurzweil, P., *Electrochemical Double-layer Capacitors*, in *Encyclopedia of Electrochemical power sources*, J. Garche, Editor. 2009, Elsevier: Amsterdam. p. 607-633.
36. Bard, A.J. and L.R. Faulkner, *Electrochemical methods, Fundamentals and Applications*. 2001: John Wiley & Sons.

37. Yu, A., V. Chabot, and J. ZhangYu, *Electrochemical Supercapacitors for energy storage and delivery, Fundamentals and Applications*. 2013: Taylor & Francis Group, LLC.
38. Grahame, D.G., *The electrical double layer and the theory of electrocapillarity.* Chemical Reviews, 1947. **41**(3): p. 441-501.
39. Barbieri, O., et al., *Capacitance limits of high surface area activated carbons for double layer capacitors.* Carbon, 2005. **43**(6): p. 1303-1310.
40. Inagaki, M., H. Konno, and O. Tanaike, *Carbon materials for electrochemical capacitors.* Journal of Power Sources, 2010. **195**(24): p. 7880-7903.
41. Frackowiak, E. and F. Béguin, *Carbon materials for the electrochemical storage of energy in capacitors.* Carbon, 2001. **39**(6): p. 937-950.
42. Chapman, D., *London and Edinburg Phil.* Mag. and J. of Sci, 1913. **25**: p. 475.
43. Gouy, G., J. Phys. Radium, 1910. **9**(9): p. 457.
44. Gouy, G., Compt. Rend., 1910(149): p. 654.
45. Stern, O., *Z Elektrochem.* Angew Phys Chem, 1924. **30**: p. 508-516.
46. Gerischer, H., et al., *Density of the electronic states of graphite: Derivation from differential capacitance measurements.* Journal of Physical Chemistry, 1987. **91**(7): p. 1930-1935.
47. Hahn, M., et al., *Interfacial Capacitance and Electronic Conductance of Activated Carbon Double-Layer Electrodes.* Electrochemical and Solid-State Letters, 2004. **7**(2): p. A33-A36.
48. Meschede, D., *Gerthsen Physik*. Vol. 23. 2005, Berlin, Heidelberg, New York: Springer.
49. Cussler, E.L., *Diffusion: Mass Transfer in Fluid Systems*. 3 ed. 2009, New York: Cambridge Academy Press.
50. Huang, J., B.G. Sumpter, and V. Meunier, *A Universal Model for Nanoporous Carbon Supercapacitors Applicable to Diverse Pore Regimes, Carbon Materials, and Electrolytes.* Chemistry – A European Journal, 2008. **14**(22): p. 6614-6626.
51. Huang, J., B.G. Sumpter, and V. Meunier, *Theoretical Model for Nanoporous Carbon Supercapacitors.* Angewandte Chemie International Edition, 2008. **47**(3): p. 520-524.
52. Viswanath, R.N., D. Kramer, and J. Weissmüller, *Adsorbate effects on the surface stress–charge response of platinum electrodes.* Electrochimica Acta, 2008. **53**(6): p. 2757-2767.
53. Sun, G., et al., *Dimensional change as a function of charge injection in graphite intercalation compounds: A density functional theory study.* Physical Review B, 2003. **68**(12): p. 125411.
54. Sun, G., et al., *Dimensional Changes as a Function of Charge Injection in Single-Walled Carbon Nanotubes.* Journal of the American Chemical Society, 2002. **124**(50): p. 15076-15080.
55. Coussy, O., *Mechanics and Physics of porous solids*. 2011, Chichester, United Kingdom: John Wiley & Sons, Ltd.
56. Wedler, G. and H.-J. Freund, *Lehrbuch der physikalischen Chemie*. 2012, Weinheim: Wiley-VCH Verlag & Co. KGaA.
57. Enoki, T., *Electronic Structures of Graphite and Related Materials*, in *Carbons for Electrochmeical Energy Storage and Conversion Systems*, F. Béguin and E. Frackowiak, Editors. 2010, Taylor and Francis Group, LLC: New York. p. 221-257.
58. Nightingale Jr, E.R., *Phenomenological theory of ion solvation. Effective radii of hydrated ions.* Journal of Physical Chemistry, 1959. **63**(9): p. 1381-1387.

59. Odutola, J.A. and T.R. Dyke, *Partially deuterated water dimers: Microwave spectra and structure.* The Journal of Chemical Physics, 1980. **72**(9): p. 5062-5070.
60. Koneshan, S., et al., *Solvent structure, dynamics, and ion mobility in aqueous solutions at 25 °C.* Journal of Physical Chemistry B, 1998. **102**(21): p. 4193-4204.
61. Paris, O. *IMPRS lecture manuscript, SAS data reduction and analyis*. 2005.
62. de Levie, R., *On porous electrodes in electrolyte solutions: I. Capacitance effects.* Electrochimica Acta, 1963. **8**(10): p. 751-780.
63. Fauvarque, J.F. and P. Simon, *Principles of Electrochemistry and Electrochemical Methods*, in *Carbons for Electrochemical Energy Storage and Energy Conversion Systems*, F. Béguin and E. Frackowiak, Editors. 2010, Taylor and Francis Group, LLC: New York. p. 1-39.
64. Stoller, M.D. and R.S. Ruoff, *Best practice methods for determining an electrode material's performance for ultracapacitors.* Energy & Environmental Science, 2010. **3**(9): p. 1294-1301.
65. Lindner, P., *Neutrons, X-rays and Light, Scattering Methods Applied to Soft Condensed Matter*. 2002, Amsterdam: Elsevier Science B.V.
66. Glatter, O. and O. Kratky, *Small Angle X-ray Scattering*. 1982, London: Academic Press Inc.
67. Gibaud, A., J.S. Xue, and J.R. Dahn, *A small angle X-ray scattering study of carbons made from pyrolyzed sugar.* Carbon, 1996. **34**(4): p. 499-503.
68. Debye, P., H.R. Anderson, and H. Brumberger, *Scattering by an Inhomogeneous Solid. II. The Correlation Function and Its Application.* Journal of Applied Physics, 1957. **28**(6): p. 679-683.
69. He, L., et al., *Small-angle neutron scattering characterization of the structure of nanoporous carbons for energy-related applications.* Microporous and Mesoporous Materials, 2012. **149**(1): p. 46-54.
70. Perret, R. and W. Ruland, *X-ray small-angle scattering of non-graphitizable carbons.* Journal of Applied Crystallography, 1968. **1**(5): p. 308-313.
71. Ruland, W., *Small-angle scattering of two-phase systems: determination and significance of systematic deviations from Porod's law.* Journal of Applied Crystallography, 1971. **4**(1): p. 70-73.
72. Paris, O., C. Zollfrank, and G.A. Zickler, *Decomposition and carbonisation of wood biopolymers - A microstructural study of softwood pyrolysis.* Carbon, 2005. **43**(1): p. 53-66.
73. Paris, O., et al., *Cross-sectional texture of carbon fibres analysed by scanning microbeam X-ray diffraction.* Journal of Applied Crystallography, 2001. **34**(4): p. 473-479.
74. Ruland, W., *Carbon Fibers.* Advanced Materials, 1990. **2**(11): p. 528-536.
75. Deschamps, M., et al., *Exploring electrolyte organization in supercapacitor electrodes with solid-state NMR.* Nature Materials, 2013. **12**(4): p. 351-358.
76. Prass, J., et al., *Capillarity-driven deformation of ordered nanoporous silica.* Applied Physics Letters, 2009. **95**(8): p. -.
77. Erko, M., et al., *Density minimum of confined water at low temperatures: A combined study by small-angle scattering of X-rays and neutrons.* Physical Chemistry Chemical Physics, 2012. **14**(11): p. 3852-3858.

Appendix A

Igor Pro code: electrolyte structure factor amplitude evaluation

```
#pragma rtGlobals=1                    // Use modern global access method and strict wave access.
#include <KBColorizeTraces>

//******************************************************************************************
//fit_structurfactor()
//
//**DESCRIPTION
// The function fit_structurefactor_2 fits the scattering curve of an electrolyte bulk measurement to the WAXS scattering intensity of a working EDLC at a defined Q-region.
The scattering curves of an entire in-situ measurement series and the bulk electrolyte measurement represent the input files.
The only fit parameter is a prefactor to the bulk electrolye scattering intensity.
The result is a series of prefactors which is proportional to the integrated intensity signal of teh defined Q-region.

#include "select_interactively"

static strconstant PROCNAME = "fit_structurfactor"
static strconstant gErrExt = "_fit"

MENU "own procedures"
        "fit structurfactor 2", fit_structurefactor_2()
END

function fit_structurefactor_2()

        string theWaveList

        // Generate input waves:
        theWaveList = select_interactively("Select waves to be fitted", showWaves=1, showVars=0, showStrs=0, verbose=1)
        variable n = itemsInList(theWaveList)

        if (n == 0) // no waves selected!
                printf "### ERROR: %s: No waves selected, cannot continue\r", PROCNAME
                return -1
        endif

        //Generate fitparameter wave:
        make /N=(n)/D/O fitpar

        string theItem, theName, thePath
        variable nErr = 0
        variable i, len

        for(i=0; i<n; i+=1)

                theItem = stringFromList(i, theWaveList)
                thePath = parseFilePath(1, theItem, ":", 1, 0)
                theItem = parseFilePath(0, theItem, ":", 1, 0)
                setDataFolder thePath
                wave /Z theWave = $theItem
                if (!waveExists(theWave))
                        nErr += 1
```

```
                printf "### WARNING: %s: Unable to find wave %s, skipping\r", PROCNAME, theItem
                continue
        endif

        //Least Square Fit:
        Optimize/L=3000/H=9000 LeastSquaresEl_2, theWave
        fitpar[i]=V_minloc

endfor

// After the Fitparameter wave has been filled up, the integrated intensity for all Q < 9nm^-1 is calculated and used as output :
wave /Z qa_waxs = root:CsCl_electrolyte:qa_waxs1

String extension=gErrExt
variable j
wave /Z el_1M = root:CsCl_electrolyte:el_6cm_00_002_nob_ip
wave /Z qa_waxs = root:CsCl_electrolyte:qa_waxs1
make /N=(n)/D/O CsBack

for(j=0; j<n; j+=1)

        theItem = stringFromList(j, theWaveList)
        thePath = parseFilePath(1, theItem, ":", 1, 0)
        theItem = parseFilePath(0, theItem, ":", 1, 0)
        setDataFolder thePath
        wave /Z theWave = $theItem
        if (!waveExists(theWave))
                nErr += 1
                printf "### WARNING: %s: Unable to find wave %s, skipping\r", PROCNAME, theItem
                continue
        endif
        theName = theItem+extension
        duplicate /O theWave $theName
        wave theFitWave = $theName
        theFitWave=fitpar[j]*el_1M
        Csback[j]=(sum(theFitWave, 0, 80))/61

endfor

END

// Least Square Fit:
function LeastSquaresEl_2(theWave, a)

        wave theWave
        variable a

        variable Qmin, Qmax

        Qmin=100
        Qmax=300

        wave /Z qa_waxs = root:CsCl_electrolyte:qa_waxs1
        wave /Z el_1M = root:CsCl_electrolyte:el_6cm_00_002_nob_ip
        make /N=(numpnts(el_1M))/D/O error
        variable errorsum
```

```
        error=abs(theWave-(a*el_1M))
        errorsum=sum(error, Qmin, Qmax)

        print errorsum

        return errorsum

END
//*****************************************************************************************
```

Igor Pro code: electrolyte structure factor evaluation

```
#pragma rtGlobals=1                    // Use modern global access method and strict wave access.
#include <KBColorizeTraces>

//*****************************************************************************************
//fit_structurfactor()
//
//**DESCRIPTION
//** Function which estimates the electrolyte structure factor background intensity of an entire in-situ experiment
// (which means that we have a set of background intensity values as a result)

#include "select_interactively"

static strconstant PROCNAME = "fit_corrlength_2"
static strconstant gErrExt = "_subCs"

MENU "own procedures"
        "fit correlation length 2", fit_corr_length_2()
END

ragma rtGlobals=1              // Use modern global access method and strict wave access.
#include <KBColorizeTraces>

function fit_corr_length_2()

string theWaveList

        // Generate input waves (select all SAXS scattering intensity curves of interest)
        theWaveList = select_interactively("Select waves to be fitted", showWaves=1, showVars=0, showStrs=0,
        verbose=1)
        variable n = itemsInList(theWaveList)

        if (n == 0) // no waves selected!
                printf "### ERROR: %s: No waves selected, cannot continue\r", PROCNAME
                return -1
        endif

        // Input of the normalized CsBackgroundWave, gained from the integrated intensity calculation in the WAXS
        Q-region: 6 - 9nm^-1
        wave /Z CsBackground = root:D9_CVCAL3_WAXS:CsBack_1M_100_300_no

        variable Qmin, Qmax

        // Define SAXS Q-region in which the model fit should be performed.
        // This should be a Q-region where only the background intensity change causes a correlation length change
        Qmin=370                       // corresponds to 3.5nm^-1
        Qmax=510                       // corresponds to 5nm^-1
```

```
// Define variables and waves:
String extension=gErrExt
string theItem, theName, thePath
string theZeroItem, theZeroName, theZeroPath
variable nErr = 0
variable i, len

wave /Z qa_saxs = root:qa_SAXS
make /N=(numpnts(CsBackground))/D/O error
make /N=16/D/O errorsum
make /N=40/D/O finalerrorsum
make /N=40/D/O fitpar2
make /N=(numpnts(qa_saxs))/D/O modelWave
make /N=(n)/D/O corr_length_calc
make /N=40/D/O fitparameter
make /N=16/D/O fitparameter2

// Define fitparameter waves:
// The first fitparameterwave correponds to a scaling factor for the relative background changes that have been estimated from the WAXS region
variable u=0
for(u=0; u<40; u+=1)
        fitparameter[u]=3+(5/40)*u
endfor

// The second fitparameterwave correponds to a constant that is added to the relative background changes.
for(u=0; u<16; u+=1)
        fitparameter2[u]=-0.5+(1/16)*u
endfor

string name

// Define waves for the modeled correlation length signals
variable w
for(w=0; w<40; w+=1)

        name = "model_corr_"+num2str(w)
        make /N=(n)/D/O $name
        wave /Z model_corr_length = $name

// Here the procedure begins
variable v
for(v=0; v<16;v+=1)

        for(i=0; i<n; i+=1)

                theZeroItem = stringFromList(0, theWaveList)
                thePath = parseFilePath(1, theZeroItem, ":", 1, 0)
                theZeroItem = parseFilePath(0, theZeroItem, ":", 1, 0)
                setDataFolder thePath
                wave /Z theZeroWave = $theZeroItem

                theItem = stringFromList(i, theWaveList)
                theItem = parseFilePath(0, theItem, ":", 1, 0)

                wave /Z theWave = $theItem
                if (!waveExists(theWave))
```

```
		nErr += 1
		printf "### WARNING: %s: Unable to find wave %s, skipping\r", PROCNAME, theItem
		continue
endif

variable integ_int_dum=0
variable j

for(j=Qmin; j<Qmax; j+=1)
		integ_int_dum+=(theWave[j]-((fitparameter[w]*CsBackground[i])+fitparameter2[v]))*((qa_saxs[Qmax]-qa_saxs[Qmin])/(Qmax-Qmin))*qa_saxs[j]
endfor

variable integ_int_zero=0

for(j=Qmin; j<Qmax; j+=1)
		integ_int_zero+=(theZeroWave[j]-((fitparameter[w]*CsBackground[i])+fitparameter2[v]))*((qa_saxs[Qmax]-qa_saxs[Qmin])/(Qmax-Qmin))*qa_saxs[j]
endfor

variable ZeroWaveFactor
ZeroWaveFactor=integ_int_dum/integ_int_zero

// Subtract: (theWave-fittingparameter[w]*CsBackground[i])
// calculate integrated intensity of the subtraction result
// normalize this value with integrated intensity value of the ZeroWave
// use this value as a factor for the following "ZeroWaveSubtraction"!

modelWave=(theZeroWave-((CsBackground[0]*fitparameter[w])))*ZeroWaveFactor+((CsBackground[i]*fitparameter[w])+fitparameter2[v])		// ->change depending on the First reference corr.length value you pick

variable integ_int=0
variable invariant=0

for(j=Qmin; j<Qmax; j+=1)
		integ_int+=modelWave[j]*((qa_saxs[Qmax]-qa_saxs[Qmin])/(Qmax-Qmin))*qa_saxs[j]
		invariant+=modelWave[j]*((qa_saxs[Qmax]-qa_saxs[Qmin])/(Qmax-Qmin))*((qa_saxs[j])*qa_saxs[j])
endfor

model_corr_length[i]=integ_int/invariant

integ_int=0
invariant=0
for(j=Qmin; j<Qmax; j+=1)
		integ_int+=theWave[j]*((qa_saxs[Qmax]-qa_saxs[Qmin])/(Qmax-Qmin))*qa_saxs[j]
		invariant+=theWave[j]*((qa_saxs[Qmax]-qa_saxs[Qmin])/(Qmax-Qmin))*((qa_saxs[j])*qa_saxs[j])
endfor

corr_length_calc[i]=integ_int/invariant
```

```
		endfor


		error=abs(corr_length_calc-model_corr_length)
		//errorsum[w]=sum(error, 728, 1285)  //use for d7_ca1
		errorsum[v]=sum(error)

endfor                                          // end of v-loop

SetScale/I x -0.5,0.5,errorsum                  // give it an X range of [-0.5, 0.5]
//Display errorsum

WaveStats errorsum

finalerrorsum[w]=errorsum[V_minRowLoc]
fitpar2[w]=V_minloc

endfor                                          // end of w-loop


SetScale/I x 3,8,finalerrorsum                  // give it an X range of [3, 8]
Display finalerrorsum

variable fitpar, fitpar_2
WaveStats finalerrorsum
fitpar = V_minloc
fitpar_2 = fitpar2[V_minRowLoc]
print fitpar
print fitpar_2

//after that write function to output the data together with the fits:

variable g

for(g=0; g<n; g+=1)

		theItem = stringFromList(g, theWaveList)
		thePath = parseFilePath(1, theItem, ":", 1, 0)
		theItem = parseFilePath(0, theItem, ":", 1, 0)
		setDataFolder thePath
		wave /Z theWave = $theItem
		if (!waveExists(theWave))
			nErr += 1
			printf "### WARNING: %s: Unable to find wave %s, skipping\r", PROCNAME, theItem
			continue
		endif
		theName = theItem+extension
		duplicate /O theWave $theName
		wave theSubWave = $theName
		theSubWave=theSubWave-((fitpar*CsBackground[g])+fitpar_2)   //CHECK!

endfor

for(w=0; w<40; w+=1)

		name = "model_corr_"+num2str(w)
		make /N=(n)/D/O $name
```

```
        wave /Z model_corr_length = $name

for(i=0; i<n; i+=1)                    //-> change in the case of using a special fitting region (eg. 728 until 1285 for d7_ca1)

        theZeroItem = stringFromList(0, theWaveList)        //-> always use the most representative corr. length point of the beginning

        thePath = parseFilePath(1, theZeroItem, ":", 1, 0)
        theZeroItem = parseFilePath(0, theZeroItem, ":", 1, 0)
        setDataFolder thePath
        wave /Z theZeroWave = $theZeroItem

        theItem = stringFromList(i, theWaveList)
        theItem = parseFilePath(0, theItem, ":", 1, 0)

        wave /Z theWave = $theItem
        if (!waveExists(theWave))
                nErr += 1
                printf "### WARNING: %s: Unable to find wave %s, skipping\r", PROCNAME, theItem
                continue
        endif

        integ_int_dum=0

        for(j=Qmin; j<Qmax; j+=1)
                integ_int_dum+=(theWave[j]-
                ((fitparameter[w]*CsBackground[i])+fitparameter2[v]))*((qa_saxs[Qmax]-
                qa_saxs[Qmin])/(Qmax-Qmin))*qa_saxs[j]
        endfor

        integ_int_zero=0

        for(j=Qmin; j<Qmax; j+=1)
                integ_int_zero+=(theZeroWave[j]-
                ((fitparameter[w]*CsBackground[i])+fitparameter2[v]))*((qa_saxs[Qmax]-
                qa_saxs[Qmin])/(Qmax-Qmin))*qa_saxs[j]
        endfor

        ZeroWaveFactor=integ_int_dum/integ_int_zero

        modelWave=(theZeroWave-
        ((CsBackground[0]*fitparameter[w])))*ZeroWaveFactor+((CsBackground[i]*fitparameter[w])+fitpar_
        2)
        // ->change depending on the First reference corr.length value you pick

        integ_int=0
        invariant=0

        for(j=Qmin; j<Qmax; j+=1)
                integ_int+=modelWave[j]*((qa_saxs[Qmax]-qa_saxs[Qmin])/(Qmax-Qmin))*qa_saxs[j]
                invariant+=modelWave[j]*((qa_saxs[Qmax]-qa_saxs[Qmin])/(Qmax-
                Qmin))*((qa_saxs[j])*qa_saxs[j])
        endfor

        model_corr_length[i]=integ_int/invariant

endfor
```

```
        endfor


END
//*****************************************************************************************
```

Igor Pro code: fit-stability test of the electrolyte structure factor evaluation

```
#pragma rtGlobals=1                    // Use modern global access method and strict wave access.
#include <KBColorizeTraces>

//*****************************************************************************************
// test fitstability
//
//**DESCRIPTION
// Procedure to calculate directly the integral paramters of the subtracted electrolyte structure factor background
// The input of the fit paramters calulated from the procedure "fit_corr_length" takes place manually.
// Thus the validity of the fitparameters can be testet by looking at the final integral parameter signals.

#include "select_interactively"

static strconstant PROCNAME = "test_fitstab"
static strconstant gErrExt = "_sub25"

MENU "own procedures"
        "test fitstability",test_fitstab()
END

ragma rtGlobals=1            // Use modern global access method and strict wave access.
#include <KBColorizeTraces>

function test_fitstab()

        string theWaveList

        // Generate waves:
        theWaveList = select_interactively("Select waves to be subtracted", showWaves=1, showVars=0, showStrs=0,
        verbose=1)
        variable n = itemsInList(theWaveList)

        if (n == 0) // no waves selected!
                printf "### ERROR: %s: No waves selected, cannot continue\r", PROCNAME
                return -1
        endif

        wave /Z CsBackground = root:D8_CVCAL1_WAXS:CsBack_1M_100_300_no    //->change!

        //Define the Q-regime:
        variable Qmin, Qmax
        Qmin=90
        Qmax=210

        String extension=gErrExt
        string theItem, theName, thePath
        variable nErr = 0
        variable i, len

        wave /Z qa_saxs = root:qa_SAXS
```

```
	//make /N=(numpnts(CsBackground))/D/O error
	String theName1 = "d8_cvcaL1_a5.05_"+num2str(Qmin)+"_"+num2str(Qmax)+"_integ"
	String theName2 = "d8_cvcaL1_a5.05_"+num2str(Qmin)+"_"+num2str(Qmax)+"_invar"
	String theName3 = "d8_cvcaL1_a5.05_"+num2str(Qmin)+"_"+num2str(Qmax)+"_corr"

	make /N=(n)/D/O $theName1
	make /N=(n)/D/O $theName2
	make /N=(n)/D/O $theName3

	wave integ_int_fitstab = $theName1
	wave invariant_fitstab = $theName2
	wave cor_len_fitstab = $theName3

	variable g

	for(g=0; g<n; g+=1)

		theItem = stringFromList(g, theWaveList)
		thePath = parseFilePath(1, theItem, ":", 1, 0)
		theItem = parseFilePath(0, theItem, ":", 1, 0)
		setDataFolder thePath
		wave /Z theWave = $theItem
		if (!waveExists(theWave))
			nErr += 1
			printf "### WARNING: %s: Unable to find wave %s, skipping\r", PROCNAME, theItem
			continue
		endif

		variable integr=0
		variable invari=0
		variable j

		// Define input fitparamters in the following for-loop:
		for(j=Qmin; j<Qmax; j+=1)
			integr+=(theWave[j]-((5.05*CsBackground[g])-0.15))*((qa_saxs[Qmax]-
			qa_saxs[Qmin])/(Qmax-Qmin))*qa_saxs[j]
			invari+=(theWave[j]-((5.05*CsBackground[g])-0.15))*((qa_saxs[Qmax]-
			qa_saxs[Qmin])/(Qmax-Qmin))*((qa_saxs[j])*qa_saxs[j])
		endfor

		integ_int_fitstab[g]=integr
		invariant_fitstab[g]=invari
		cor_len_fitstab[g]=integr/invari

	endfor

	variable integi, invarii, corri
	integi=integ_int_fitstab[0]
	invarii=invariant_fitstab[0]
	corri=cor_len_fitstab[0]

	integ_int_fitstab/=integi
	invariant_fitstab/=invarii
	cor_len_fitstab/=corri

END
//*************************************************************************************
```

Appendix B

Igor Pro code: ion concentration calculation

```
//*****************************************************************************************
// Function to perform the Cs/Cl concentration fit
// Furthermore the error of the Cs/Cl concentration estimation procedure is calculated
// by varying the input paramters with a gaussian distribution. The spread of the final result
// corresponds to the error.

function error_ionconc2()

wave trans=root:in_situ_trans7:C11_CA05_L4_trans
Duplicate/O trans transmission
transmission*=0.985
wave charge=root:in_situ_trans7:C11_CA05_L4_Q_realval

//wave myd=root:in_situ_trans6:C10_CA05_L5_myd8

make /N=7/D/O C11_CA05_L4_param

make /N=100/D/O Cs
make /N=100/D/O Cl
make /N=100/D/O startconcentration
make /N=100/D/O porevolume


variable i
for(i=0; i<100; i+=1)
        //Define parameters, spread them with gaussian distribution, in order to calculate the error of the final result
        variable Trans_yp80_sco=(0.913*0.985)+gnoise(0.017)
        variable Trans_yp80_sco_h2o=(0.6374*0.985)+gnoise(0.03)
        variable
        Trans_yp80_sco_1Mel=((transmission[0]+transmission[2]+transmission[4]+transmission[6])/4)+gnoise(0.012)
        variable absorb_Cs=2178.10+gnoise(60)
        variable absorb_Cl=189.9+gnoise(10)
        variable dens_Cs=6.60311+gnoise(0.30)
        variable dens_Cl=1.71414+gnoise(0.20)
        variable d=0.034+gnoise(0.0015)
        variable A=2.835+gnoise(0.12)

        variable d_h2o=(-ln(Trans_yp80_sco_h2o)+ln(Trans_yp80_sco))/10.35
        variable porosity=d_h2o/d
        variable        X_Cs=(ln(Trans_yp80_sco_1Mel)-ln(Trans_yp80_sco_h2o))/(-(absorb_Cs*        d_h2o)-
        (absorb_Cl*d_h2o)+(2*(-ln(Trans_yp80_sco_h2o)+ln(Trans_yp80_sco))))
        variable V_Cs=X_Cs*(1000/((1-2*X_Cs)))
        variable X_h2o=1-(2*X_Cs)
        variable mass_Cs=V_Cs*dens_Cs
        variable startconc_Cs=(mass_Cs/132)*6.022e+20
        startconcentration[i]=startconc_Cs
        variable d_el=d_h2o
        variable V_pores=d*A*porosity
        porevolume[i]=V_pores

        //variable factor=gnoise(0.03)
```

```
        //myd=(-ln(transmission)+ln(Trans_yp80_sco))*(1+factor)

        C11_CA05_L4_param[0]=absorb_Cs
        C11_CA05_L4_param[1]=absorb_Cl
        C11_CA05_L4_param[2]=startconc_Cs
        C11_CA05_L4_param[3]=X_Cs
        C11_CA05_L4_param[4]=d_el
        C11_CA05_L4_param[5]=V_pores
        C11_CA05_L4_param[6]=(-9.735100E+18)+gnoise(0.6E+18)

        //Perform the fit 4 times
        fitTraces("ion_conc2", include="*", exclude="fit*", paramWave="root:W_coef", resName="Graph17",
        resFolder="root:in_situ_trans_7:", hold="00", constrain="", paramNames="A;B;", weightExt="_none_",
        extractRes="00", extractSD=0, plot=0, reverseFit=0, useCursors=1, resetGuess=0, verbose=1)
        fitTraces("ion_conc2", include="*", exclude="fit*", paramWave="root:W_coef", resName="Graph17",
        resFolder="root:in_situ_trans_7:", hold="00", constrain="", paramNames="A;B;", weightExt="_none_",
        extractRes="00", extractSD=0, plot=0, reverseFit=0, useCursors=1, resetGuess=0, verbose=1)
        fitTraces("ion_conc2", include="*", exclude="fit*", paramWave="root:W_coef", resName="Graph17",
        resFolder="root:in_situ_trans_7:", hold="00", constrain="", paramNames="A;B;", weightExt="_none_",
        extractRes="00", extractSD=0, plot=0, reverseFit=0, useCursors=1, resetGuess=0, verbose=1)
        fitTraces("ion_conc2", include="*", exclude="fit*", paramWave="root:W_coef", resName="Graph17",
        resFolder="root:in_situ_trans_7:", hold="00", constrain="", paramNames="A;B;", weightExt="_none_",
        extractRes="00", extractSD=0, plot=0, reverseFit=0, useCursors=1, resetGuess=0, verbose=1)


        wave parameterwave=root:W_coef

        Cs[i]=parameterwave[0]
        Cl[i]=((C11_CA05_L4_param[6])/V_pores)+Cs[i]
        //Cl[i]=Cs[i]-((C11_CA05_L4_param[6])/V_pores)

endfor

Wavestats Cs
Wavestats Cl

END


Function ion_conc2(w,x)
        Wave w; Variable x

        wave parameter=root:in_situ_trans7:C11_CA05_L4_param

        //return 1.90344+(w[0]*(1-exp(-x/w[1]))*(absorb_Cs*X_Cs*d_el)/(startconc_Cs))+((w[0]+((-
        9.735E+18)/V_pores))*(1-exp(-x/w[1]))*(absorb_Cl*X_Cs*d_el)/(startconc_Cs))
        Return 1.6314+(w[0]*(1-exp(-
        x/w[1]))*(parameter[0]*parameter[3]*parameter[4])/(parameter[2]))+((w[0]+((parameter[6])/parameter[5]))
        *(1-exp(-x/w[1]))*(parameter[1]*parameter[3]*parameter[4])/(parameter[2]))
        //return 1.87344+((w[0]-(parameter[6]/parameter[5]))*(1-exp(-
        x/w[1]))*(parameter[0]*parameter[3]*parameter[4])/(parameter[2]))+(w[0]*(1-exp(-
        x/w[1]))*(parameter[1]*parameter[3]*parameter[4])/(parameter[2]))

End

//*****************************************************************************************
```